Advances in Meteorology

Aviation Meteorology

Lead Guest Editor: Pak Wai Chan
Guest Editors: Feng Chen and Thomas Hauf

Aviation Meteorology

Advances in Meteorology

Aviation Meteorology

Lead Guest Editor: Pak Wai Chan
Guest Editors: Feng Chen and Thomas Hauf

Contents

Hindawi
Advances in Meteorology
Volume 2022, Article ID 3128657, 14 pages
https://doi.org/10.1155/2022/3128657

Research Article

Progressive and Prospective Technology for Cloud Seeding Experiment by Unmanned Aerial Vehicle and Atmospheric Research Aircraft in Korea

Woonseon Jung,[1] **Joo Wan Cha**,[1] **A.-Reum Ko**,[1] **Sanghee Chae**,[1] **Yonghun Ro**,[1] **Hyun Jun Hwang**,[1] **Bu-Yo Kim**,[1] **Jung Mo Ku**,[1] **Ki-Ho Chang**,[1] **and Chulkyu Lee**[2]

[1]*Research Applications Department, National Institute of Meteorological Sciences, Korea Meteorological Administration, 33, Seohobuk-ro, Seogwipo-si, Jeju-do 63568, Republic of Korea*
[2]*Observation Research Department, National Institute of Meteorological Sciences, Korea Meteorological Administration, 33, Seohobuk-ro, Seogwipo-si, Jeju-do 63568, Republic of Korea*

Correspondence should be addressed to Woonseon Jung; wsjung01@korea.kr

Received 6 January 2022; Revised 23 May 2022; Accepted 30 May 2022; Published 22 June 2022

Academic Editor: Feng Chen

This study applies a novel cloud seeding method using an unmanned aerial vehicle (UAV) and a research aircraft in Korea. For this experiment, the UAV sprayed a cloud seeding material (calcium chloride), and the aircraft monitored the clouds in the southern part of the Korean Peninsula on April 25, 2019. Cloud observation equipment in the aircraft indicated an increase in the number concentration and average particle size of large cloud particles after the seeding. Weather radar reflectivity increased by approximately 10 dBZ above the experimental area due to the development of clouds and precipitation systems. Rain was observed after seeding, and 0.5 mm was recorded, including natural and mixed precipitation from the cloud seeding. In addition, it showed that the rapid increase in the number of raindrops and vertical reflectivity was approximately 10 dBZ. Therefore, these results showed the possibility of cloud seeding using UAVs and atmospheric research aircraft. The effects of cloud seeding are indicated through the increased number concentration and size of cloud particles, radar reflectivity, and ground-based precipitation detection.

1. Introduction

Aerosols can act as cloud condensation nuclei or ice nuclei and affect cloud formation and lifetime. Understanding the microphysical effects of aerosols on clouds and precipitation is critical in understanding and predicting climate change [1]. In weather modification technology, cloud seeding materials corresponding to these aerosols act as cloud condensation or ice nuclei, thus affecting cloud and precipitation formation. Weather modification is an advanced scientific technique that is used in the meteorological field to enhance precipitation, suppress hail, and dissipate fog. It is an important method that can be used to alleviate water resource scarcity, drought relief, and forest-fire prevention. For the future of atmospheric sciences, weather modification techniques are critical. Cloud seeding experiments have been performed using seeding materials that have been used since 1946 [2–5]. Weather modification is a technology in which cloud seeding materials artificially cause cloud condensation and precipitation development in areas of the atmosphere with insufficient cloud condensation or ice nuclei.

Weather modification techniques originated from the discovery that spraying artificial ice nuclei into supercooled clouds can increase the number concentration of ice crystals [2, 3]. The cloud seeding method depends on precipitation formation processes, which vary with cloud temperature. In cold clouds (below 0°C), precipitation is induced by spraying ice nuclei materials, such as silver iodide or dry ice, to

produce or strengthen ice. In warm clouds (above 0°C), precipitation is induced by spraying hygroscopic substances, such as sodium chloride or calcium chloride, which act as cloud condensation nuclei and promote the collision-coalescence process in the cloud. The seeding particles serve to increase the drop-size distribution, which accelerates the rain process [6, 7].

The World Meteorological Association (WMO) noted that the development of meteorological projects, such as weather modification activities, has grown significantly due to an increase in social-economic demand for drought relief, water resources, and fire forest prevention [8]. Weather modification has been proposed as a means to minimize environmental problems and secure water resources at a relatively low cost [9, 10]. Thus, cloud seeding experiments and analysis technologies are needed. Currently, weather modification projects are underway worldwide, including in the United States, China, Japan, the United Arab Emirates, and Russia [8]. Cloud seeding experiments using aircraft have been performed to gain meaningful results [6, 9, 11–26]. Furthermore, the method shows high success for rain enhancement [5, 6, 27–29]. The United States and Thailand are conducting cloud seeding experiments with aircraft to increase long-term precipitation; they suggested an increase in annual precipitation through cloud seeding [30–32]. Various other cloud seeding studies have been conducted using aircraft. An overview of these studies/experiments is provided in the following.

The Wyoming Weather Modification Pilot Project (WWMPP) was performed to statistically evaluate the effectiveness of cloud seeding with silver iodide in the Medicine Bow and Sierra Madre Ranges of south-central Wyoming [30]. The cloud seeding program over the Sierra Nevada mountains region resulted in six successful and five unsuccessful cases [33]. The Seeded and Natural Orographic Wintertime Cloud: the Idaho Experiment (SNOWIE) project was performed to verify the cloud seeding effect using meteorological radar and cloud droplet instrument [34]. The Queensland Cloud Seeding Research Program (QCSRP) was carried out in Australia to investigate the cloud seeding effect on cloud and precipitation in a clean aerosol environment [35]. In South Africa, seeding with hygroscopic seeding flares from the wings of an aircraft resulted in an increase in radar-measured rain mass [20]. The cloud seeding experiments in Israel showed the precipitation enhancement over the target area with strong low pressure, precipitation, and wind of synoptic condition [36]. In India, cloud seeding from aircraft-based hygroscopic flares attributed an approximate 17% of the total rainfall. The growth rate was shown to be sensitively affected by aerosol size distribution, vertical velocity, pressure, temperature, and relative humidity [37]. These cloud seeding experiments have been attempted using various types of aircraft, such as helicopters, drones, rockets, and airplanes [8, 38].

In Korea, cloud seeding experiments using aircraft were first conducted in 1963 [39] and are still being used [40–47]. Since 2018, cloud seeding experiments and observations have been executed using atmospheric research aircraft [45, 46]. The available days for a cloud seeding experiment in Korea are estimated to be between 40 and 91 per annum to cover all the focus areas, namely, water resources, drought relief, forest-fire prevention, and air quality improvement [47]. However, these experiments entail considerable costs associated with building and maintaining infrastructure (e.g., aircraft and equipment).

Recently, an unmanned aerial vehicle (UAV) has been proposed as an alternative, more cost-effective solution to expand weather modification technology. Thus, more recently, UAV systems have been tested for their use in various fields, including meteorology, environment, and its applications [48–52]. The UAV system is a useful tool for cloud seeding operations and efficiency analysis. In the United States, an unmanned aerial system platform was established to investigate the potential of UAVs in conducting cloud observation experiments [48, 50]. They tried to develop a framework to use autonomous unmanned aircraft systems for the operation and evaluation of cloud seeding activities. They found major advantages in using the UAV system for cloud seeding operations that enable the identification of the atmospheric environmental conditions for more effective implementation of cloud seeding. They further provided a context and guidance on using unmanned aircraft systems for the operation and implementation of cloud seeding. For the operation of cloud seeding, a large UAV system, including sensors and seeding material, is needed [48, 50]. The Lower Atmospheric Process Studies at Elevation-a Remotely Piloted Aircraft Team Experiment (LAPSE-RATE) campaign was conducted using an unmanned aerial system to observe the vertical profile of aerosol, carbon dioxide, water vapor, and other meteorological parameters [53]. Compared to manned aircraft, UAVs require less workforce and lower budgets and can fly during severe weather conditions.

This study introduces and analyzes the first cloud seeding experiment using both UAVs and atmospheric research aircraft in Korea. It further presents research direction for future cloud seeding experiments utilizing UAVs. Moreover, the experiment and observations considered the differences between the windward and leeward sides of the flight area and utilized diverse verification methods, such as satellites, radar, aircraft observation equipment, ground-based observation equipment, and numerical models.

2. Materials and Methods

In this study, cloud seeding experiments were conducted using a UAV and an atmospheric research aircraft. Figure 1 shows the aircraft and instruments in the (a) UAV and (b) Korea Meteorological Administration (KMA)/National Institute of Meteorological Sciences (NIMS) Atmospheric Research Aircraft (NARA). Table 1 provides the respective specifications. The UAV used in this study is a TR-60 practical tiltrotor UAV developed by the Korea Aerospace Research Institute, which can take off and land vertically and fly at high speeds. This is a next-generation UAV system that can perform reconnaissance and surveillance missions through a fast approach towards the target point [54–56]. It has a wing length of 3 m, maximum takeoff payload of 200 kg, maximum flight time of 5 h, and maximum ceiling altitude of 3 km. This

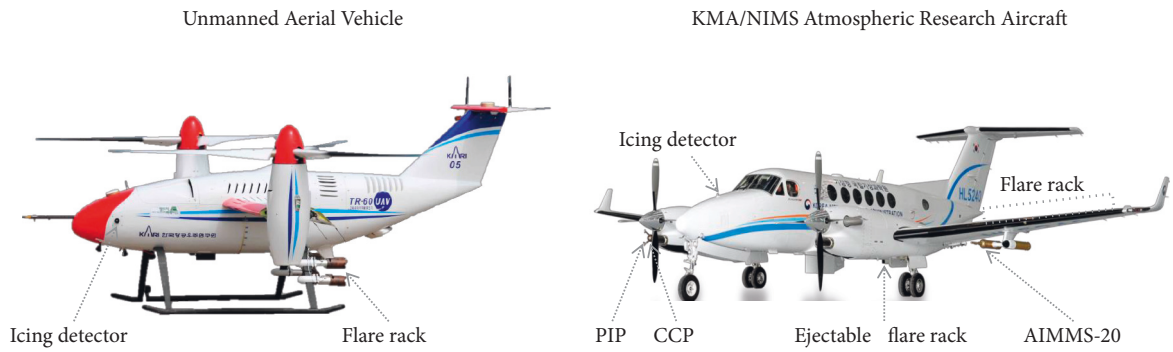

Figure 1: Aircraft and its instruments in (a) UAV and (b) NARA.

Table 1: Specification of UAV and NARA.

	Unmanned aerial vehicle (UAV)	KMA/NIMS Atmospheric Research Aircraft (NARA)
Type	TR60	King Air 350 HW
Manufacturer	Korea Aerospace Research Institute (Korea)	Beechcraft (USA)
Size (m)	Wing: 3	L/W/H: 14.22/17.65/4.37
Maximum ceiling (km)	3	10
Maximum speed (km/h)	240	578
Maximum takeoff payload (kg)	200	7,425
Maximum flight time (hour)	5	5.5
Maximum range (km)	240	2,871
Scientific instruments	Flare rack	Flare rack, CCNC, CIP, CDP, PIP, and WCM-2000

enables vertical takeoff and landing operations in narrow areas, high-speed flight, and high-efficiency reconnaissance and monitoring. To expand the utility of the UAV, it was developed to control a flare rack installed underneath it to conduct cloud seeding experiments. The flare rack is designed to be equipped with four to six flares.

The NARA used in this study was a King Air 350 HW model manufactured by Beechcraft in the United States in November 2017. The engine is a turbo-prop model in which two propellers operate, with a maximum ceiling of 10 km and a maximum flight time of 5.5 h. The NARA was equipped with a total of 25 types of meteorological observation instruments to conduct severe weather monitoring, environmental monitoring, greenhouse gas monitoring, cloud physics observations, and cloud seeding [57]. To conduct cloud seeding experiments, the NARA was equipped with a flare rack, cloud condensation nuclei counter (CCNC) for 0.75–10 μm cloud condensation nuclei observation, cloud imaging probe (CIP) for 7.5–930 μm cloud particle observation, cloud droplet probe (CDP) for 2–50 μm cloud particle observation, precipitation imaging probe for 100–6,200 μm precipitation particle observations, and multielement water content measurement (WCM-2000) for liquid water content. Cloud physics observations and cloud seeding experiments using NARAs have been actively conducted since 2018 and showed increases in cloud particle size and ground precipitation [45].

To conduct the cloud seeding experiment, the first in Korea to use both the UAV and NARA, an experimental design suitable for the purpose of each aircraft was prepared. The experiment sprayed cloud seeding material using the UAV and observed the atmospheric conditions and cloud particles using NARA. To apply cloud seeding to warm clouds, the UAV was equipped with calcium chloride flares from the Ice Crystal Engineering company. To verify the experiment results, data from the CIP, CDP, weather radar, automatic weather system (AWS), micro rain radar, disdrometer, and a numerical model were analyzed.

Variations in the cloud particle microphysics were analyzed using cloud physics observation equipment mounted on the NARA. The C-band weather radar at the Korea Aerospace Research Institute was used to record reflectivity changes. Rainfall detection and amount data were collected from the ground-based observation network within the seeding particle diffusion range and time. In addition, the reflectivity before and after the experiment and the size distribution of the raindrops by field observations, such as by micro rain radar and disdrometer, were analyzed.

To verify the effectiveness of the cloud seeding experiment, a numerical simulation was performed using a weather research and forecasting (WRF) model. The Morrison microphysical scheme [58] of the WRF model was modified for the cloud seeding experiment, which was successfully simulated for orographic cloud in the winter [59].

3. Results and Discussion

3.1. Description of Cloud Seeding Experiment. Processes, such as weather forecast analysis, seeding scenario establishment, and licensing for aircraft operations, were conducted prior

to the cloud seeding experiment. The experiment was conducted by observing variations in atmospheric conditions and cloud particles using the NARA after spraying cloud seeding material using the UAV. This was conducted on April 25, 2019, during which the UAV flew from 0912 to 1037 local standard time (LST) (85 min) and the NARA flew from 0930 to 1254 LST (204 min). The UAV sprayed the cloud seeding material from 0917 to 1029 LST (72 min). The study area included Goheung and Boseong, Jeollanam-do. Figure 2 shows the target area and flight path of seeding by the UAV and the observation by the NARA over the southern part of the Korean peninsula. The UAV seeded the clouds using 12 calcium chloride flares at a height of 760 m on the windward side of the area; the NARA traveled straight at 1-2 km in height on the windward and leeward sides.

3.2. Weather Conditions during Cloud Seeding Experiment. Investigating whether the weather conditions were suitable before the cloud seeding experiment was a major factor influencing its success. Moreover, the seeding material species are dependent on the threshold for atmospheric temperature. Thus, the threshold value and weather conditions were compared (Table 2). Table 2 provides the weather condition checklist for this experiment. The atmospheric conditions for cloud seeding experiments in warm clouds, as suggested by the NIMS, are a temperature above 0°C, a liquid water content over 0.1 g/m^3, and a wind speed below 15 m/s at the seeding height. The NARA performed the atmospheric conditions at the seeding height to ensure the suitability of these conditions for seeding. The measured conditions were as follows: temperature of 10.1°C, liquid water content of 0.71 g/m^3, and wind speed of 6.9 m/s.

Information on the prevailing synoptic conditions is useful to estimate the movement and characteristics of the cloud system for cloud seeding purposes. The synoptic weather conditions by Unified Model (UM) in KMA and satellite infrared satellite image during this experiment are provided in Figure 3. Figure 3 shows the (a) surface weather chart, (b) the gap between temperature and dew point temperature, dew point temperature, and wind at 850 hPa, (c) the weather chart at 850 hPa, and (d) the temperature at 850 hPa and vertical velocity at 700 hPa at 0900 LST on April 25, 2019. As shown in Figures 3(a) and 3(c), during the experiment, the middle and upper clouds, accompanied by an upper air pressure valley near Balhae Bay, were moving northeast, and the developed low and convective clouds behind them moved northeast to the northern Yellow Sea. As the southwest wind continued to blow from southern China, the dew point deficit in the target area increased from 0 to 1°C (Figure 3(b)), and the vertical velocity was −5 hPa/h, with a weak upward wind (Figure 3(d)). It was presumed that the seeding material sprayed in this moist atmosphere rose vertically and reacted with the cloud particles.

Vertical weather conditions were determined using the vertical sounding profile and (b) precipitable water in Heuksando at 0900 LST and 2100 LST on April 25, 2019. Figure 4 reflects (a) the vertical sounding profile and (b) precipitable water in Heuksando at 0900 LST and 2100 LST on April 25, 2019. In the vertical profile of the atmospheric conditions, shown in Figure 4(a), the lifting condensation level was recorded at approximately 990 hPa, and the K-index increased by 9.2 after the cloud seeding, indicating the possibility of showers or thunderstorms. In Figure 4(b), the precipitable water increased in most areas from the lower to the upper layer. Moreover, the precipitable water at the surface was 0.65–0.76 mm, and the accumulated precipitable water was 1.70–2.39 m. From this vertical profile, it was observed that moisture and unstable cloud conditions were present, making it suitable for conducting cloud seeding experiments.

Information on the cloud characteristics was based on the data obtained from the Communication, Ocean, and Meteorological Satellite (COMS) and is presented in Figure 5. Figure 5 shows the horizontal distribution of the (a) cloud top height, (b) cloud type, (c) cloud top temperature, and (d) cloud optical depth at 1030 LST, as well as the (e) time series of cloud top height (grey), cloud thickness (green), observed height by the aircraft (black), cloud top temperature (red), liquid water path (blue), cloud base height (red triangle), and cloud type (character) on April 25, 2019. As shown in Figure 5, the cloud top height was 0.5–2 km (Figure 5(a)), and the cloud top temperature was 5–15°C (Figure 5(c)). The cloud optical thickness was 5–25 (Figure 5(d)), and the total liquid water content was 30–70 g/m^2 (Figure 5(e)). This indicates low stratocumulus clouds with liquid status (Figure 5(b)). This experiment was conducted with the NARA flight design that performed the entire cloud distribution from a cloud base of 0.1 km to a cloud top of 1.7 km. The cloud base height calculated from NARA and satellite data was similar to that from the ceilometer at the Boseong Weather Observatory (BSWO), indicating that stratus clouds with a cloud thickness of 0.2–0.3 km occurred.

3.3. Results of Cloud Seeding Experiment. The results of the cloud seeding were determined using field observations and a numerical simulation.

To analyze the drop-size distribution in the cloud to determine the effect of cloud seeding, the information collected by NARA was utilized as shown in Figure 6, which depicts (a) the flight path map, (b) time series of flight height from 1030 to 1145 LST, and (c) average cloud size distribution at 1 km in height before (cyan) and after seeding (blue) on April 25, 2019. Considering the southeast wind and the spraying height during the cloud seeding (Figure 6(a)), the windward side (the section not affected by the cloud seeding material, shown in cyan) and the leeward side (the section affected by the cloud seeding material, shown in blue) were divided into three layers at 2.0, 1.5, and 1.0 km (Figure 6(b)). During the cloud observation flight, the points marked OB1-1 and OB1-2 were observed windward in the order of 2.0, 1.5, and 1.0 km in height, and the points OB3-1 and OB3-2 were observed leeward in the order of 1.0, 1.5, and 2.0 km in height. As shown in Figure 6(c), at 1 km cloud seeding height, the number concentration of the cloud particles below 10 μm in diameter was similar before and

Figure 2: Target area and flight path of seeding by the UAV (red) and observation by the NARA (blue) over the southern part of the Korean peninsula on April 25, 2019.

Table 2: The weather condition checklist for cloud seeding experiment on April 25, 2019.

	Threshold for warm cloud	Value at seeding height
Temperature (°C)	Over 0.0	10.1
Liquid water content (g/m^3)	Over 0.1	0.71
Wind speed (m/s)	Below 15.0 for enough time for droplet growing	6.9

after seeding. However, the particle size of the cloud particles over 10 μm increased. Therefore, the maximum number concentration decreased, and a wide cloud particle spectrum appeared in 10–100 μm particles because of the competition effect and formation of precipitation by strengthening the collision-coalescence process in the cloud [14]. In addition, the cloud droplets showed a wide cloud particle spectrum in cloud particles over 100 μm through giant cloud condensation nuclei activity that appeared due to the tail effect, accelerating precipitation formation [6, 60]. Table 3 compares the average number concentration (cm^{-3}) before and after cloud seeding at a height of 1 km on April 25, 2019. When comparing the result after seeding to those before the cloud seeding experiment, the cloud particles with diameters of 2–50 μm, as measured using the CDP, had similar number concentrations after the seeding, whereas those particles with diameters of 60–500 μm as measured using the CIP increased 1.52 times, from 12.52 cm^{-3} before to 19.01 cm^{-3} after cloud seeding, which was significant. The NARA observed an increase in the number concentration of cloud particles on the leeward side after the seeding, which is due to the growth of large cloud particles after cloud seeding.

The weather radar detected the sensitive fluctuation of precipitation in the cloud seeding experiment. The variation in the radar reflectivity to determine the effect of the cloud seeding is shown in Figure 7. Figure 7 shows the (a) horizontal distribution of reflectivity at 1100 LST and (b) time series of reflectivity (red solid line with circles) and radar precipitation (blue dotted line with triangles) at BSWO (red point) from 0800 to 1400 LST on April 25, 2019. The pink line in the black box in Figure 7(a) is the area in which the UAV sprayed the cloud seeding material, and the red circle represents the BSWO. As shown in Figure 7, reflectivity near the target area was weak, at −10 to −5 dBZ. Figure 7(b) shows reflectivity near the BSWO, which was less than −10 dBZ before the seeding and less than −15 dBZ during the experiment. After the experiment, the reflectivity increased to −5 dBZ due to the inflow of a weak cloud system. This indicates that the cloud seeding enhanced reflectivity as a result of the reaction of cloud seeding material and the growth of cloud particles. This echoes the result of the AgI Seeding Cloud Impact Investigation project conducted in Wyoming, USA, of an increase in reflectivity of approximately 10 dBZ after cloud seeding [23].

The BSWO data was further used to analyze the variation of rainfall on the surface to determine the effect of the cloud seeding (Figure 8). Figure 8 shows (a) the horizontal distribution of rain detection at 1130 LST, (b) the time series of relative humidity (blue), temperature (red), rain (black), and cloud top height (green), (c) the reflectivity, and (d) the number concentration (black) and diameter (red) of raindrops at BSWO from 0800 to 1500 LST on April 25, 2019. After the cloud seeding experiment, rainfall detection showed at the target Beolgyo (BG), Gwangyang-si (GYS), and Hadong

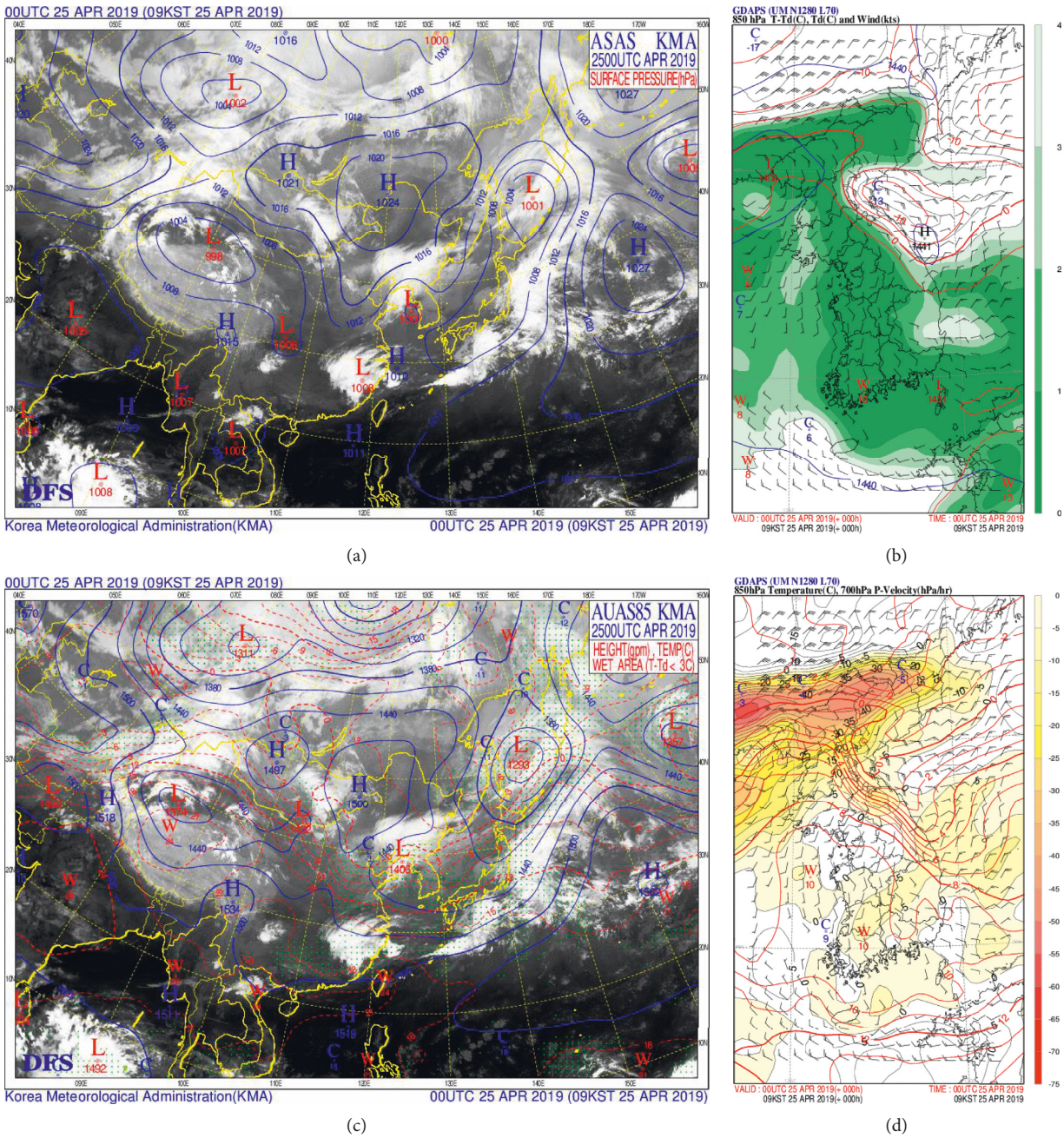

Figure 3: (a) Surface weather chart, (b) gap between temperature and dew point temperature, dew point temperature, wind at 850 hPa, (c) weather chart at 850 hPa, and (d) temperature at 850 hPa and vertical velocity at 700 hPa at 0900 LST on April 25, 2019.

(HD) AWS sites (Figure 8(a)). At the BSWO site (Figure 8), rain was detected but rainfall was not recorded after the cloud seeding experiment at 1023, 1036, 1045, 1050, or 1053 LST. In addition, these three sites recorded approximately 0.5 mm of precipitation, which was presumed to be a mix of natural precipitation and precipitation caused by seeding. At the BSWO, the relative humidity was 84–94% (humid conditions), and the temperature decreased by more than 1°C after the experiment (Figure 8(b)). In Figures 8(c) and 8(d), the cloud seeding time is shown in a red box, and the cloud seeding effect time is shown in a purple box. After cloud seeding, the reflectivity increased by approximately 10 dBZ at 750 m in height at 1120 LST. Additionally, the average number concentration of the raindrop particles increased rapidly, and raindrops of approximately 0.2 mm were recorded from 1100 to 1135 LST. Although rainfall was not observed at the BSWO at 1100 LST, the effects of the seeding could be estimated through rainfall detection, increased reflectivity, and the increased number concentration and size of the raindrops.

A numerical model is a useful tool to estimate the dispersion of seeding material and the increase in rain

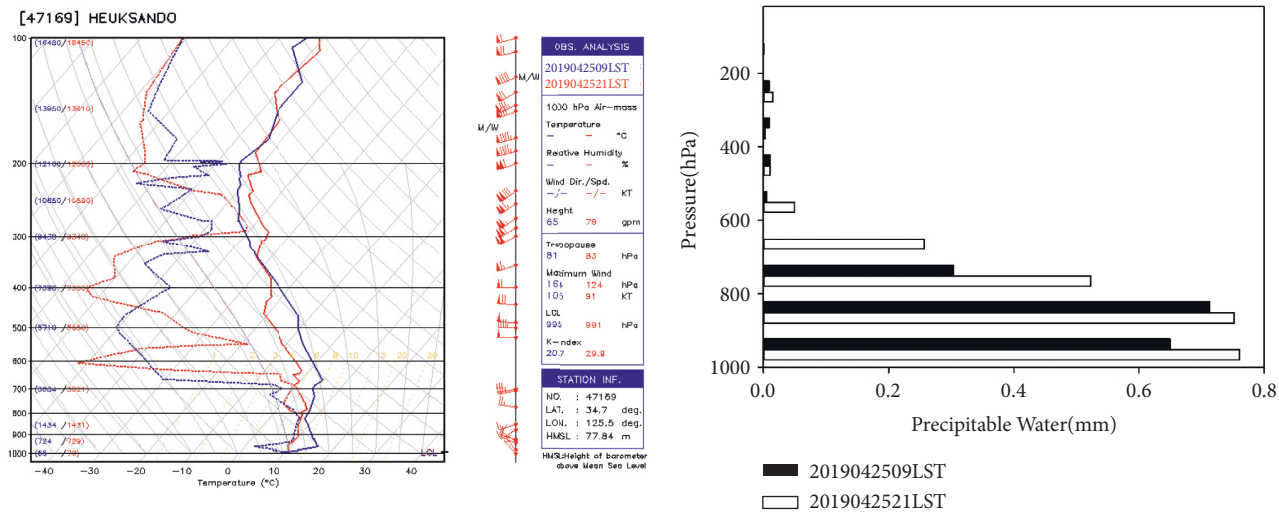

Figure 4: (a) Vertical sounding profile of sounding and (b) precipitable water in Heuksando at 0900 LST and 2100 LST on April 25, 2019.

during a cloud seeding experiment because the classification of natural and artificial (by cloud seeding effect) precipitation is complex. The modified numerical model simulation was used to verify the dispersion of seeding material during the cloud seeding experiment (Figure 9). Figure 9 shows the numerical simulation of the horizontal distribution of the seeding material dispersion (calcium chloride ($CaCl_2$)) at (a) 0930, (b) 1030, and (c) 1130 LST as well as precipitation differences at (d) 0930–1030, (e) 1030–1130, and (f) 1130–1230 LST on April 25, 2019. Figure 9 shows a numerical simulation performed using the WRF model with Unified Model-Local Data Assimilation and Prediction System analysis data and global positioning system location information as input data [61]. In Figures 9(a)–9(c), the shaded area indicates the distribution of the number concentration of the seeding material (calcium chloride), and the vector represents the wind field at 0.75 height. The seeding material after being sprayed dispersed throughout the points of Boseong (BS), BSWO, BG, Gwangyang-eup (GYU), GYS, and Geumnam (GN). The cloud seeding material at seeding height spread to the BS, BSWO, BG, GYU, and GYS points due to the southeast wind but gradually spread northwest over time. In Figures 9(d)– 9(f), the red and blue colors indicate an increase and decrease in precipitation, respectively. Figures 9(d)–9(f) show that the accumulated rain amount increased in the northwest portions of BS and BSWO, where the seeding material dispersed gradually. Three hours after the cloud seeding experiment, the accumulated rain amount increased to 5.1 mm at 1210 LST (not shown). This is a sufficient response time for calcium chloride, as a hygroscopic material, to react with clouds and precipitation; therefore, this was an effect of the cloud seeding experiment.

3.4. Designing Cloud Seeding Experiments Using Two Vehicles. A successful cloud seeding experiment using two types of aircraft can be conducted to mitigate the disadvantages of atmospheric research aircraft. Atmospheric research aircraft have difficulty flying in low clouds. The UAV used for this study can fly in low clouds. Thus, the most important aspect of cloud seeding experiments using UAVs and atmospheric research aircraft is the experimental design. For the two aircraft to perform effectively and coordinated manner during cloud seeding experiments without safety concerns, the experiment must be designed considering temporal and spatial conditions. Figure 10 shows a schematic diagram of the cloud seeding experiment using the UAV (red) and the NARA (blue). As shown in Figure 10, the UAV should perform the cloud seeding first, and the atmospheric research aircraft should subsequently observe the meteorological conditions. Spatially, the experiment can be designed by dividing it into vertical and horizontal areas. Vertically, UAVs should fly in the lower regions of the clouds, and atmospheric research aircraft should fly in the middle and upper levels of the clouds, maintaining at least a hundred meters between the two aircraft to reduce safety problems and accidents. A previous study [50] emphasized maintaining a 100–300 m interval between the two aircraft; thus, this experiment was conducted with an interval of 240–1280 m. Horizontally, the atmospheric research aircraft must fly in a verification area where ground-based observation equipment is installed, and UAVs must fly in the seeding area of the target cloud. Cloud seeding experiments can be verified in various ways (ground-based and upper layers). Overall, when designing cloud seeding experiments using multiple aircraft, the UAV should spray cloud seeding material near the cloud base over the experimental area first, and atmospheric research aircraft should observe the

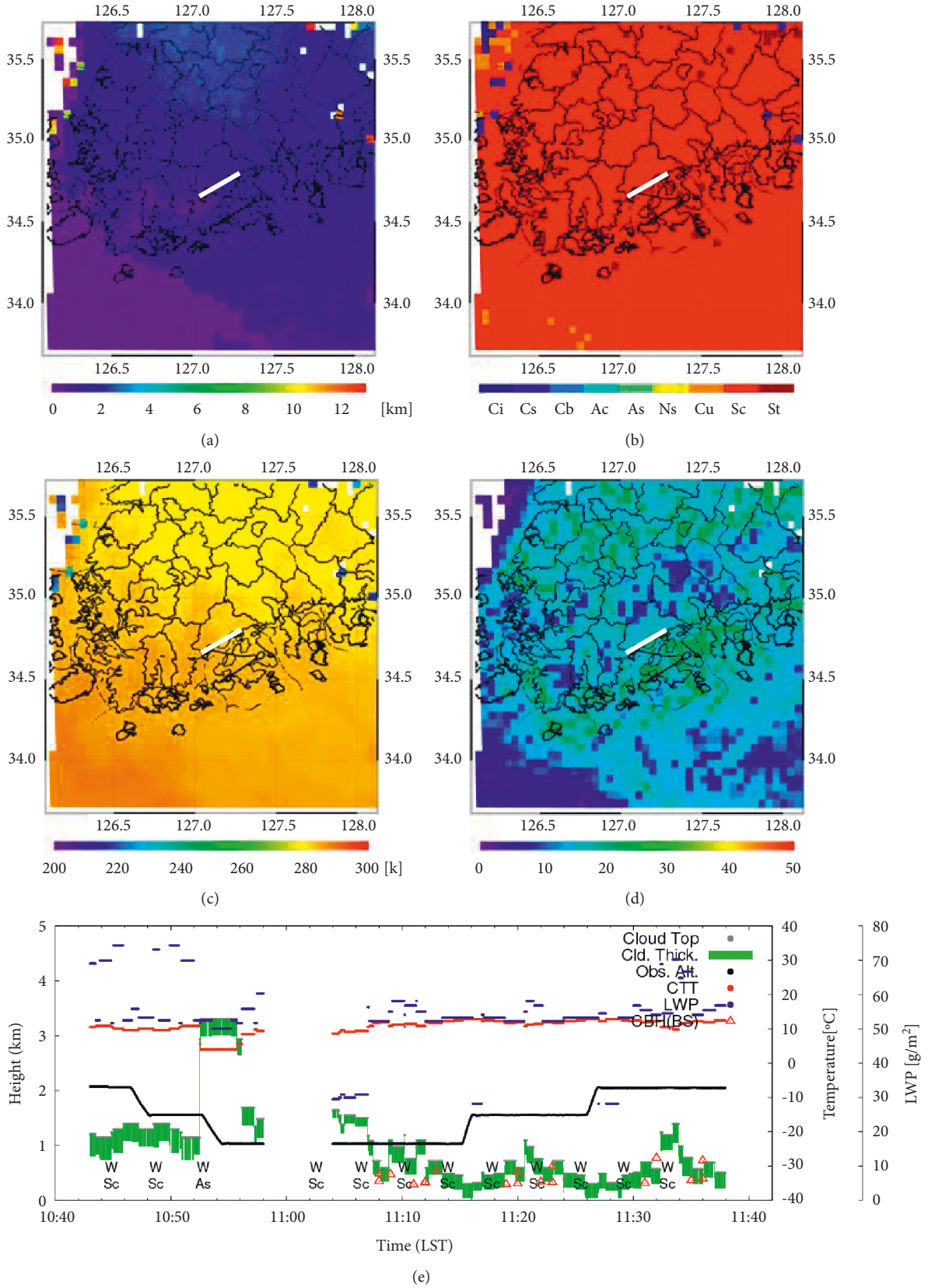

Figure 5: Horizontal distribution of (a) cloud top height, (b) cloud type, (c) cloud top temperature, (d) cloud optical depth at 1030 LST, and (e) time series of cloud top height (grey), cloud thickness (green), observed height by aircraft (black), cloud top temperature (red), liquid water path (blue), cloud base height (red triangle), and cloud type (character) on April 25, 2019.

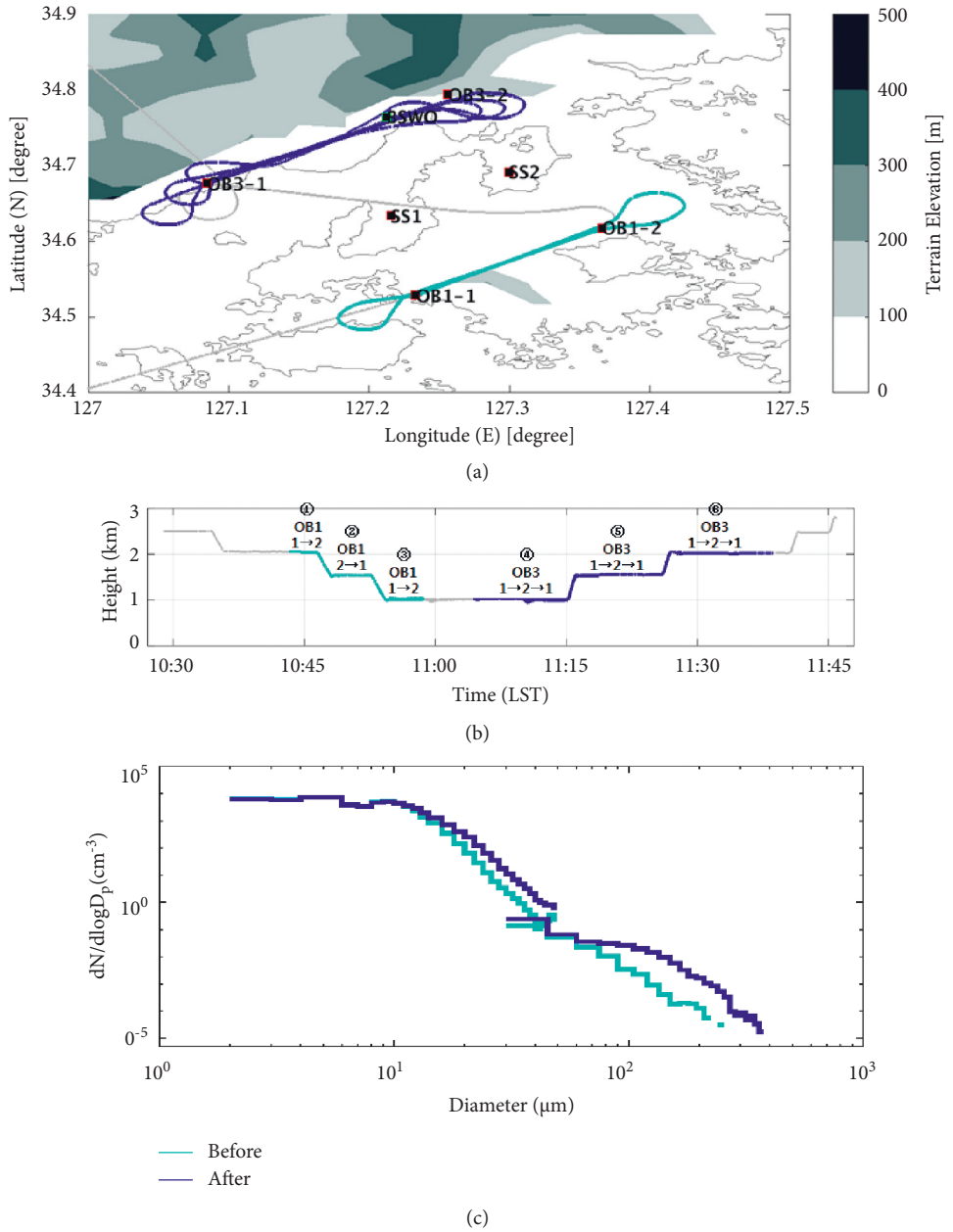

Figure 6: (a) Flight path map, (b) time series of flight height from 1030 to 1145 LST, and (c) average cloud size distribution at 1 km height before (cyan) and after seeding (blue) on April 25, 2019.

Table 3: Comparison of average cloud number concentration (cm^{-3}) between before and after cloud seeding at 1 km height on April 25, 2019.

	Small cloud droplet (2~50 μm)	Large cloud droplet (60~500 μm)
Before cloud seeding (cm^{-3})	4671.05	12.52
After cloud seeding (cm^{-3})	4648.38	19.01
Variance	1.00 time	1.52 times

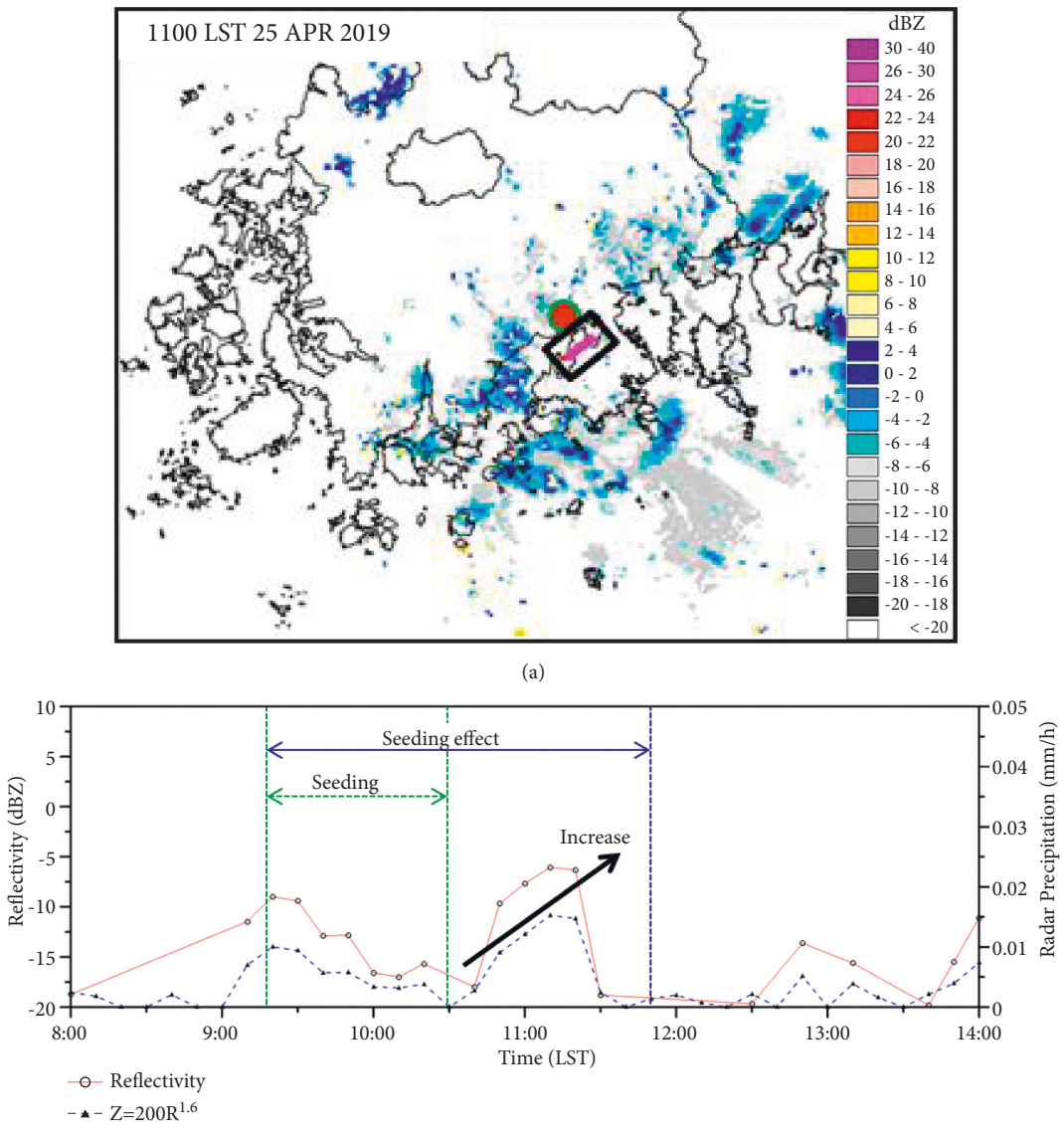

Figure 7: (a) Horizontal distribution of reflectivity at 1100 LST and (b) time series of reflectivity (red solid line with circle) and radar precipitation (blue dotted line with triangle) at BSWO (red point) from 0800 to 1400 LST on April 25, 2019.

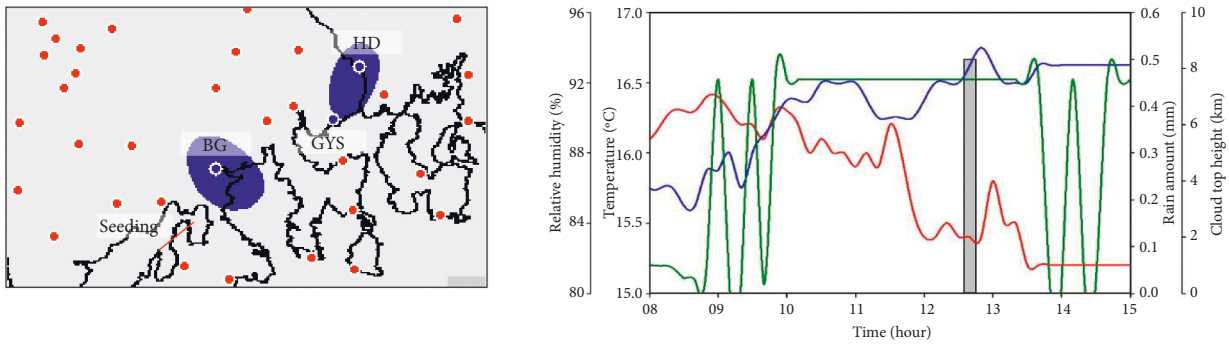

Figure 8: Continued.

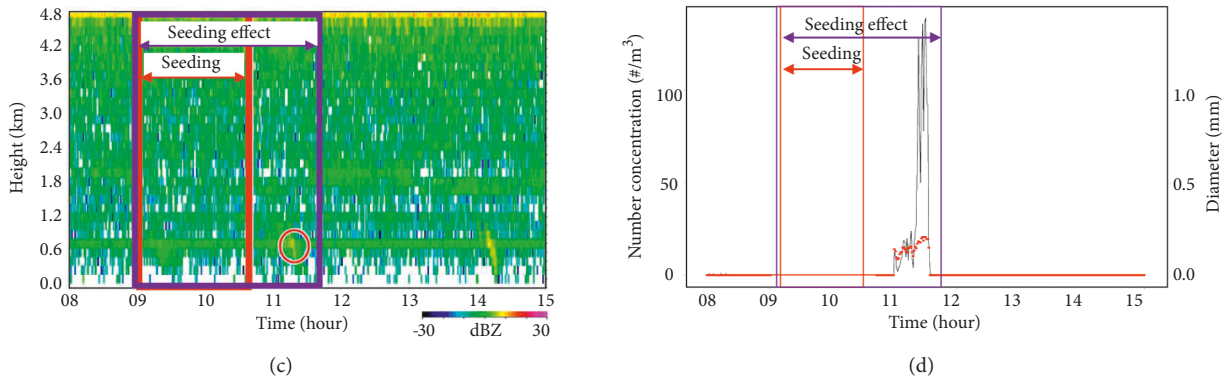

Figure 8: (a) Horizontal distribution of rain detection at 1130 LST, (b) time series of relative humidity (blue), temperature (red), rain (black), cloud top height (green), (c) reflectivity, and (d) number concentration (black) and diameter (red) of raindrop at BOWO from 0800 to 1500 LST on April 25, 2019.

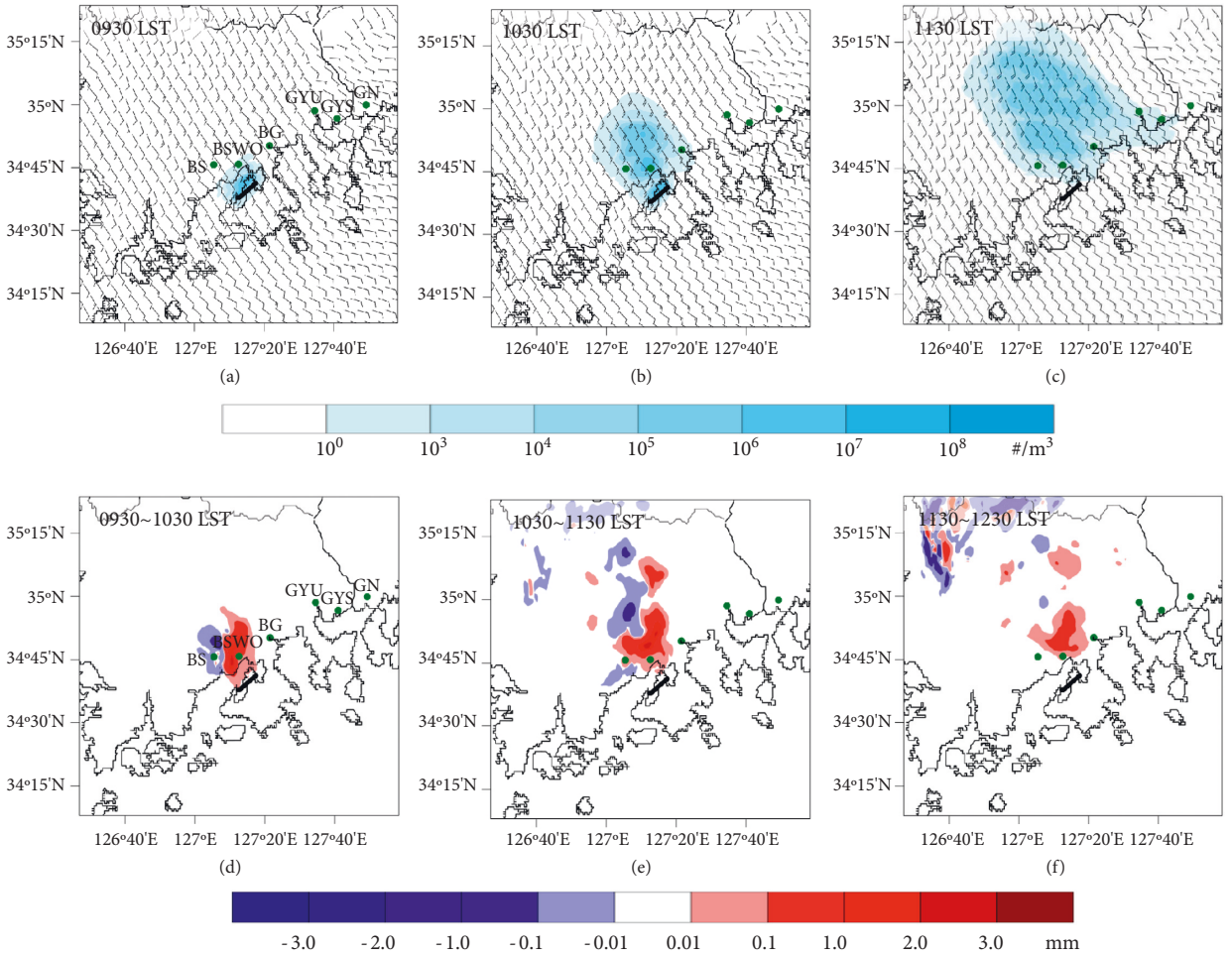

Figure 9: Horizontal distribution of seeding material dispersion (calcium chloride ($CaCl_2$)) at (a) 0930, (b) 1030, and (c) 1130 LST and precipitation difference at (d) 0930–1030, (e) 1030–1130, and (f) 1130–1230 LST on April 25, 2019, by numerical simulation.

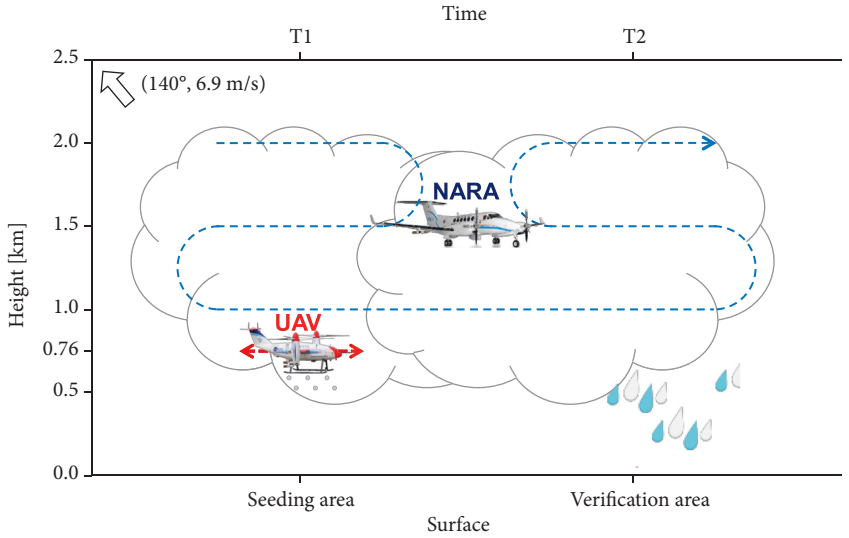

Figure 10: Schematic diagram of cloud seeding experiment by UAV (red) and NARA (blue).

atmospheric conditions in the middle and upper cloud layers over the verification area at a later stage. Effective and safe cloud seeding experiments and verification can therefore be conducted by using these two types of aircraft. This study (especially, Figure 10) will serve as a guideline for cloud seeding experiment using two or several aircraft.

4. Conclusions

This study investigated for the first time in Korea the possibility of cloud seeding using crewed atmospheric research aircraft and UAVs. A thorough experimental design was prepared to spray cloud seeding material with the UAV and to observe the cloud physics by using the NARA. The meteorological conditions (temperature, liquid water content, and wind speed) on April 25, 2019, were suitable for cloud seeding experiments using calcium chloride as seed material. It showed that there were low clouds with liquid status, moist conditions, and a 0-1°C dew point deficit in the experimental area. Observations showed an increase in the number concentration of cloud particles over 10 μm in diameter, an increase in radar reflectivity of over 10 dBZ, rainfall detection, and an increase in the number concentration and size of the raindrops. Moreover, a numerical simulation showed the dispersion of the cloud seeding material. Therefore, the growth of the clouds and raindrops was likely due to the cloud seeding experiment. The analysis criteria for cloud seeding effects proposed by the NIMS and KMA are increased surface precipitation, cloud particles, and radar reflectivity [45]; thus, this study shows suitable results.

Although increases in precipitation and clouds in the target area after the experiment were indicated, this may have been a natural increase. Therefore, statistical verification through more experiments is needed. Although this was the first cooperative experiment using UAVs and atmospheric research aircraft in Korea, we expect to see similar experiments from other researchers and collaborative operators. Priority for investment to develop further weather modification technologies was analyzed using the 10 indicators for 16 technologies and noted that the development of new weather sensors for UAVs, spraying and diffusion of cloud seeding material, verification, numerical modelling, and ground-based experiments are required [62]. Therefore, the KMA will continue to strive for technology development in cloud seeding experiments using UAVs and atmospheric research aircraft. In the future, we plan to improve cloud seeding efficiency using UAVs through continued dual aircraft experiments.

Data Availability

The data that support the funding of this study are available from the corresponding author from NIMS, KMA, Korea.

Conflicts of Interest

The authors declare that there are no conflicts of interest regarding the publication of this paper.

Acknowledgments

This work was funded by the Korea Meteorological Administration Research and Development Program "Research on Weather Modification and Cloud Physics" under Grant KMA2018-00224.

References

[1] S. Solomon, D. Qin, M. Manning et al., *Climate Change 2007, The Physical Science Basis*, Cambridge University Press, Cambridge, UK, 2007.

[2] V. J. Schaefer, "The production of ice crystals in a cloud of supercooled water droplets," *Science*, vol. 104, no. 2707, pp. 457–459, 1946.

[3] B. Vonnegut, "The nucleation of ice formation by silver iodide," *Journal of Applied Physics*, vol. 18, no. 7, pp. 593–595, 1947.

[4] B. Vonnegut, "Misconception about cloud seeding with dry ice," *Journal of Weather Modification*, vol. 13, pp. 9-10, 1981.

[5] A. S. Dennis, *Weather Modification by Cloud Seeding*, Academic Press, New York, NY, USA, 1980.

[6] D. Rosenfeld, D. Axisa, W. L. Woodley, and R. Lahav, "A quest for effective hygroscopic cloud seeding," *Journal of Applied Meteorology and Climatology*, vol. 49, no. 7, pp. 1548–1562, 2010.

[7] J. A. Warburton, L. G. Young, and R. H. Stone, "Assessment of seeding effects in snowpack augmentation programs: ice nucleation and scavenging of seeding aerosols," *Journal of Applied Meteorology*, vol. 34, no. 1, pp. 121–130, 1995.

[8] World Meteorological Organization (WMO), A. I. Flossmann, M. Manton et al., *Peer Review Report on Global Precipitation Enhancement Activities*, WWRP, Geneva, Switzerland, 2018.

[9] R. T. Bruintjes, "A review of cloud seeding experiments to enhance precipitation and some new prospects," *Bulletin of the American Meteorological Society*, vol. 80, no. 5, pp. 805–820, 1999.

[10] B.-Y. Kim, J. W. Cha, W. Jung, and A.-R. Ko, "Precipitation enhancement experiments in catchment areas of dams: evaluation of water resource augmentation and economic benefits," *Remote Sensing*, vol. 12, no. 22, p. 3730, 2020.

[11] E. K. Bigg, "An independent evaluation of a South African hygroscopic cloud seeding experiment, 1991-1995," *Atmospheric Research*, vol. 43, no. 2, pp. 111–127, 1997.

[12] D. Caro, W. Wobrock, and A. I. Flossmann, "A numerical study on the impact of hygroscopic seeding on the development of cloud particle spectra," *Journal of Applied Meteorology*, vol. 41, no. 3, pp. 333–350, 2002.

[13] W. A. Cooper and R. P. Lawson, "Physical interpretation of results from the HIPLEX-1 experiment," *Journal of Climate and Applied Meteorology*, vol. 23, no. 4, pp. 523–540, 1984.

[14] W. A. Cooper, R. T. Bruintjes, and G. K. Mather, "Calculations pertaining to hygroscopic seeding with flares," *Journal of Applied Meteorology*, vol. 36, no. 11, pp. 1449–1469, 1997.

[15] B. Geerts, Q. Miao, Y. Yang, R. Rasmussen, and D. Breed, "An airborne profiling radar study of the impact of glaciogenic cloud seeding on snowfall from winter orographic clouds," *Journal of the Atmospheric Sciences*, vol. 67, no. 10, pp. 3286–3302, 2010.

[16] B. Geerts, Y. Yang, R. Rasmussen, S. Haimov, and B. Pokharel, "Snow growth and transport patterns in orographic storms as estimated from airborne vertical-plane dual-doppler radar data," *Monthly Weather Review*, vol. 143, no. 2, pp. 644–665, 2015.

[17] T. W. Krauss, R. T. Bruintjes, J. Verlinde, and A. Kahn, "Microphysical and radar observations of seeded and non-seeded continental cumulus clouds," *Journal of Climate and Applied Meteorology*, vol. 26, no. 5, pp. 585–606, 1987.

[18] P. A. Kucera, D. Axisa, R. P. Burger et al., "Features of the weather modification assessment project in the southwest region of Saudi Arabia," *Journal of Weather Modification*, vol. 42, pp. 78–103, 2010.

[19] J. R. Kulkarni, R. S. Maheshkumar, S. B. Morwal et al., "The cloud aerosol interaction and precipitation enhancement experiment (CAIPEEX): overview and preliminary results," *Current Science*, vol. 102, no. 3, pp. 413–425, 2012.

[20] G. K. Mather, D. E. Terblanche, F. E. Steffens, and L. Fletcher, "Results of the South African cloud-seeding experiments using hygroscopic flares," *Journal of Applied Meteorology*, vol. 36, no. 11, pp. 1433–1447, 1997.

[21] B. A. Silverman, "An independent statistical reevaluation of the South African hygroscopic flare seeding experiment," *Journal of Applied Meteorology*, vol. 39, no. 8, pp. 1373–1378, 2000.

[22] B. A. Silverman, "A critical assessment of hygroscopic seeding of convective clouds for rainfall enhancement," *Bulletin of the American Meteorological Society*, vol. 84, no. 9, pp. 1219–1230, 2003.

[23] B. Pokharel, B. Geerts, X. Jing et al., "The impact of ground-based glaciogenic seeding on clouds and precipitation over mountains: a multi-sensor case study of shallow precipitating orographic cumuli," *Atmospheric Research*, vol. 147-148, no. 148, pp. 162–182, 2014.

[24] B. Pokharel, B. Geerts, X. Jing, K. Friedrich, K. Ikeda, and R. Rasmussen, "A multi-sensor study of the impact of ground-based glaciogenic seeding on clouds and precipitation over mountains in wyoming. part II: seeding impact analysis," *Atmospheric Research*, vol. 183, pp. 42–57, 2017.

[25] M. Pósfai, D. Axisa, É. Tompa, E. Freney, R. Bruintjes, and P. R. Buseck, "Interactions of mineral dust with pollution and clouds: an individual-particle TEM study of atmospheric aerosol from Saudi Arabia," *Atmospheric Research*, vol. 122, pp. 347–361, 2013.

[26] E. Tas, A. Teller, O. Altaratz et al., "The relative dispersion of cloud droplets: its robustness with respect to key cloud properties," *Atmospheric Chemistry and Physics*, vol. 15, no. 4, pp. 2009–2017, 2015.

[27] W. L. Woodley, D. Rosenfel, and B. A. Silverman, "Results of on-top glaciogenic cloud seeding in Thailand. Part I: the demonstration experiment," *Journal of Applied Meteorology*, vol. 42, no. 7, pp. 920–938, 2003.

[28] W. L. Woodley, D. Rosenfeld, and B. A. Silverman, "Results of on-top glaciogenic cloud seeding in Thailand. Part II: exploratory analyses," *Journal of Applied Meteorology*, vol. 42, no. 7, pp. 939–951, 2003.

[29] W. L. Woodley and D. Rosenfeld, "The development and testing of a new method to evaluate the operational cloud-seeding programs in Texas," *Journal of Applied Meteorology*, vol. 43, no. 2, pp. 249–263, 2004.

[30] D. Breed, R. Rasmussen, C. Weeks, B. Boe, and T. Deshler, "Evaluating winter orographic cloud seeding: design of the wyoming weather modification pilot project (WWMPP)," *Journal of Applied Meteorology and Climatology*, vol. 53, no. 2, pp. 282–299, 2014.

[31] Colorado Water Conservation Board, *Inventory and Assessment of Colorado Weather Modification Programs: A Summary of Current Programs and Opportunities for Enhancement, CWCB Reports*, Colorado Water Conservation Board, Colorado, Denver, USA, 2015.

[32] R. M. Rauber, B. Geerts, L. Xue et al., "Wintertime orographic cloud seeding-a review," *Journal of Applied Meteorology and Climatology*, vol. 58, no. 10, pp. 2117–2140, 2019.

[33] B. A. Silverman, "An evaluation of eleven operational cloud seeding programs in the watersheds of the Sierra Nevada Mountains," *Atmospheric Research*, vol. 97, no. 4, pp. 526–539, 2010.

[34] S. A. Tessendorf, J. R. French, K. Friedrich et al., "A transformational approach to winter orographic weather modification research: the SNOWIE project," *Bulletin of the American Meteorological Society*, vol. 100, no. 1, pp. 71–92, 2019.

[35] S. A. Tessendorf, R. T. Bruintjes, C. Weeks et al., "The Queensland cloud seeding research program," *Bulletin of the American Meteorological Society*, vol. 93, no. 1, pp. 75–90, 2012.

[36] Z. Levin, N. Halfon, and P. Alpert, "Reassessment of rain enhancement experiments and operations in Israel including synoptic considerations," *Atmospheric Research*, vol. 97, no. 4, pp. 513–525, 2010.

[37] A. Samaddar, Y. Roohani, S. Ghosh, and B. V. Rao, "Microphysical characterization of cloud seeding experiments in India," *Asian Journal of Water Environment*, vol. 1, no. 1, 2013.

[38] A. I. Flossmann, M. Manton, A. Abshaev et al., "Review of advances in precipitation enhancement research," *Bulletin of the American Meteorological Society*, vol. 100, no. 8, pp. 1465–1480, 2019.

[39] I. K. Yang, "Basic investigation and preliminary field test for precipitation enhancement," *Asia–Pacific Journal of Atmospheric Science*, vol. 1, pp. 8–13, 1965.

[40] M.-J. Lee, K.-H. Chang, G.-M. Park et al., "Preliminary results of the ground-based orographic snow enhancement experiment for the easterly cold fog (cloud) at daegwallyeong during the 2006 winter," *Advances in Atmospheric Sciences*, vol. 26, no. 2, pp. 222–228, 2009.

[41] C. Lee, K.-H. Chang, J.-W. Cha et al., "Estimation for the economic benefit of weather modification (precipitation enhancement and for dissipation)," *Atmosphere*, vol. 20, no. 2, pp. 187–194, 2010.

[42] C. Lee, K.-H. Chang, J.-W. Jung, J.-W. Cha, Y.-J. Choi, and K. Kim, "Strategy for the meteorological and environmental airborne observations over the Korean Peninsula," *Asia-Pacific Journal of Atmospheric Sciences*, vol. 47, no. 1, pp. 91–96, 2011.

[43] H.-Y. Yang, K.-H. Chang, S. Chae et al., "Case study of ground-based glaciogenic seeding of clouds over the pyeongchang region," *Advances in Meteorology*, vol. 2018, Article ID 9465923, 16 pages, 2018.

[44] J. W. Cha, S. Seo, H.-Y. Yang et al., *Principle and Application of Precipitation Enhancement*, NIMS Technical Note, Jeju, Republic of Korea, 2018.

[45] J. W. Cha, W. Jung, S. Chae et al., "Analysis of results and technics about precipitation enhancement by aircraft seeding in Korea," *Atmosphere*, vol. 29, no. 4, pp. 481–499, 2019.

[46] W. Jung, K.-H. Chang, A.-R. Ko et al., "Meteorological conditions for the cloud seeding experiment by aircraft in Korea," *Journal of Environmental Science International*, vol. 30, no. 12, pp. 1027–1039, 2021.

[47] W. Jung, K.-H. Chang, J. W. Cha, J. M. Ku, and C. Lee, "Estimation of available days for a cloud seeding experiment in Korea," *Journal of Environmental Science International*, vol. 31, no. 2, pp. 117–129, 2022.

[48] D. Axisa and T. P. DeFelice, "Modern and prospective technologies for weather modification activities: a look at integrating unmanned aircraft systems," *Atmospheric Research*, vol. 178-179, pp. 114–124, 2016.

[49] T. S. Bates, P. K. Quinn, J. E. Johnson et al., "Measurements of atmospheric aerosol vertical distributions above Svalbard, Norway, using unmanned aerial systems (UAS)," *Atmospheric Measurement Techniques*, vol. 6, no. 8, pp. 2115–2120, 2013.

[50] T. P. Defelice and D. Axisa, "Modern and prospective technologies for weather modification activities: developing a framework for integrating autonomous unmanned aircraft systems," *Atmospheric Research*, vol. 193, pp. 173–183, 2017.

[51] S. G. Gupta, M. M. Ghonge, and P. M. Jawandhiya, "Review of unmanned aircraft system (UAS)," *International Journal of Advanced Research in Computer Engineering and Technology*, vol. 2, no. 4, pp. 1646–1658, 2013.

[52] E. Frew, J. Elston, B. Argrow, A. Houston, and E. Rasmussen, "Sampling severe local storms and related phenomena: using unmanned aircraft systems," *IEEE Robotics and Automation Magazine*, vol. 19, no. 1, pp. 85–95, 2012.

[53] D. Brus, J. Gustafsson, V. Vakkari, O. Kemppinen, G. de Boer, and A. Hirsikko, "Measurement report: properties of aerosol and gases in the vertical profile during the LAPSE-RATE campaign," *Atmospheric Chemistry and Physics*, vol. 21, no. 1, pp. 517–533, 2021.

[54] B.-J. Park, Y.-S. Kang, C.-S. Yoo, and A. Cho, "Development of operational flight program for smart UAV," *Journal of the Korean Society for Aeronautical & Space Sciences*, vol. 41, no. 10, pp. 805–812, 2013.

[55] Y.-S. Kang, B.-J. Park, A. Cho, and C.-S. Yoo, "Control law design for a tilt-rotor unmanned aerial vehicle with a nacelle mounted WE (wing extension)," *Journal of Institute of Control, Robotics and Systems*, vol. 20, no. 11, pp. 1103–1111, 2014.

[56] Y. Kang, B.-J. Park, A. Cho, C.-S. Yoo, S.-O. Koo, and M.-J. Tahk, "Development of flight control system and troubleshooting on flight test of a tilt-rotor unmanned aerial vehicle," *International Journal of Aeronautical and Space Sciences*, vol. 17, no. 1, pp. 120–131, 2016.

[57] S.-P. Jung, C. Lee, J.-H. Kim et al., "Thermodynamic characteristics of snowfall clouds using dropsonde data during ICE–POP 2018," *Atmosphere*, vol. 30, no. 1, pp. 1–16, 2020.

[58] H. Morrison, G. Thompson, and V. Tatarskii, "Impact of cloud microphysics on the development of trailing stratiform precipitation in a simulated squall line: comparison of one- and two-moment schemes," *Monthly Weather Review*, vol. 137, no. 3, pp. 991–1007, 2009.

[59] C. K. Kim, S. S. Yum, and Y.-S. Park, "A numerical study of winter orographic seeding experiments in Korea using the weather research and forecasting model," *Meteorology and Atmospheric Physics*, vol. 128, no. 1, pp. 23–38, 2016.

[60] Y. Segal, A. Khain, M. Pinsky, D. Rosenfeld, and A. KhAin, "Effects of hygroscopic seeding on raindrop formation as seen from simulations using a 2000-bin spectral cloud parcel model," *Atmospheric Research*, vol. 71, no. 1-2, pp. 3–34, 2004.

[61] S. Chae, K.-H. Chang, S. Seo et al., "Numerical simulations of airborne glaciogenic cloud seeding using the WRF model with the modified Morrison scheme over the Pyeongchang region in the winter of 2016," *Advances in Meteorology*, vol. 2018, Article ID 8453460, 15 pages, 2018.

[62] J. Y. Lim, K. Kim, D. Won, and W.-D. Yeo, "Priority for the investment of artificial rainfall fusion technology," *The Journal of the Korea Contents Association*, vol. 19, no. 3, pp. 261–274, 2019.

Hindawi
Advances in Meteorology
Volume 2022, Article ID 7920779, 10 pages
https://doi.org/10.1155/2022/7920779

Research Article

Harmonization and Verification of Three National European Icing Forecast Models Using Pilot Reports

Christoph Knigge,[1] **Katie Bennett**,[2] **Christine Le Bot**,[3] **Mara Gehlen-Zeller**,[1] **and Svenja Koos**[1]

[1]*Deutscher Wetterdienst, Offenbach Am Main, Germany*
[2]*UK Met Office, Exeter, UK*
[3]*Météo-France, Toulouse, France*

Correspondence should be addressed to Christoph Knigge; christoph.knigge@dwd.de

Received 5 November 2021; Revised 22 March 2022; Accepted 20 April 2022; Published 26 May 2022

Academic Editor: Thomas Hauf

The Single European Sky Air Traffic Management Research (SESAR) program aims at modernizing and harmonizing the European airspace, which currently has a strongly fragmented character. Besides turbulence and convection, in-flight icing is part of SESAR and can be seen as one of the most important meteorological phenomena, which may lead to hazardous flight conditions for aircraft. In this study, several methods with varying complexities are analyzed for combining three individual in-flight icing forecasts based on numerical weather prediction models from Deutscher Wetterdienst, Météo-France, and Met Office. The optimal method will then be used to operate one single harmonized in-flight icing forecast over Europe. As verification data, pilot reports (PIREPs) are used, which provide information about hazardous weather and are currently the only direct regular measure of in-flight icing events available. In order to assess the individual icing forecasts and the resulting combinations, the probability of detection skill score is calculated based on multicategory contingency tables for the forecast icing intensities. The scores are merged into a single skill score to give an overview of the quality of the icing forecast and enable comparison of the different model combination approaches. The concluding results show that the most complex combination approach, which uses iteratively optimized weighting factors for each model, provides the best forecast quality according to the PIREPs. The combination of the three icing forecasts results in a harmonized icing forecast that exceeds the skill of each individual icing forecast, thus providing an improvement to in-flight icing forecasts over Europe.

1. Introduction

The European airspace has a strongly fragmented character. At the continental scale, there are multiple air navigation service providers each responsible for a portion of the European airspace. Furthermore, air traffic control in Europe is very complex because the airspace is one of the busiest in the world with over 30,000 flights daily on average (2018, before COVID-19 pandemic) and a very high airport density. In the year 2000, the Single European Sky initiative was created to structure airspace and air navigation services in Europe to overcome the fragmentation and increase flight capacity and air traffic management efficiency. The Single European Sky Air Traffic Management Research (SESAR) program aims at modernizing and harmonizing the European airspace through the development and implementation of a new set of operational procedures and systems among European aviation stakeholders [1, 2].

In order to achieve the goals of SESAR, aeronautical and meteorological information need to be harmonized and consistent over Europe. Several national meteorological service providers operate their own Numerical Weather Prediction (NWP) systems on various grid scales (global to regional) and time scales resulting in several weather forecasts available over Europe at any given time. Additionally, harmonized global aviation weather forecasts provided by the World Area Forecast Centre's are available. However, for the highly fragmented and high-capacity European airspace, there is a need for more detailed weather forecast information (high-resolution aeronautical

meteorological (MET) information for short-distance flights, terminal areas, and airports). The SESAR Deployment project [3] 2015_068_AF5 "European Harmonised Forecasts of Adverse Weather (Icing, Turbulence, Convection and Winter Weather)" aims at fulfilling this need by providing European harmonized MET products of aviation weather hazards in high resolution and of high accuracy.

Alongside turbulence and convection, in-flight icing is seen as one of the most important meteorological phenomena, which may lead to hazardous flight conditions for aircraft. In-flight icing typically occurs in clouds with supercooled water droplets. The temperature within these clouds is usually between 0 and -20°C [4] and can be, depending on the surrounding conditions (such as the absence of ice nuclei), as cold as -40°C [5]. An aircraft flying through such a cloud may collect some of the supercooled droplets on its wings, propellers, or turbines, measuring instruments and other structures of the aircraft. The droplets freeze instantaneously in contact with the aircraft (large droplets may remain in a semi-liquid state for up to one second [5]) and can accrete to form an ice layer of up to several centimeters [6]. These ice layers can have a strong impact on the maneuverability of the aircraft and may lead to hazardous flight conditions in such a way that measuring instruments and the aircraft aerodynamics are compromised. In the latter case, icing causes an increased drag and a decreased lift, which results in control problems [7]. Green [8] gives a long-term overview (1978–2002) of accidents and incidents related to in-flight icing. Further descriptions of some individual incidents are discussed by Bernstein et al. [9].

Due to the hazardous nature of in-flight icing, aircraft are equipped with anti-icing and de-icing systems. The two most commonly used systems are heated surfaces and pneumatic rubber boots on the leading edge of the wings and at other locations where ice accretion may lead to flight problems. However, their utilization leads to a significant increase in fuel consumption, and therefore, avoidance of icing conditions is preferred. Consequently, there is a demand for more reliable icing forecasts to reduce costs as well as increase flight safety.

In this study, a harmonized icing forecast over Europe is produced using forecast data from Deutscher Wetterdienst (DWD), Météo-France (MF), and Met Office (MO). The three icing forecast products, each based upon a different NWP model, are ADWICE from DWD [5] (postprocessing based on model ICON-EU [10]), ARPEGE from MF [11], and Unified Model (UM) from MO [12]. The harmonized product, hereafter called by its working title "HarmonICE," is produced by combining the different icing indices created by each of the individual NWP models.

The primary goal of this study is to analyze different methods combining the icing indices, such as the minimum, maximum, or mean of all data and, as a more complex approach, the method suggested by Pepe and Thompson [13] described in detail below. The approach with the highest forecast skill will be deployed operationally to provide a harmonized European icing forecast with a high accuracy and consistency across national borders and among airspace users and aviation stakeholders.

Pilot reports (PIREPs) are used to verify the forecasts as supported by previous studies, for example, Brown et al. [14] who describe in detail the advantages and disadvantages of using PIREPs for NWP verification. PIREPs provide information about hazardous weather and are currently the only direct regular measure of in-flight icing events. An overview of the PIREPs used in this study and the methods for the combination of the individual icing forecasts are described in the next section, followed by a detailed description of the results and an outlook.

2. Data and Methods

PIREPs from the winter season 2017/18 (October 2017 to April 2018) are used in order to determine the best approach for combining the three icing forecasts based on single NWP models and to verify the final harmonized icing forecast, HarmonICE. Icing events over Europe typically occur more frequently during this period of the year than in other months. However, compared to the large amount of forecast data available in the time period, there are few observations of the icing phenomenon.

2.1. Observation Data. An icing event reported by a PIREP provides a point observation of the existence and severity of icing (categorized as none, trace, light, moderate, or severe) at the location of the aircraft. Alongside the five-level icing intensity, the geographic location, altitude, and observation time are reported. PIREPs have been used as icing observation data in several other studies such as Brown et al. [14], Taffner et al. [15], and Kalinka et al [5].

In total, 4268 PIREPs were collected during the winter season. The geographical distribution of "no icing" and "icing" events is shown in Figure 1. The majority of the positive icing events were reported over land in the middle of Europe and close to large cities. Aircraft sending these PIREPs were often located at middle flight levels during approach or landing. This can be seen in the altitude distribution of the PIREPs in Figure 2. In contrast, negative reports were mostly sent from over the sea in the western part of the analyzed area (Figure 1) and from higher flight levels (Figure 2). As a result, a large number of "no icing" reports are at heights that are above the maximum forecast level (FL 360) where supercooled liquid water rarely exists due to very low temperatures.

The frequency distributions of the PIREPs separated into four icing intensities can be seen in Figure 3. Trace icing observations are included in the light icing intensity category as there are few trace icing reports compared to light icing reports. By far, most PIREPs report moderate icing. A relatively small number of negative reports are available (662) compared to the number of positive icing events (3606). This distribution can be explained by the fact that pilots are expected to avoid areas with severe icing intensities and that light icing intensities may not give rise to a level of

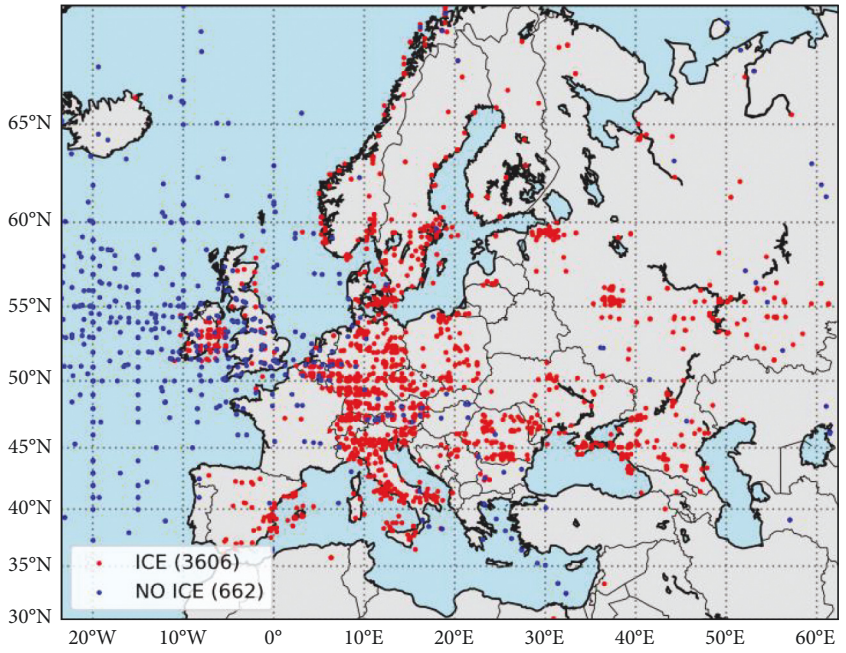

Figure 1: Geographical distribution of the PIREPs used in this study. The area shown represents the geographical coverage of HarmonICE.

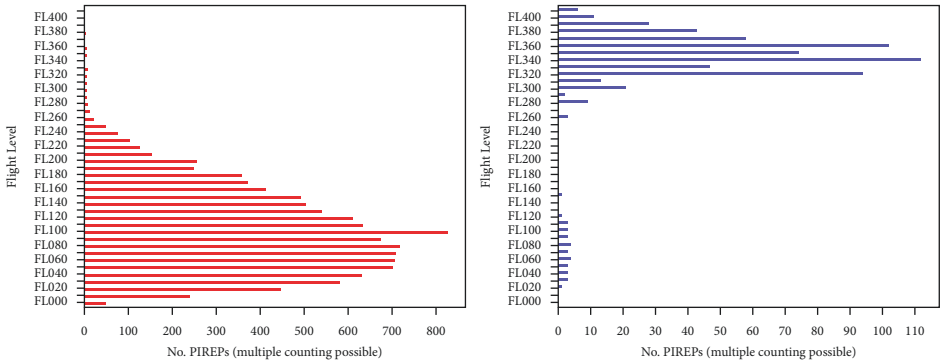

Figure 2: Distribution of the PIREPs by altitude (left: positive icing, right: negative icing). Note that different ranges on the abscissa are shown due to the relatively small number of no icing reports. One report may be counted multiple times because the report identifies multiple levels.

concern for the pilot to consider making a report. Furthermore, icing intensity is subjective since no quantitative definition of severity exists. A detailed discussion about the low quality and quantity of PIREPs is given by Brown et al. [14]. They conclude that PIREPs are challenging to use in an absolute sense for NWP verification. However, in a relative sense, they can be useful, for example, for comparing the detection rates of different icing forecasts or the combination of them as presented in this study.

2.2. Forecast Data. The three icing forecasts used for the harmonized product from DWD, MF, and MO are based on differed NWP systems. ADWICE from DWD provides hourly data output with a horizontal grid spacing of 0.0625° and 32 vertical layers up to 225 hPa. The icing intensities provided by ADWICE match the four categories used for the PIREP values in the study. The icing index based on ARPEGE from MF has a lower horizontal grid resolution of 0.1° and 14 layers up to 400 hPa vertically. The data output is hourly up to forecast hour 12 and then every three hours with an icing intensity range between 1 and 10 in steps of one. The UM icing index from MO provides hourly data with 0.140626° horizontal grid spacing in east-west direction and 0.09375° in north-south direction with 16 vertical grid layers extending up to 250 hPa. The icing intensity is continuous ranging between 0 and 1. All models are run every six hours (0, 6, 12, and 18 UTC) and simulate up to 36 hours or longer.

The different grid spacings and time resolutions have to be considered in the final harmonized product. The approach used for HarmonICE uses the finest of the aforementioned horizontal grid resolutions of 0.0625° and 29 vertical grid layers (up to 225 hPa or flight level 360). This is done so that in the final product, there is no loss of icing intensity information resulting from extrapolation to a

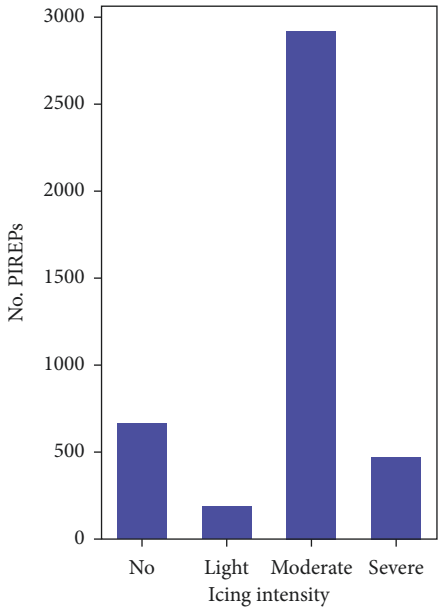

Figure 3: Frequency distribution of the icing intensity.

coarser grid. Furthermore, customers who currently use the finer resolved single product could have reservations against the harmonized product if it contained less information. Any reduction of information in the vertical dimension would result in less flight levels available in the forecasts, reducing the icing intensity information available when compared to existing single model forecasts, which is undesirable for customers. This may give the impression that the harmonized product is not as good as the higher resolved single product and result in reluctance to use HarmonICE.

Data output of HarmonICE is hourly up to forecast hour 36. The final output is the categorical icing intensity forecast utilizing the categories recommended in ICAO Annex 3 [16], which are the same categories used for PIREPs. The domain of HarmonICE goes from 23.5° West to 62.5° East and from 29.5° to 70.5° North (see Figure 1).

In order to combine the three different centers' forecasts, each individual icing forecast is re-gridded to the HarmonICE grid using linear interpolation. Time interpolation is performed with the ARPEGE data, and the icing indices of ARPEGE and UM are transformed to the four-step categorical range of HarmonICE by applying the thresholds listed in Table 1. This transformation is necessary because unlike ADWICE, which produces categorical icing intensity forecasts, there are no internal calculations to a categorical icing intensity within ARPEGE and UM. The thresholds listed in Table 1 were calculated during an earlier phase of the project using PIREPs from another winter season. They are currently fixed at the given values but will be verified and if necessary recalculated in future.

Due to storage problems, some gaps in the forecast data exist for the analyzed winter season 2017/18. All three datasets cover approx. 70% of the complete winter time period so not all PIREPs gathered could be used for comparison with the forecast data. In total, 3010 PIREP forecast data comparisons could be performed.

Table 1: Thresholds used for the transformation of the original icing index potential based on ARPEGE and UM to the four-step range used in HarmonICE.

HarmonICE	ARPEGE	UM
No = 0	0	0–0.59
Light = 1	0.1–3.9	0.6–0.79
Moderate = 2	4.0–7.9	0.8–0.89
Severe = 3	8.0–10.0	0.9–1.0

2.3. Analyzing Methods. This section describes the data processing required to enable evaluation and verification of the forecasts. First, the forecast data corresponding to each PIREP are extracted from the four-dimensional data files. Second, the individual icing forecasts are combined in order to produce the harmonized icing intensity.

2.4. Pairing Data. For each PIREP of the examined winter season, the position, observation time, and icing intensity were compared with the forecast data. The point in time for each PIREP was shifted to the nearest full hour so that a maximum time difference between an icing forecast validity time and the PIREP time was 30 minutes. Within this half-hour window, the detected icing area (cloud) could be advected horizontally some distance according to the mean wind at this altitude leading to some spatial deviation in the location of the icing forecast. Assuming typical mean wind speed of around 15 m/s in a middle altitude of the troposphere, the advection would lead to a distance of around 30 km between the measuring point and the potential new position of the measured cloud half an hour earlier or later. Another source of uncertainty lies in the reported information in the PIREP (e.g., rounding errors of the longitude and latitude values or a time offset during the observation resulting from aircraft travel). In order to account for these uncertainties in time and space, a box was placed around each PIREP and the maximum forecast icing intensity in the box was used to compare to the observed icing intensity (similar to other studies, e.g., Kalinka et al. [5]). The sensitivity of the results to the size of such a box was tested by using four different box sizes. The smallest box is simply a single grid length in all dimensions, which results in a point-to-point comparison. All other boxes are increased vertically by one grid point up and down (totaling three grid points in height), and by one, two, and three grid points, respectively, in all four horizontal directions. Thus, the largest box has dimensions $3 \times 7 \times 7$, totaling 147 grid points, that is, three vertical grid points and seven horizontal grid points in North-South and East-West directions (denoted as 3v7h), corresponding to approximately 600 m vertically and 50 km in both horizontal directions.

2.5. Merging Data. For merging the individual icing forecasts, different approaches were tested. Besides the classical method to calculate the mean of the three forecasts, the combination of the maximum and minimum was calculated. Additionally, the method proposed by Pepe and Thompson [13] is used. This method combines the forecast values p1,

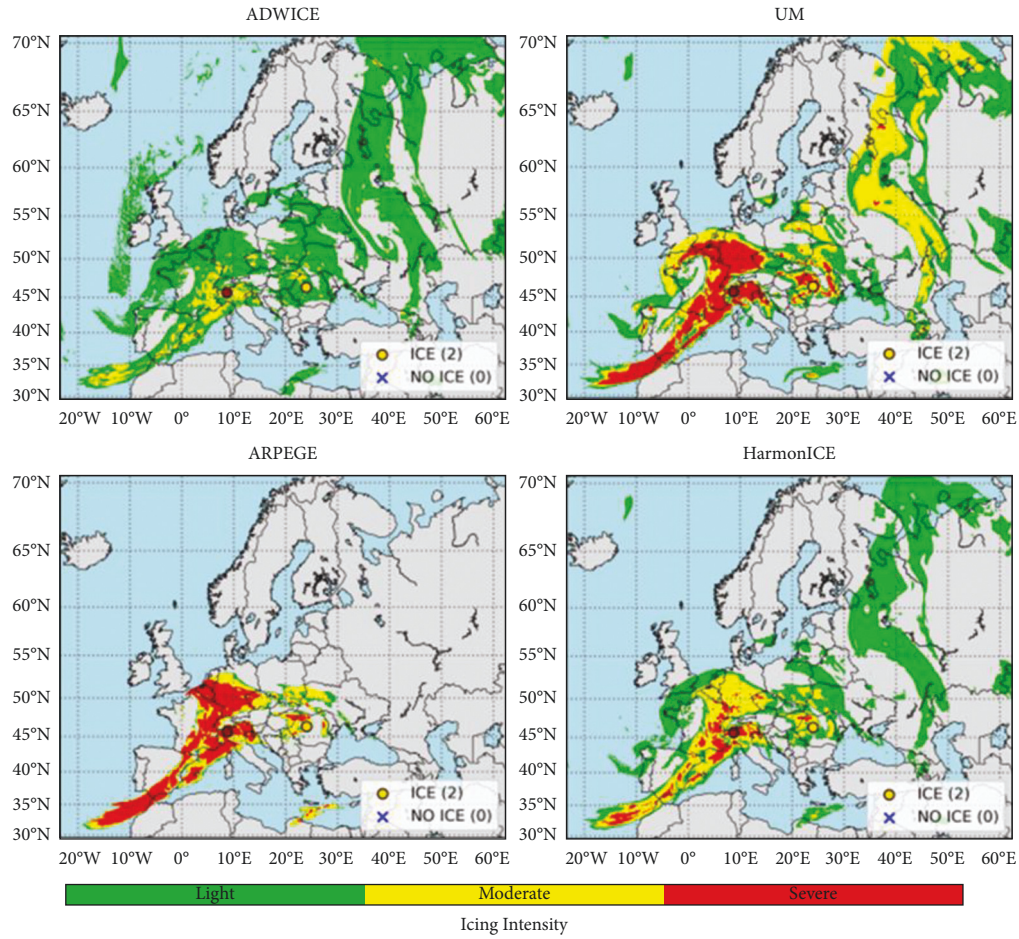

Figure 4: Example of the icing intensity of the three icing forecasts and HarmonICE (mean method applied) for 11 December 2017, 06 UTC, 600 hPa. The corresponding PIREPs from this altitude and point in time are plotted as dots with the same color map as the forecast data.

p2, p3 by choosing a weighting factor $\lambda \in [-1,1]$ in such a way that the combinations $\lambda pi + pj$ (with $i, j \in \{1,2,3\}$) result in an optimal value for the chosen skill score for each pair of possible combinations (pi, pj). The pair with the highest resulting skill score is then combined into a new intermediate combined icing forecast value pij. This process is then repeated for the remaining pair of icing forecasts pk, pij (with $k \in \{1,2,3\}$) in order to calculate a second weighting factor for the final product, which has the following form: $pijk = pi + \lambda 1\ pj + \lambda 2\ pk$.

2.6. Evaluating Data. Former studies often used a binary yes/no icing analyzing method, for example, Brown et al. [14] and Kalinka et al. [5]. A contingency table enables the calculation of POD (probability of detection) for yes and no icing as well as calculation of the FAR (false alarm rate). The AUC (area under the curve) can also be calculated. These skill scores provide an overview of the forecast quality and enable comparisons of different NWP model performance to be made. However, this binary method distinguishes only between an icing and a no icing event with no consideration to the intensity. For this reason and the fact that only a small number of negative icing reports are available (they are needed for the FAR calculation), a more complex multicategory contingency table is used to analyze the data (e.g., Murphy [17], Brooks [18]). A detailed description of the method applied in this study for calculating skill scores from the multicategory contingency tables is given in the next section alongside an example.

3. Results and Discussion

In this section, the results are presented for combining individual in-flight icing forecasts using simple and more sophisticated methods. The skill of each method for combining the individual in-flight icing forecasts as well as of each individual in-flight icing forecast is shown. Based on these results, the recommended approach for combining the in-flight icing forecasts for HarmonICE is presented.

3.1. Example of a Combination of Individual Forecasts. One of the simplest ways of combining the icing forecasts is by calculating the average icing intensity (mean method). An example of such an icing intensity field is shown in Figure 4. A pressure level of 600 hPa on 11 December 2017 at 6 UTC (model run at 00 UTC) is chosen. At this time, the single forecasts show some significant differences in the icing intensities (ADWICE has only very small areas of severe

icing) and in the areas where icing occurs (ARPEGE has no icing in the northeastern and northwestern part of the domain). However, the position and spatial extension of the frontal zone agree well between all models. In the HarmonICE field, the mean method is shown to remove icing areas with light intensities predicted by only one of the three forecast products and typically reduces the higher icing intensity areas since the highest intensity predicted by all products appears only in few areas.

The two PIREPs available at this flight level and time, shown as colored dots in Figure 4, agree well with the forecast icing intensities of HarmonICE. In contrast, not all of the individual forecasts are a good fit to the PIREPs, further highlighting the benefit of intelligently combining the individual in-flight icing forecasts into HarmonICE. Analysis of all data during the winter season for this mean-method case is shown in Figure 5. The multicategory contingency table belongs to the point comparison (smallest model box size around each PIREP) and can be read as follows: on the green diagonal, the forecast values agree perfectly with the observed data. An optimal forecast would generate nonzero values only along this diagonal; all other entries would be zero. The blue cells show under-forecast cases where the predicted icing intensity is smaller than the corresponding PIREP icing intensity. The red cells show the over-forecast cases. The darker the red and blue colors, the larger the differences between the forecast icing intensities and each corresponding PIREP. The percentage of the three categories (perfect forecast, under-forecast, and over-forecast) is mentioned below the table. The gray cells give the sum of the corresponding rows and columns. As mentioned previously, 3010 PIREPs were compared with a forecast value. This is less than the total amount of PIREPs available in the winter season (see section "Data and Methods") since not all forecasts were not available over the entire time period and some PIREPs were reported from an altitude above the model domain height.

In this example of averaging the individual model forecasts, the results show a tendency to underestimate the icing intensities. Nearly half of the compared values of the mean-method data are smaller than the corresponding PIREP. A perfect forecast, where the predicted icing intensity and the corresponding observed icing intensity are identical, is observed in 41.7% of all cases.

The multicategory contingency table provides a variety of different information about the analyzed forecast product. However, it does not provide one single skill score, which would allow an overall evaluation of the product and a simple comparison with multicategory contingency tables derived from other forecast products. In order to create a single skill score to use to compare the individual icing forecasts, the PODs of each icing intensity, as well as the total hit rate, the FARs of each icing intensity as well as the total false-forecast rate and under- and over-forecasting rates were calculated. For the latter four values, the total amount of observed PIREPs (3010) was used as the divisor. To calculate the icing intensity hit rates (no, light, moderate, and severe), the number of correctly forecast icing intensities (green values on the diagonal of the table in Figure 5) was

Observed icing intensities (PIREPs)

Forecast icing intensities	0	1	2	3	all
0	236	42	561	63	902
1	4	29	568	72	673
2	7	60	949	145	1161
3	0	14	219	41	274
all	247	145	2297	321	3010

Blueish cells: underforecast: 1451 ≙ 48.2%
Green cells: Perfect forecast: 1255 ≙ 41.7%
Reddish cell: Overforecast: 304 ≙ 10.1%

Figure 5: Multicategory contingency table for the mean method using point data comparison.

divided by the amount of PIREPs with the corresponding icing intensity (gray values in the last line of the table in Figure 5). For example, the hit rate of no icing was calculated by dividing 236 by 247, which results in 0.96. Figure 6 shows the above-listed skill scores calculated from the multicategory contingency table (Figure 5). The very high hit rate for no icing reports (0.96) highlights the problems mentioned in section "Observation Data" section with PIREPs of no icing. Most of the no icing PIREPs are at altitudes where no icing clouds occur and thus these statistics look very good. The reason for taking both the single hit rates of each icing intensity (hit no, hit light, hit moderate, hit severe) and the total hit rate (hit all) into account is that in the total hit rate, each value has the same influence on the probability, while the single hit rates are differently influenced by one value because their total numbers are different.

In order to determine one single skill score from the values shown in Figure 6, they were merged into three different groups of skill scores: the hit rates for the single icing intensities (hit no, hit light, hit moderate, and hit severe), the total hit rate, which is equal to 1-false all and the under- and over-forecast rates. These three groups of scores contain all relevant information in the multicategory contingency table (Figure 5). By averaging the single scores within the groups and then averaging the three groups, one multicategory average skill score (MCASS) is obtained, which contains all relevant characteristics of the multicategory contingency table. The calculation described above can be mathematically formulated as

$$\mathrm{MCASS} = \frac{\sum_{i=1}^{4} \mathrm{hits}_i}{4} + \mathrm{hits}_{\mathrm{all}} + \left(1 - \frac{(\mathrm{underf.} + \mathrm{overf.})}{2}\right), \quad (1)$$

with the first term representing the average of the single hits, the second term representing all hits, and the third term giving consideration to under- and over-forecast events. The under-forecast and over-forecast values are subtracted from one in order to get a value that is best when it is equal to 1. The authors are aware that there are other scores or combinations of scores that can be derived from the multicategory contingency table such as the Heidke skill score (HSS) [19]. However, the MCASS (equation (1)) provides a good and sufficient indication of the icing forecast skills investigated in this study. This was also manually checked by

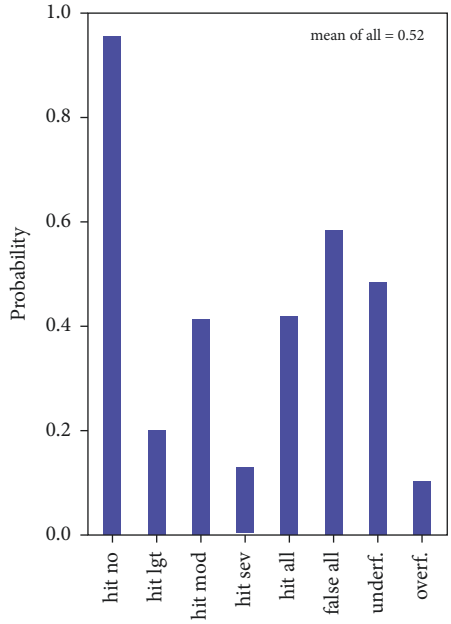

Figure 6: Hit rates of no, light, moderate, and severe icing as well as the total hit rate, false-forecast rate, under-forecasting rate, and over-forecasting rate. Figure 5showsthe bars correspond to the multicategory contingency table.

comparing a set of calculated MCASS with the corresponding multicategory contingency tables.

One additional advantage to the formulation of the MCASS over skill scores such as the HSS is that it can be modified by different weighting factors for each term in equation (1) in order to consider certain single terms more than others. This might be the case if customer requirements are modified in a way that, for example, over-forecasting must have a stronger impact than under-forecasting or the hit rate of severe must be considered stronger than the other hit rates. In the current study, however, the single terms of equation (1) are weighted homogeneously. More detailed analysis of the differences as well as the advantages and disadvantages of the MCASS in comparison with other skill scores will be investigated in future studies.

The MCASS was computed for each individual icing forecast and each individual combination method discussed in the "Merging Data" section (results for the mean method presented in Figures 5 and 6).

3.2. Overview of Various Combination Methods. Following the example for the multicategory contingency table in the previous section, the performance of each individual icing forecast and combination method is now assessed. A final value of MCASS is shown for the recommended combination method for producing HarmonICE.

For the Pepe and Thompson (PT) method, the best values for $\lambda 1$ and $\lambda 2$ were iteratively calculated as 0.6 and -0.2, respectively. The final optimized combination results in ADWICE + $\lambda 1$UM + $\lambda 2$ARPEGE. In Figure 7, all results are summarized for the three forecast products as well as for the four combinations (min, mean, max, and PT). The box sizes used around the PIREPs are indicated as different colors of the bars. Figure 7 shows that when considering the individual forecasts, the box size only has a significant influence on ADWICE. The larger the box size, the better the results indicated by the MCASS. This can be explained by the relatively high grid resolution of ADWICE compared to the other two forecasts. The higher grid resolution leads to higher spatial fluctuations of the icing intensity within small areas, and hence, larger icing intensity values are more likely to be encountered by increasing the box size. Furthermore, ADWICE tends to underestimate the icing intensity more than the other models for the smallest box size (not directly shown here but reflected by the relatively small blue bar of ADWICE in Figure 7), which also leads to better results for an increasing box size. The box size dependency of ADWICE can also be seen in the combined PT method since ADWICE is included with the largest factor of one. Overall, the PT method leads to the best results of all forecast combinations and is better than each individual forecast product. This statement is independent of the box size around the PIREPs. For each box size (bar color), the PT method provides the largest MCASS value.

In order to give a better insight into the improvement of HarmonICE provided by the PT method, Figure 8 shows the multicategory contingency table, which belongs to the largest bar in Figure 7 box 3v7h of PT method red bar). The table in Figure 8 can be compared with that of Figure 5, which was obtained by using the mean method with the smallest box size (box 1v1h of the mean method in Figure 7—blue bar).

The MCASS difference between these two examples is approximately 0.12. This is less than the difference between the PT method and most of the individual forecasts. The perfect forecast using the PT method is 63.1%, more than 20 percentage points larger than with the mean method (41.3%,

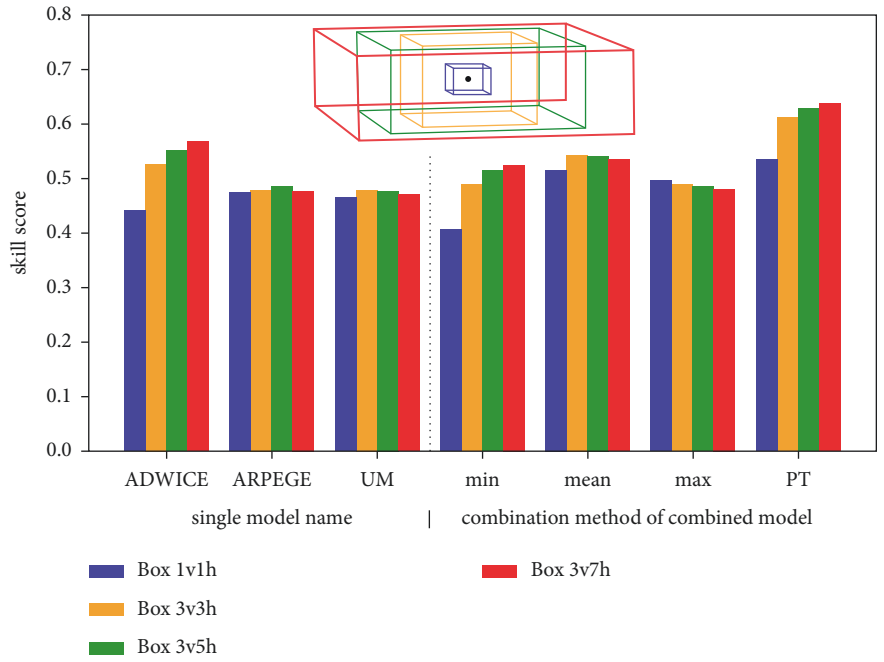

Figure 7: Multicategory average skill score (MCASS) comparison of the three individual forecast products with the four combination methods. The colors mark the box sizes used around the PIREPs to extract the forecast value and are shown schematically on top of the figure.

Observed icing intensities (PIREPs)

Forecast icing intensities	0	1	2	3	all
0	234	14	204	22	474
1	4	26	366	42	438
2	9	101	1625	243	1978
3	0	4	102	14	120
all	247	145	2297	321	3010

Blueish cells: underforecast: 891 ≙ 29.6%
Green cells: Perfect forecast: 1899 ≙ 63.1%
Reddish cell: Overforecast: 220 ≙ 7.3%

Figure 8: Multicategory contingency table for the final HarmonICE forecast, created using the PT method, using a box size of 3v7h (see Figure 7).

see Figure 5), and the under-forecasting is reduced to 29.6%. The main reason for the higher skill using the PT method is that a large number of the light icing forecasts in the other methods are increased to moderate icing. This leads to a high hit rate of moderate icing, which is the group with the most icing reports and consequently has a large impact on the results. Despite this increase, the hit rate of the no icing events is still very good with the PT method (234 vs. 236 with the mean method). This shows that the influence on the hit rate of no icing reports is small.

4. Conclusion and Outlook

In this study, a method for harmonizing in-flight icing forecasts over Europe is introduced. Different approaches were tested in order to find the best combination of three in-flight icing forecast indices based on three different NWP models. PIREPs are used as verification data, although they have some disadvantages for this purpose. An example on a single day shows the differences in the individual forecast products and the combined forecast product using the mean method. The PIREPs reported during the single day event fit reasonably well to the combined data set.

In order to be able to compare the different combination methods, the MCASS was derived from each multicategory contingency table generated for various forecast combinations and the individual forecast products. The MCASS contains all relevant information given by the multicategory contingency table, that is, the hit rates of the four icing intensities, over- and under-forecasting, and the total hit rate. It allows quantitative comparisons of the forecast skill from each icing forecast product as well as from the combination methods presented.

The final comparison of the MCASS of the different forecast combinations and the individual forecast products shows that the PT method provides the best results including showing an improvement compared to each single icing intensity forecast. The sensitivity study of box sizes around the PIREP positions in which the forecast data were extracted shows that the results are independent of the chosen box size; however, it does have an influence on the MCASS. In most cases, an increased box size leads to a larger MCASS, but for certain forecast products or combinations, the results were unaffected by box size or showed a decrease in MCASS.

Within the SESAR Deployment project, initial tests of the preoperational version of HarmonICE have run since the middle of 2019. Since 2020, the data have been provided as a six-hourly icing forecast over Europe. Verification to inform the revision of the best forecast combination method—and if

necessary, a new calculation of the weighting factors—is and will be performed annually with the PIREPs from the previous winter season. Within that recalculation, it will also be possible to adapt MCASS to user requests. The calculation method allows for a different weighting of the single skill score terms such as over-forecasting or a certain intensity hit rate (e.g., severe icing intensity). If one of these single skill score terms must be considered more strongly than the others, it can be implemented in the average skill score calculation.

PIREPs are used for icing verification since better alternatives have previously been unavailable. One alternative for determining observed icing intensities, or at least whether icing occurs or not, is the use of a satellite inferred icing potential [20]. Stretton et al. [21] showed that satellite data can be used to detect the "no icing" regions in cloud-free areas. Furthermore, cloud top heights and the corresponding icing potential at this height level can be derived from the satellite. Overall, satellite data cannot provide a three-dimensional dataset of icing intensities, but it can help to improve the forecast of the areas of icing conditions and accuracy of the verification dataset together with PIREPs. The use of satellite data as a verification tool alongside PIREPs will be explored in future work.

Data Availability

The underlying data have been produced for aviation purposes. They can be provided for aviation use and for research activities. Contact the author or VL.Kundenservice@dwd.de.

Disclosure

The contents of this publication are the sole responsibility of Deutscher Wetterdienst, Météo-France, and Met Office and do not necessarily reflect the opinion of the European Union. An interim status of the study was presented at the "International Conference On Icing Of Aircraft Engines and Structures JUNE 17–21 2019 MINNEAPOLIS MN."

Conflicts of Interest

The authors declare that there are no conflicts of interest regarding the publication of this article.

Acknowledgments

The authors thank all who have provided support and contributed to the European Harmonization In-flight Icing project, especially the project managers of the involved partners Stephanie Jameson (MO), Lauren Donohue (EUMETNET), and Stéphanie Wigniolle (MF), and acknowledge the support from user's perspective by Rosalind Lapsley (EUROCONTROL). The activity as part of the Action "SESAR Deployment Programme implementation 2015–Cluster 2" N° 2015-EU-TM-0196-M is co-founded by the European Union (482k EUR).

References

[1] Eurocontrol, https://www.eurocontrol.int/news/new-traffic-record-set-37228-flights-one-day, 2019.
[2] "SESAR Joint Undertaking," 2021, https://www.sesarju.eu.
[3] "SESAR Deployment Manager," 2021, https://www.sesardeploymentmanager.eu.
[4] M. K. Politovich, "Aircraft icing caused by large supercooled droplets," *Journal of Applied Meteorology*, vol. 28, no. 9, pp. 856–868, 1989.
[5] F. Kalinka, K. Roloff, J. Tendel, and T. Hauf, "The In-flight icing warning system ADWICE for European airspace – current structure, recent improvements and verification results," *Meteorologische Zeitschrift*, vol. 26, no. 4, pp. 441–455, 2017.
[6] W. R. Sand, W. A. Cooper, M. K. Politovich, and D. L. Veal, "Icing conditions encountered by a research aircraft," *Journal of Climate and Applied Meteorology*, vol. 23, no. 10, pp. 1427–1440, 1984.
[7] M. K. Politovich, "Response of a research aircraft to icing and evaluation of severity indices," *Journal of Aircraft*, vol. 33, no. 2, pp. 291–297, 1996.
[8] S. D. Green, "A study of U.S. Inflight icing accidents, 1978 to 2002," in *Proceedings of the 44th AIAA AerospaceSciences Meeting and Exhibit*, Reno, Nevada, 2006.
[9] B. C. Bernstein, F. McDonough, M. K. Politovich et al., "Current icing potential: algorithm description and comparison with aircraft observations," *Journal of Applied Meteorology*, vol. 44, no. 7, pp. 969–986, 2005.
[10] G. Zängl, D. Reinert, P. Ripodas, and M. Baldauf, ""The ICON (ICOsahedral Non-hydrostatic) modelling framework of DWD and MPI-M: description of the non-hydrostatic dynamical core," *Quarterly Journal of the Royal Meteorological Society*, vol. 141, no. 687, pp. 563–579, 2015.
[11] J. Pailleux, J.-F. Geleyn, M. Hamrud, and P. Courtier, "Twenty-five years of IFS/ARPEGE," *ECMWF Newsletter*, vol. 141, pp. 22–30, 2014.
[12] D. Walters, I. Boutle, M. Brooks et al., "The Met Office unified model global atmosphere 6.0/6.1 and JULES global land 6.0/6.1 configurations," *Geoscientific Model Development*, vol. 10, no. 4, pp. 1487–1520, 2017.
[13] M. S. Pepe and M. L. Thompson, "Combining diagnostic test results to increase accuracy," *Biostatistics*, vol. 1, no. 2, pp. 123–140, 2000.
[14] B. G. Brown, G. Thompson, R. T. Bruintjes, R. Bullock, and T. Kane, "Intercomparison of in-flight icing algorithms. Part II: statistical verification results," *Weather and Forecasting*, vol. 12, no. 4, pp. 890–914, 1997.
[15] A. Tafferner, T. Hauf, C. Leifeld, T. Hafner, H. Leykauf, and U. Voigt, "ADWICE: advanced diagnosis and warning system for aircraft icing environments," *Weather and Forecasting*, vol. 18, no. 2, pp. 184–203, 2003.
[16] ICAO, *Annex 3 to the Convention on International Civil Aviation, Meteorological Service for International Air Navigation*, Montreal, Canada, 20th edition, 2018.
[17] A. H. Murphy and R. L. Winkler, "A general framework for forecast verification," *Monthly Weather Review*, vol. 115, no. 7, pp. 1330–1338, 1987.
[18] H. E. Brooks and C. A. Doswell III, "A comparison of measures-oriented and distributions-oriented approaches to forecast verification," *Weather and Forecasting*, vol. 11, no. 3, pp. 288–303, 1996.

[19] P. Heidke, "Berechnung des Erfolges und der Güte der Windstärkevorhersagen im Sturmwarnungsdienst," *Geografiska Annaler*, vol. 8, pp. 301–349, 1926.
[20] P. N. Francis, "Detection of aircraft icing conditions over Europe using SEVIRI data," *AMS/EUMETSAT Meteorological Satellite Conference Session*, vol. 3, pp. 24–28, 2007.
[21] R. Stretton, P. Buchanan, and P. Francis, *Verification of Met Office Global Icing Potential Forecasts Using Satellite Observations," AMS 18th Conference on Aviation, Range, and Aerospace Meteorology*, pp. 23–26, Seattle, Washington, 2017.

Hindawi
Advances in Meteorology
Volume 2022, Article ID 5356563, 15 pages
https://doi.org/10.1155/2022/5356563

Research Article

Analysis of the Most Common Aviation Weather Hazard and Its Key Mechanisms over the Yangon Flight Information Region

K. T. Oo [1,2] and K. L. Oo [3]

[1]*Aviation Weather Services, Myanmar Air Force, Yangon, Myanmar*
[2]*Nanjing University of Information Science and Technology, Nanjing, China*
[3]*Department of Meteorology and Hydrology, Nay Pyi Taw, Myanmar*

Correspondence should be addressed to K. T. Oo; kyawthanoo34@outlook.com

Received 27 December 2021; Revised 21 February 2022; Accepted 23 March 2022; Published 15 April 2022

Academic Editor: Feng Chen

The aviation industry has a global economic impact of $2.7 trillion (including direct, indirect, induced, and tourism catalytic effects) and contributes 3.6 percent of global GDP. Weather is one of the most essential elements impacting how an aircraft runs and how safely it can fly. The correlation coefficient is the most significant index explaining the relationship between variables and can result in teleconnection patterns of climate indices. El Nino-Southern Oscillation (ENSO) and India Ocean Dipole (IOD) were used in this study based on the ERA5 reanalysis dataset for 30 years (1991–2020). Myanmar's Yangon International Airport has recorded more than 119874 times of observation data from 2009 to 2019. The mean percentage of occurrences of weather elements is calculated for each month and each season. Analysis of flight delay and accident data was obtained statistically from the Aviation Safety Network (ASN). According to the monthly delay index, July, August, and March are the maximum delay index months, and the correlation value between aircraft movement and delays is maximum in July and August and minimum in January and February. After examining numerous characteristics of Yangon International Airport, we identified which elements had a big impact on operations through vital interviews with operators, the accident case study section, and climatology analysis. As a result, we identified two meteorological occurrences: thunderstorm rain (TSRA) and fog (FG) are of high frequency and TSRA poses a larger risk than FG for aviation operation. The maximum frequency (%) of thunderstorm occurrences was 22% in July and the minimum was 1% in January. Annual frequency analysis revealed that TSRA days are becoming more common year after year as a result of global climate change. According to a spatial gridded analysis by ERA5 reanalysis data (1991–2020), the annual convective available potential energy (CAPE) values over local airport regions, the Bay of Bengal (BOB), the western equatorial Pacific, and the South China Sea show a positive correlation with convective rainfall. In contrast, negative convective inhibition (CIN) anomalies have been observed over the same areas as above, except for the western part of BOB along the Indian Coast. The primary innovation is that we look at the effects of thunderstorms on airport operations before determining their link with ENSO and the IOD individually and then combining them during their full phases. This raises a new question and a new possibility for viewing climatology from a new perspective.

1. Introduction

The aviation industry is critical to the economies of developed countries such as China, landlocked countries such as Laos, and small island nation states such as Madagascar. The aviation industry is a vital component of long-term economic development. It also acts as a significant driver of other economic activities like internal trade, military operations, and tourism.

According to the Air Transport Action Group, the aviation industry generated 704.4 billion dollars in direct gross benefits in 2019 and supported 65.5 million jobs worldwide (Figure 1). Aviation has a $2.7 trillion global economic impact (including direct, indirect, induced, and tourism catalytic effects) and contributes 3.6 percent of global GDP in 2019 [2].

The Republic of the Union of Myanmar (also known as Burma) is one of the world's most densely populated

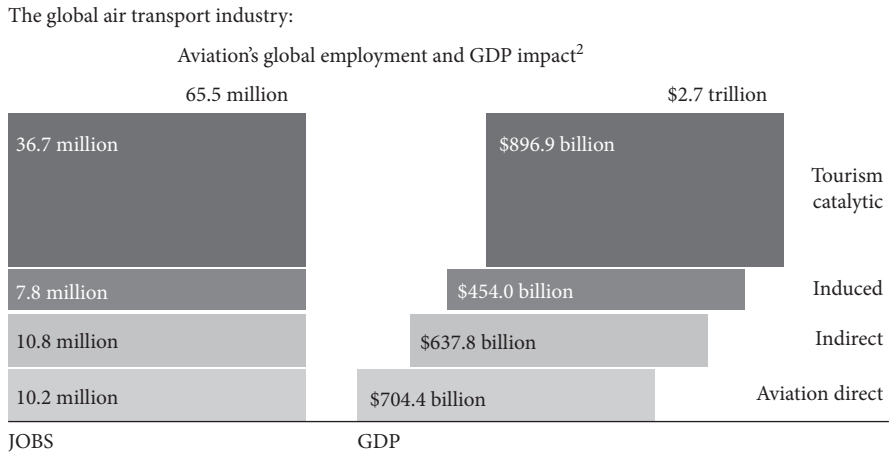

Figure 1: Aviation global employment and GDP impact (2019) [1].

countries. It is bordered on the north-east by the People's Republic of China, the east by Laos, the southeast by Thailand, and the south by India [3]. The busiest airport in Myanmar is Yangon (RGN)/Yangon International Airport (VYYY), with flights to 56 destinations in 14 countries and catering to about six million passengers [4]. Yangon International Airport is the main airport in Myanmar (formerly known as Burma). It has one runway with two touchdown zones (TDZ) and an elevation of 33.6 M (110 FT) above sea level. The airport is home to all ten Myanmar airlines as well as roughly 30 international airlines [5].

The weather is one of the most critical factors influencing how an aircraft runs and how safely it can operate. Weather is also important for the aviation industry benefits, but, unfortunately, it is an uncontrollable factor, as everyone knows. Annual analysis of flight delay causes shows that weather accounts for 6% of total aircraft operation delays (Figure 2) [6].

Aviation and meteorology have a long and illustrious history. Climatology can anticipate significant changes in local weather as well as severe weather patterns. Heavy rain, thunderstorms, hailstorms, and cyclones are all common, resulting in losses in the aviation industry as well as delayed or cancelled flights [7]. As a result, unless new solutions are found, the impact of weather on aviation is likely to increase over time. It is impossible to avoid delays in flying all of the time. Changing climatic and meteorological conditions at the same time have a significant impact on aircraft performance at the airport, which cannot be prevented in the end. These delays are sometimes necessary to demonstrate that the safety of our passengers is our first priority. As of Figure 2, the weather is the only uncontrollable factor among the five forms of aviation delays. As a result, departure delays caused by bad weather are virtually always unavoidable. It is critical to be prepared for departure delays in order for airfield operations to run properly; thus preparedness is necessary [8].

Even in bad weather on an aerodrome, air weather services do not have the authority or ability to close an airport [9]. Airport operators are the only authorities able to close an airport, and this would only be taken in extreme circumstances. The degree to which an aircraft's departure and arrival are visible (or RVR) is determined by the sophistication of ground equipment and the qualification of the flight crew [5]. At or near an airport, low cloud, fog, and rain can make visibility difficult, while thunderstorms and lightning can cause substantial delays in flight schedules. Thunderstorm rain (TSRA) and the fast rising or lowering air currents that frequently accompany it can make flying uncomfortable for passengers and difficult for pilots. Aircraft are unable to take off or land during a TSRA and are usually rerouted around storm cells or diverted from their original locations. Thunderstorms and lightning strikes near airports may cause ground operations to be halted until the storm passes. As a result, data on the spatial and temporal distribution and fluctuations of thunderstorm occurrence and convective rainfall is critical not only for understanding basic climate dynamics but also for societal uses such as airport operations and aircraft operations.

The primary research focus is Yangon International Airport (VYYY), and this work is the first to investigate the impact of aviation climatology over Yangon International Airport (Figure 3). Statistical analysis of the observation data is obtained by the meteorological station. The purpose of the studies has looked at the individual effects of thunderstorms on regions, the El Nino-Southern Oscillation (ENSO), or the Indian Ocean Dipole (IOD) on regional convective rainfall, with only a few taking into account the combined effects of all three on airport operations. Furthermore, the majority of past studies on the association between ENSO/the IOD and precipitation focused on just one or two seasons rather than the full ENSO/IOD cycle. We elaborate on this previous research in this paper by looking at the prospective effects of the ENSO and IOD phenomena, as well as their combined effects, on the annual and seasonal variance of thunderstorm or convective rainfall throughout their phases. Other aviation weather elements may have a significant impact on airport operations. However, in this study, we will just look at these two phenomena. The main difference is that we examine the effects of thunderstorms on airport operations before evaluating their relationship with ENSO and the IOD separately and then integrating them during their complete phases. It is

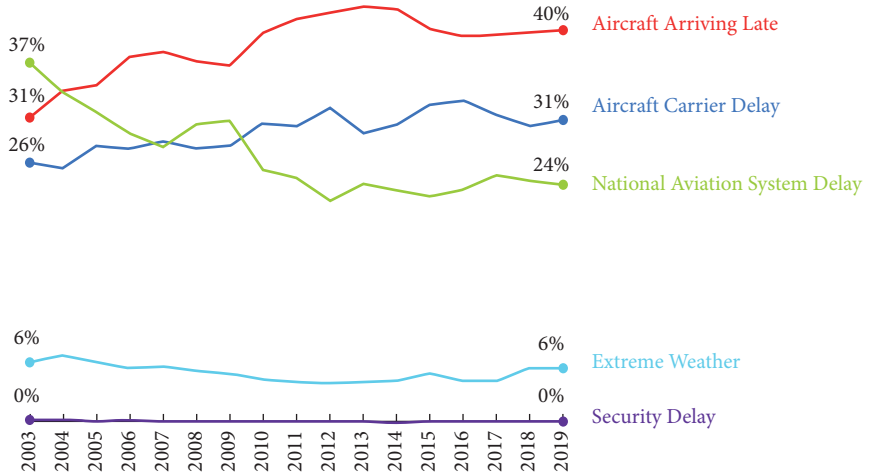

Figure 2: Delay cause by year, as a percent of total delay minutes.

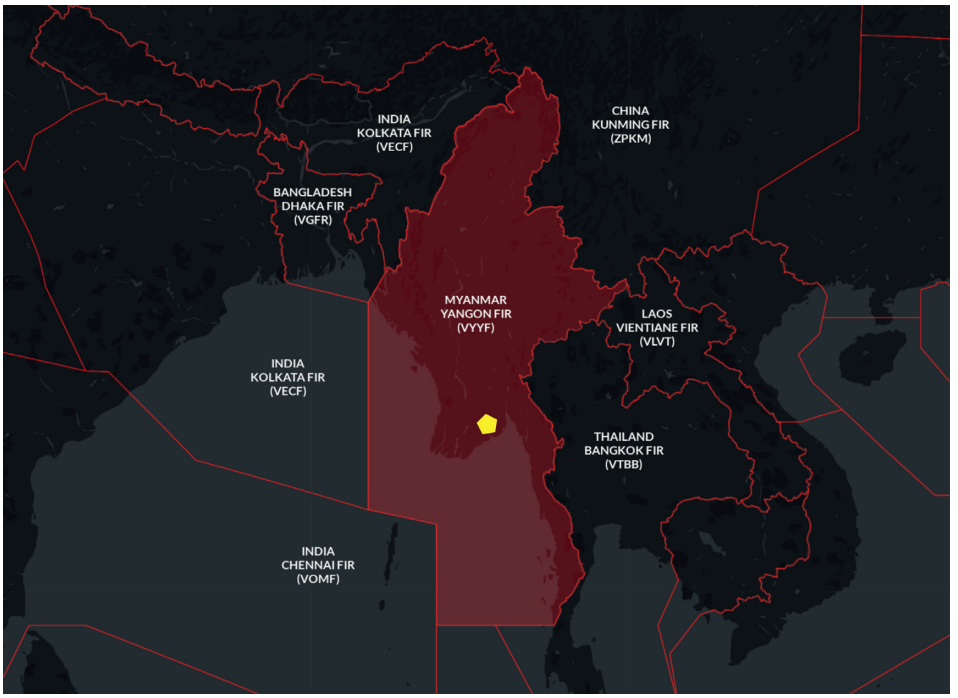

Figure 3: Study area. The red box shows the Flight Information Region (FIR) coverage area of Yangon International Airport Control (Yellow Polygon) [11].

also intended not only for airport operations but also for a diverse group of users, including international and domestic civil airlines flying to and from Myanmar airports, private pilots, airport operational and administrative services, aeronautical administration, air navigation service providers, and the Myanmar Civil Aviation Agency. Besides the potential users mentioned above, this summary can also be used by specialists from other domains for scientific research.

2. Materials and Methods

The International Civil Aviation Organization (ICAO) and the World Meteorological Organization (WMO) have issued recommendations for the processing of climatologic data, which are followed in the creation of statistical data [12]. Count 119874 times of observation data (thirty-minute (xx20, and xx50) METARs) from Yangon International Airport between 2009 and 2019.

Flight delay and accident data are obtained from the Aviation Safety Network (ASN) and the ICAO Safety API Data Service. The aerodrome's data is supported by YIA Service Company Limited and MC-Jalux Airport Services Company Limited. The depicted observation data from the meteorological stations at Yangon Airport meets all the established requirements: the data is representative, continuous, and reliable. The Meteorological Service holds a Quality Management ISO 9001 : 2015 Certificate, which was issued by the SGS international organization.

The large-scale atmospheric parameters such as sea surface temperature (SST) and two-component wind (1991 to 2020) data are taken from the ERA5 reanalysis dataset produced by the European Centre for Medium-Range Weather Forecasts (ECMWF). Also, atmospheric stability indices like Convective Available Potential Energy (CAPE), Convective Inhibition (CIN), K-Index (K), and Total Totals Index (TT) data are taken from the same ERA5 reanalysis (0.25×0.25) resolution dataset of ECMWF for 30 years (1991–2020).

Frequency is a measure of the number of occurrences of a particular score in a given set of data [13]. The climatology is the examination for each month and each season to determine the mean proportion of occurrences of meteorological factors at the study area. The percentage is obtained by dividing the frequency of the category by the total number of participants and multiplying by 100% [14].

$$\text{Frequency Percentage} = \frac{\text{Frequencies of element}^{*}}{\text{Total of Observation Times}}. \quad (1)$$

To improve the climatology results, we performed the vital and online qualitative survey questionnaire about weather experiences for aviation people, resulting in the worst weather phenomena for flight operations at VYYY and a case study of weather-related aircraft accidents at that airport. 15 senior pilots from three airlines (Myanmar International Airline, Air Than Lwin Airline, and Air KBZ Airline) are interviewed.

There are several statistical relationships for perceiving the relationships between two variables which are expressed in both linear and nonlinear equations. The correlation coefficient, which displays the intensity and type (direct or reverse) of the association, is the most important statistic for explaining the relationship between variables. This coefficient's computed value ranges from −1 to +1. Based on the average values, we carried on and performed a correlation coefficient for deep analysis. Before performing composite and correlation analyses, all climatic parameters' data were detrended. Generally, the most common index for showing the correlation is Pearson's correlation coefficient. This index shows the degree and direction of correlation. The Pearson correlation coefficient (r) is calculated using the following equation:

$$r = \frac{n(\sum xy) - (\sum X)(\sum y)}{\sqrt{\left[n\sum x^2 - (\sum x)^2\right]\left[n\sum y^2 - (\sum y)^2\right]}}. \quad (2)$$

Teleconnection patterns can be the result of correlation analysis, as with other techniques. This method has been widely used in climate research, and each offers some advantages [15]. The global climate indices El Nino-Southern Oscillation (ENSO) and Indian Ocean Dipole (IOD) were used in this study and were studied from the same ERA5 SST. The average SST anomaly in the region of 5N to 5S and 170W to 120W (NINO3.4 region) index is a largely used indicator of ENSO. Similarly, the Indian Ocean Dipole (IOD) is the difference between two SSTs in the equatorial Indian Ocean's western (50E–70 E and 10S–10 N) and eastern (90E–110 E and 10S–10 N) halves [16]. Our study also analyzed annual and seasonal correlations of gridded data for SST, convective rainfall over Yangon Region, and CAPE index based on the ERA-5 dataset to calculate TSRA occurrence indices using IBM SPSS, CDO, and open-grads. Student's t-test with a 95 percent confidence interval was used to establish the statistical significance of the composite analysis in this study. The application of this technique to South Asian countries has been presented in a previous number of works [7–9]. The Pearson correlation analysis is used in this study to show the association between the variables with a 95% confidence level.

3. Results and Discussion

3.1. Flight Delay Causes. It is critical to investigate airplane delays and their causes in order to preserve airspace efficiency and safety [21]. Delay samples, on the other hand, are not independent because they consistently display the same aggregation pattern. These delays take one of three forms: ground delay programs, ground stops, or general airport delays. A ground delay program may be instituted when the arrival demand at an airport is greater than the determined capacity of the airport [21]. These programs limit the number of aircraft that can land at an affected airport. Because demand is greater than the aircraft's arrival capacity, flight delays will result [22]. Second, when severe weather is forecast for a short period or the weather at the airport is unsuitable for landing, ground stops are issued. Ground stops mean that traffic bound for the impacted airport is prohibited from leaving for a set amount of time. Finally, there are general delays in arrival and departure. This usually means that arriving traffic is encountering airborne delays or that outgoing traffic is suffering longer than usual cab wait times or gate delays. This could be caused by a variety of factors, including nearby thunderstorms, heavy departure demand, or a runway modification. Total flight delay categories at VYYY during 2019–2021 are shown in Figure 4.

As the delay index, compiled by Airports INFO Statistics, shows that the relationship between aircraft delays and adverse weather is primarily relative at Yangon International Airport (Figure 5). Weather delays can occur in both direct and indirect ways. If airport weather is bad, that can be a direct impact, and bad weather situations on the route of the aircraft can be an indirect impact, as a flight can be arriving late.

After categorizing the delay causes, we found that the weather-related delay index is high. The delay index represents the percentage of delayed flights (take-offs) [23]. For example, if there are 10 flights on a day and 5 are delayed, then the delay index would be 50%.

By the monthly delay index, we found July, August, and March are the maximum delay index months, and May is the minimum month within 2019–2021 (Figure 5). As the above delay index with aircraft movement by month, the correlation value is maximum in July and August and minimum in January and February (Figure 6). Aircraft movement means all airport movements for this airport. A movement can be a take-off or a landing, which are summed up.

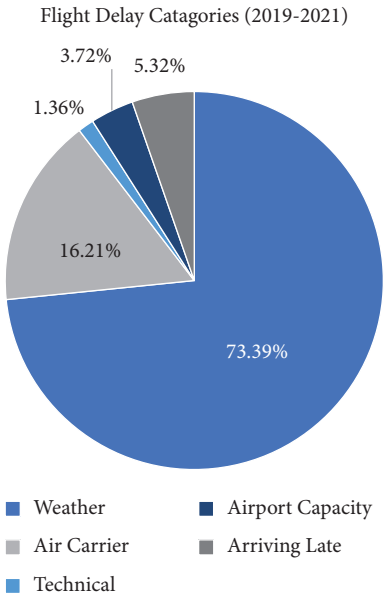

Figure 4: Flight delay categories during 2019–2021.

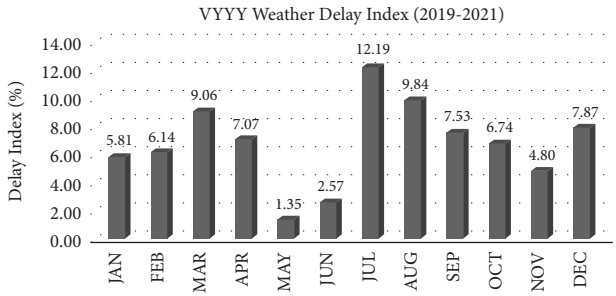

Figure 5: Weather delay index for VYYY (2019–2021).

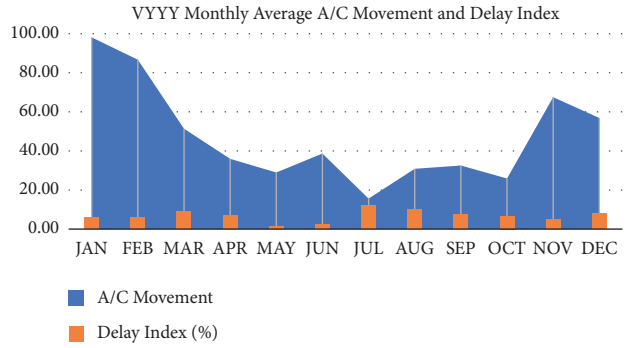

Figure 6: Correlation of monthly aircraft movement and delay index.

Weather conditions can create major delays in air travel [22], resulting in the cancellation or postponement of hundreds or thousands of flights, affecting the itineraries and budgets of millions of people. More than that, bad weather conditions may lead to flight accidents. A comprehensive study was conducted on Yangon International Airport using climatology data and the aircraft delay index to identify the particular meteorological elements that cause flight delays and cancellations by month.

Airport weather directly impacts airport operations, and other aviation hazards also occur based on these weather phenomena. Thus, as a result, we found that, among the 20219 times weather phenomena occurred, including 1237 times of thunderstorms (maximum in July) during this study period. Compared to the flight delay index, July is also the highest delay index during 2019–2021 (Figure 6).

3.2. Qualitative Survey Results and Accident Cases Study. Interviews are conducted with the 15 senior pilots from 3 airlines (Myanmar International Airline, Air Than Lwin Airline, and Air KBZ Airline). The questionnaires included the following questions:

(1) What are the worst weather-related aviation hazards?

(2) What time of day is the best for weather conditions for flying?

(3) How much visibility is important in flight and in which phase of flight?

(4) What is the worst weather phenomenon at Yangon International Airport?

For the survey result of vital or online question No. 1, 52% answered that thunderstorms are the worst weather phenomenon for flight operations, and 10% answered that fog conditions are the worst also. Other weather phenomena were mentioned by 38% of those polled, but the majority of them were thunderstorm-related (Figure 7(a)). Thus, we can assume that thunderstorms and fog are the worst weather phenomena for flight operations in Myanmar.

For question No. 2, 55% said that 09:00 am to 12:00 pm local time (01:30 UTC to 05:30 UTC) is the best time to fly (Figure 7(b)). For question No. 3, 87.5% answered that visibility is very important for aircraft approach and landing (Figure 7(c)). As the survey result of question No. 4, 30% answered that thunderstorms are the worst weather phenomenon at Yangon International Airport and 10% answered that fog conditions are the worst also. Another 20% answered that rain on airplanes' approaches is relative to poor visibility, and the other 16% answered that heavy gust wind is the worst weather phenomenon at Yangon International Airport. Other answers are low ceilings with cloudy conditions (Figure 7(d)). However, most of them are thunderstorm-related phenomena. Thus, we can assume that poor visibility, low ceiling, and thunderstorm and fog weather conditions are the worst weather phenomena for Yangon International Airport according to survey results.

3.3. Causes of Aircraft Accidents over Myanmar. It is quite rare for an accident to be explained by one single cause. Almost every catastrophe is the result of a series of circumstances, and most accident reports distinguish between the main cause and multiple contributory elements. Figure 8 shows the distribution of the main causes identified in an aircraft accident. The main root cause is weather-related accidents. Also, some loss of control accidents may be unfortunate factors that can result in aviation accidents.

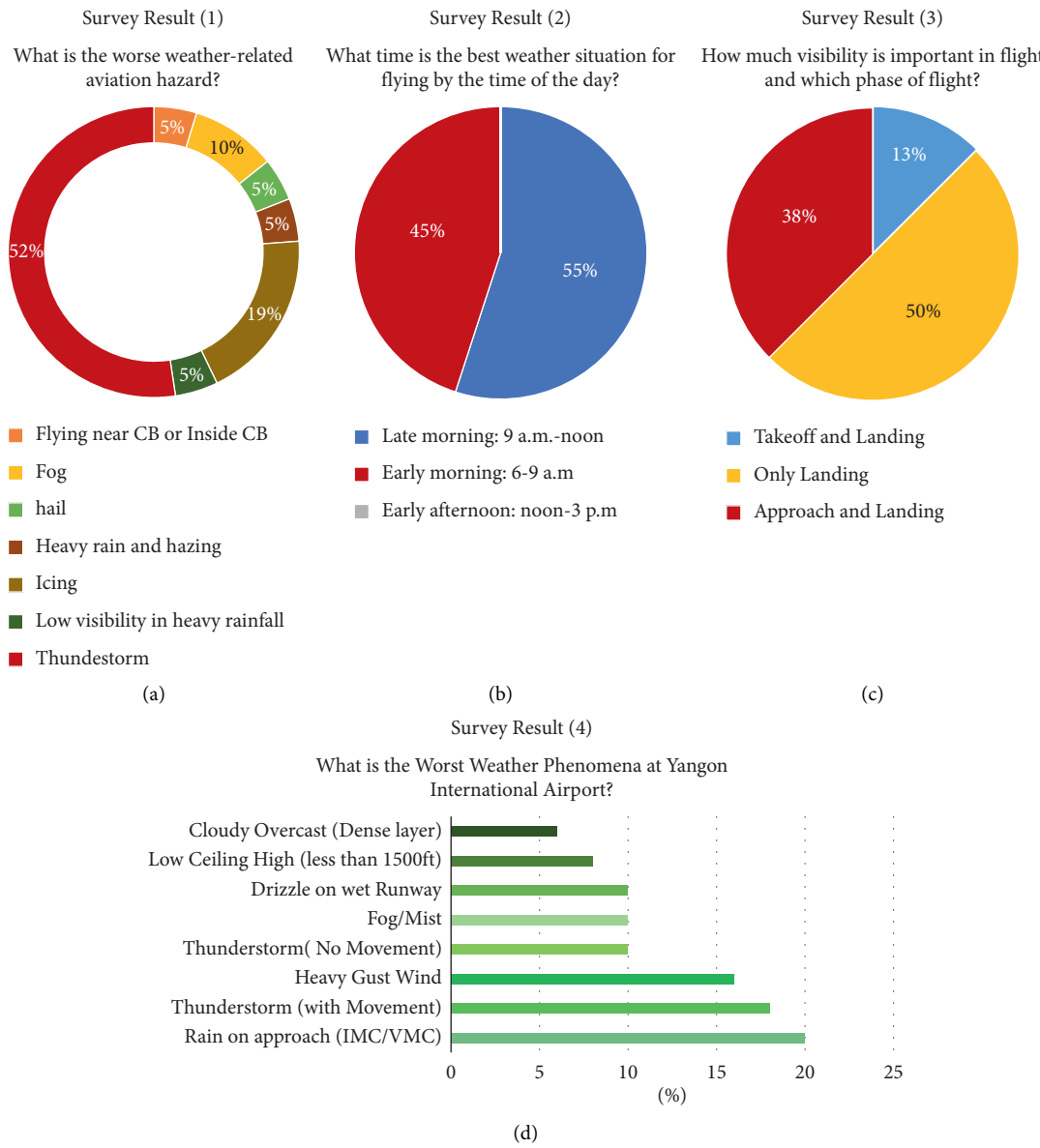

Figure 7: Questionnaires survey results.

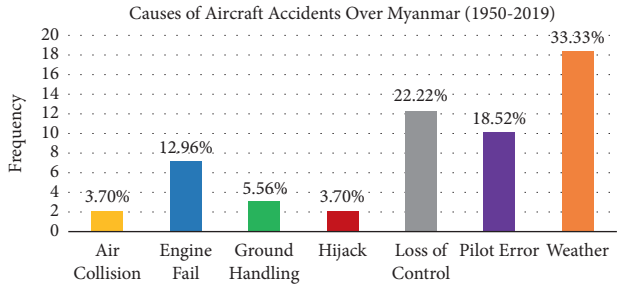

Figure 8: Causes of aircraft accidents over Myanmar (1950–2019).

Among an aircraft's greatest threats are the effects of significant flight icing or in-flight turbulence.

There are a lot of noted weather-related aircraft accidents over VYYY, such as Air Bagan 424 landing crash in 2015 [24], the Shaanxi Y-8-200F transport plane crash near Dawei in 2017 [25], and the Biman Bangladesh Airlines DHC-8-400 accident in 2019 [26]. According to accident reports, these accidents may be caused by the direct or indirect impact of a thunderstorm, and the satellite image analysis results can be seen in Figure 9.

As a result of vital or online questions, most answered that thunderstorms rain (TSRA) and fog (FG) are the worst weather phenomena for flight operations and others answered with other weather phenomena, but most are thunderstorm-related phenomena. For Yangon International Airport (VYYY), many answered that 6:00 am to 12:00 pm local time (23:30 UTC to 05:30 UTC) is the best time for flight operations and that TSRA and FG are the worst weather phenomena for operations. According to the accident case study, most aircraft accidents are found to be thunderstorm-related accidents exhibited in Figure 9 during 2009–2019. From all the above results, we may assume that

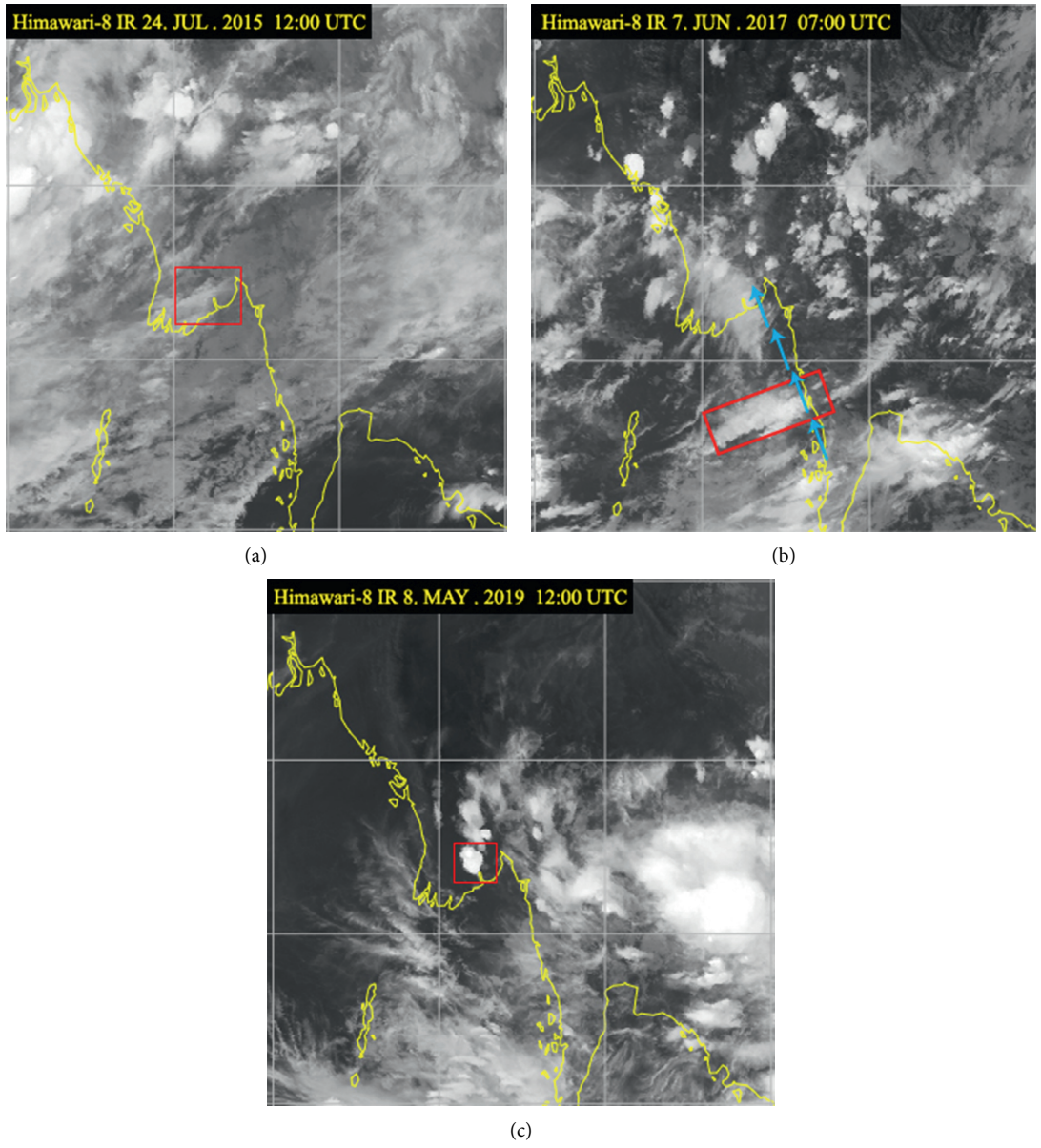

Figure 9: Actual thunderstorm cloud condition satellite image at a time of (a) Air Bagan ATR72, (b) Biman DHC-8-400, and (c) Y-8-200 F W aircraft's accidents.

the worst weather phenomena for flight operations in Myanmar are thunderstorms.

3.4. Thunderstorm Days Analysis. We count 119874 occurrences of observation from Yangon International Airport using half-hourly METAR data. This data contained 20219 instances of meteorological phenomena, including 1237 thunderstorms. The percentage of each weather phenomenon that happens, including thunderstorms, is shown in distinct hues in Figure 10. The maximum frequencies in February are mist (BR) 0.86%, haze (HZ) 8.35%, and fog (FG) 11.55%. Maximum thunderstorm rain (TSRA) of 12.13% occurred in July during 2009–2019 with Drizzle (DZ) of 9.74%, Rain (RA) of 6.49% (Figure 10).

After examining numerous characteristics for Yangon International Airport, we identified which elements had a big impact on operations, and we obtained a lot of practical information from the operators during the important interview phase. The accident case study section also demonstrates how weather, specifically TSRA and visibility, can influence aviation crashes. As a result, we identified two meteorological events (TSRA and fog) that were very likely to cause plane accidents or operational delays. Because it is associated with a range of other weather phenomena such as hail, wind shear, and lightning, TSRA provides a larger risk than fog.

The three seasons in Myanmar are summer or hot weather season (March–mid-May), rainy or southwest monsoon season (mid-May–October), and winter or

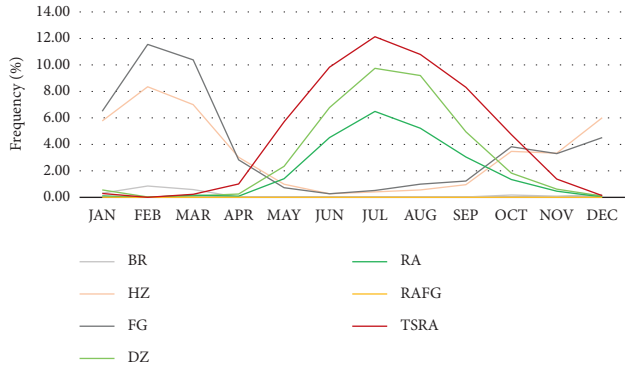

Figure 10: Climatology of monthly frequencies (%) of weather phenomena (2009–2019).

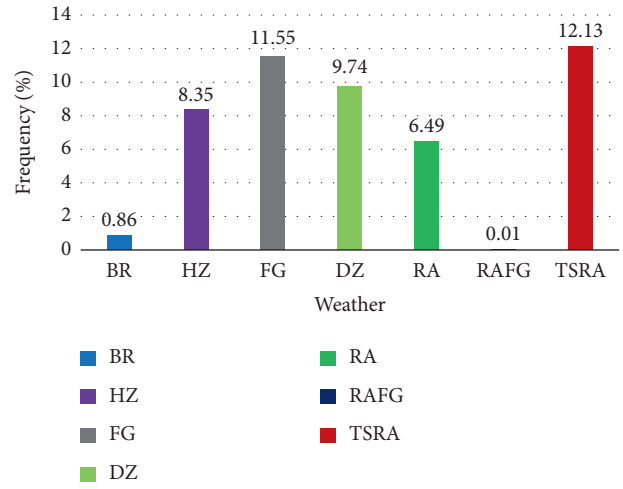

Figure 11: Maximum frequency (%) of weather occurrences by phenomenon (2009–2019).

northeast monsoon season (November–February) as by Myanmar Climate Report 2017 [27]. During the winter, fog and haze weather phenomena are more common. Thunderstorms have been reported not only during the southwest monsoon (wet) seasons but also during the second half of the summer (dry) season, which extends from April to November each year. As the result of Figure 10, maximum thunderstorm conditions have been present for at least 8 months at Yangon International Airport.

Thunderstorms (TS) and fog are the most dangerous weather phenomena at Yangon International Airport (FG) as shown in Figure 11. Thunderstorms had a greater influence on airport operations because of the numerous types of weather that followed, such as hail, strong winds, heavy rain, lightning, and extreme turbulence. All of these factors have a significant impact on aircraft and airfield operations. Thus, the following evaluations of TSRA conditions are carried out in great depth.

From 2009 to 2019, the frequencies (%) of thunderstorm occurrences were analyzed for monthly and daily occurrences are as shown in Figure 12(a). The maximum frequency is 22% in July, the minimum frequency is 1% in January, and there are no occurrences in February, March, and December. According to the seasonal distribution, July is the southwest monsoon season and thunderstorms are typical during this time of year. Tropical cyclones from the Bay of Bengal or the Western Pacific, on the other hand, are the predominant cause of thunderstorms in the winter and summer [27].

For the frequencies (%) for daily analysis of TSRA during this 2009 to 2019 period, the maximum frequency of TSRA may occur from 08:30 to 10:00 UTC during a day (Figure 12(b)). The minimum frequency may occur from 19:00 to 20:00 UTC. According to time zones, 08:30 UTC will be 15:00 afternoon in the local time. Thus, maximum TSRA occurrences may have occurred between 15:00 and 16:30 afternoon on those TSRA days at Yangon International Airport. In such TSRA days, 00:00 UTC to 04:00 UTC is the best time for daytime operations for aviation.

The yearly frequencies research revealed that TSRA days become increasingly common year after year, indicating that global climate change is to blame. In 2010, there were 255 instances, the lowest amount in the previous eleven years. The average number of incidents in 2018 was 527, and it was 920 in 2017 (Figure 13). The trend forecast showed a positively increasing thunderstorm occurrence in the future, and the regression value of this trend is strong ($R^2 > 0.7$) at more than 95% significance level.

3.5. Synoptic Mechanisms Possibly Underlying Thunderstorm Variability. Most of the world's climate change and India's monsoon system is deeply concerned with the Pacific Nino area SST [29]. To result in the teleconnection pattern, we used a correlation between the Nino Index and yearly convective rainfall. Before analysis, we performed the correlation of standardized monthly convective rainfall based on ERA5 and observed stations TSRA occurrence datasets, averaged over longitudes 96°E-97°E and latitudes 16°N-17°N during 2009–2019. The results demonstrate a strong positive connection between both variables with a 95% level of significance (Figure 14). According to the above result, the spatial analysis is carried out using ERA5 reanalysis data, as shown next.

Thunderstorms are caused by the convective downpour, which occurs when the Earth's surface warms rapidly, resulting in an unstable atmosphere. As the heated surface air rises, it cools, resulting in clouds and heavy rain [30]. In meteorology, moisture, instability, and lifting are three components required for a thunderstorm [31]. The convective available potential energy (CAPE) is a measure of thunderstorm potential [32]. CAPE is the total amount of work performed by the upward (positive) buoyancy force on a certain mass of air (called an air-parcel) if it were to climb vertically through the entire atmosphere (often abbreviated as CAPE) [33]. The index is based on measures such as "vertical temperature lapse rate, lower atmosphere moisture content, and the vertical panes of the moist layer," according to the NOAA.

The composite with annual 10 m component wind, the correlation of convective rainfall over VYYY with annual anomalies of CAPE Index, and convective inhibition of the

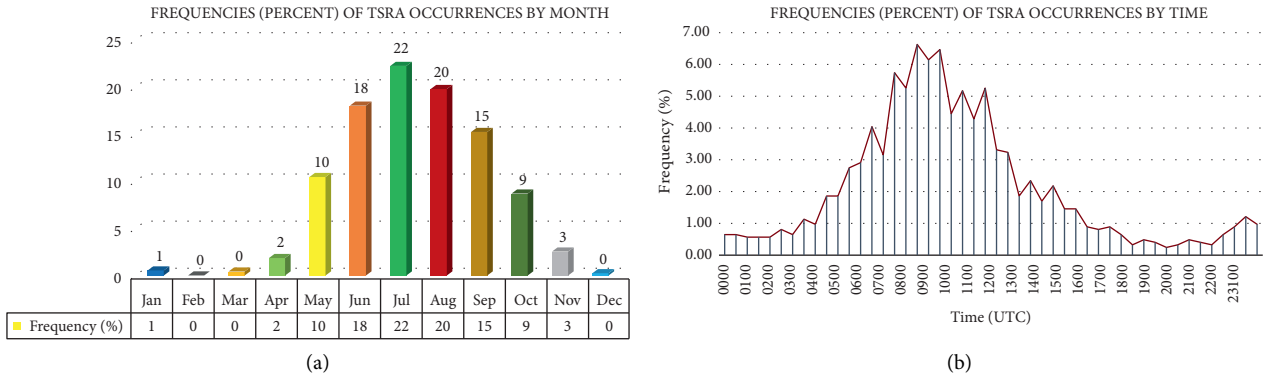

Figure 12: (a) monthly (b) and daily frequencies of TSRA occurrences at Yangon International Airport from 2009 to 2019 [28].

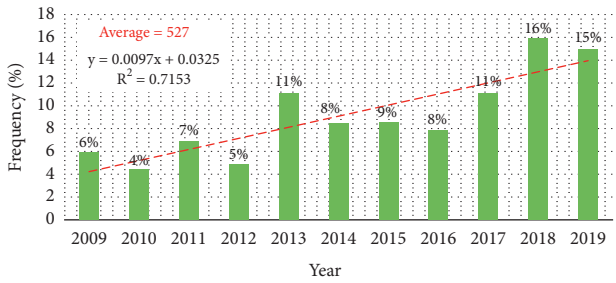

Figure 13: Annual frequencies of TSRA occurrences at VYYY (shaded bar) with their trend (red-dotted line) during 2009–2019.

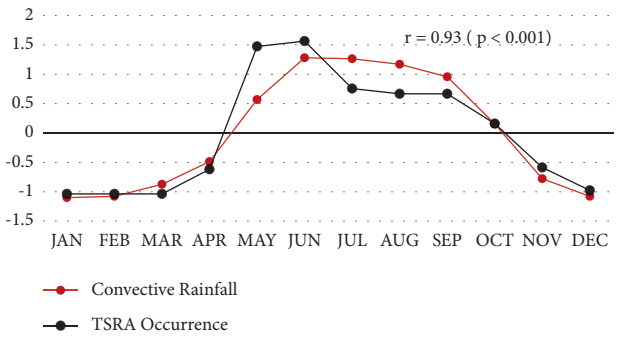

Figure 14: The correlation of standardized monthly convective rainfall based on ERA5 and observed station TSRA occurrence datasets, averaged over longitudes 96°E-97°E and latitudes 16°N-17°N for the period of 2009–2019.

region are exhibited in Figure 15. Convective available potential energy (CAPE) and convective inhibition (CIN) both respond to changes in the heat and humidity profiles of the atmosphere in the absence of moist convection [34]. These changes are explained in terms of a direct effect, which involves changes in the profile in the absence of parcel changes, and an indirect effect, which involves changes in air-parcel evolution in a developing convective boundary layer. A simple estimate of the direct influence on CAPE, which is independent of the assumptions related to choosing parcel ascent, is shown to give accurate results. As a result of Figure 15(a), the annual CAPE over local airport regions, the Bay of Bengal (BOB), the western equatorial Pacific, and the South China Sea shows a strong positive correlation with convective rainfall over the study area. In contrast, negative CIN anomalies have been observed over the same areas as above, except for the western part of BOB along the Indian Coast (Figure 15(b)). It is shown that these areas had a strong chance to experience convective activity. Furthermore, the annual component wind, which blows from the southwest sea to the northeast, may result in increased moisture transport to the BOB's northeast continental area and encourage convective rainfall over the airport regions (Figure 15). These results are agreed with previous studies on the South Asian summer monsoon [35].

Several recent studies have highlighted the ocean's role in climate and weather predictability, as well as the regional patterns of the effects of global teleconnections like IOD and ENSO. The ENSO indicator of atmospheric variability has been thoroughly investigated, and it is thought to serve as an "atmospheric bridge" connecting interannual SST fluctuations in the tropical Pacific with oceanic variations at higher latitudes [36]. The following correlation results show that interannual convective rainfall over the study area does not have any significant correlation with SST at NINO 3-4 (5N–5S and 170W–120 W) in the Pacific Ocean, but a significant negative correlation is found clearly over Indian Ocean (Figure 16(a)). However, seasonal relationship analysis shows different results, with a positive correlation over the Nino 3-4 region. Especially in the summer southwest monsoon season (JJAS) (Figure 16(b)), there was a positive (warming) strong correlation of convective rainfall with SST over the Nino 3-4 area in the equatorial Pacific regions. But there was only a weak positive correlation during the winter months (DJF) (Figure 16(c)).

There is maximum TSRA occurrence also found during the summer months (Figure 12(a)) and convective rainfall also exceeds that in the other months as in Figure 14. It means that Nino 3-4 SST anomalies can strongly impact on thunderstorm occurrence and convective rainfall over the study region during the summer months (JJAS). A weak positive IOD phase can also be found during summer (Figure 16(b)). In contrast, the negative IOD phase can be found in the winter months (DJF) (Figure 16(c)). But only Indian Ocean (IO) SST shows a strong negative correlation with convective rainfall for the annual mode (Figure 16(a)).

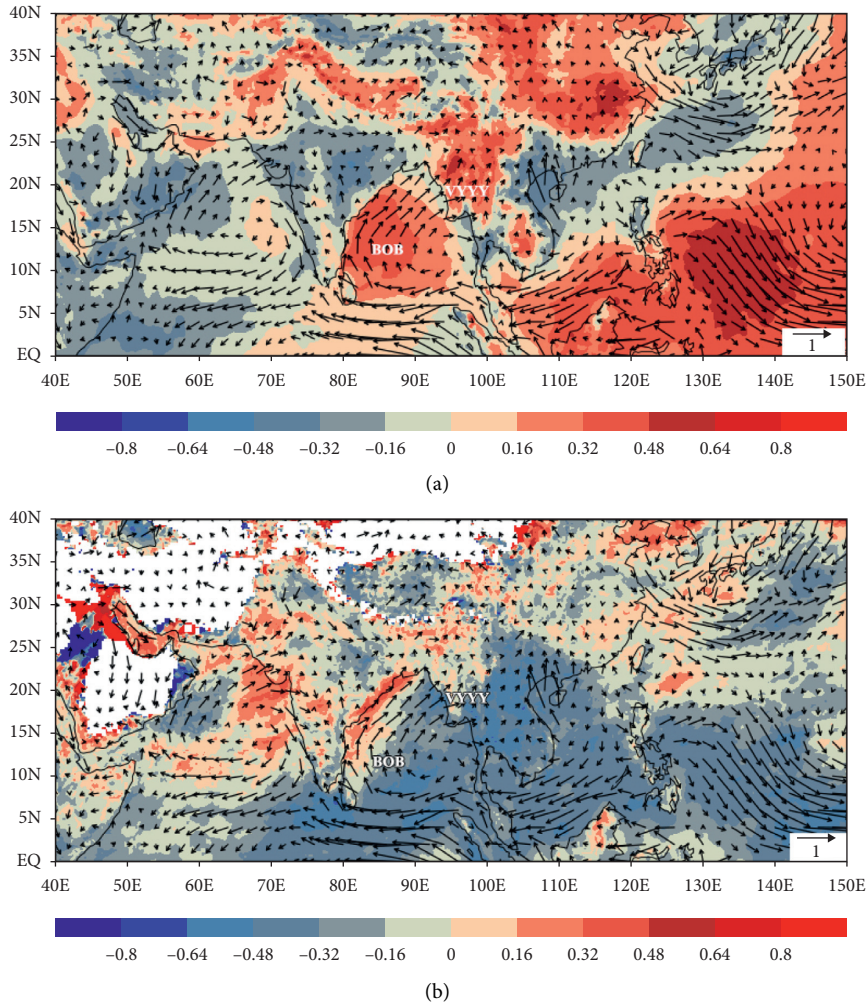

FIGURE 15: The composite of correlation between annual convective rainfall over VYYY and (a) annual anomalies of CAPE Index (J kg^{-1}) of the region and (b) annual anomalies of convective inhibition (J kg^{-1}) of the region (ms^{-1}), with annual 10 m component wind (ms^{-1}).

The main conclusion is that increased convective rainfall may occur during the summer El Nino phase of ENSO (JJAS). Interannual negative Indian Ocean SST anomalies may also result in increased convective rainfall over the study area as the result of Figure 16(a).

The influence of the ENSO signals on precipitation can persist from year to year [37]. Furthermore, the lagged relationship between convective rainfall over the study region, NINO 3-4, IOD, and IO during 1991–2020 was calculated for significant results (Table 1). The robust relationship of convective rainfall is observed with only summer NINO3-4 and winter IOD. Moreover, the concurrent response of NINO3-4 to summer (JJAS) convective rainfall for the study period is 0.50 ($P < 0.01$) (Table 1). A negative correlation value of −0.44 (p–0.02) with IOD is found for the winter months (DJF). But neither NINO 3-4 nor IOD found significant value for annual analysis. Only IO SST has a negative correlation of −0.65 (p 0.01) with convective rainfall over the study region during 1991–2020.

In order to select the anomalous convective rainfall exceed or less years, standardized anomalies at or above ± 1 have been used. (Figure 17). The black line represents the reference line and the black-dotted line separates the exceeding and less years during 1991–2020. The result shows each positive (exceeding: 1994, 1999, 2006, and 2008) and negative (less: 2001, 2010, 2015, 2019, and 2020) anomaly year.

Previous correlations (Figure 16) show only that summer convective rainfall over the study area has a strong positive correlation with SST at NINO 3-4 (5N–5S and 170W–120 W) and a weak positive correlation with the IOD (see Figure 16). To understand the reason for negative and positive anomalies of convective rainfall over the study area, Figure 18 depicts a composite of the correlation between convective rainfall anomalies and SST during exceeding and less years of convective rainfall. The lagged correlation between detrended seasonal convective rainfall and SST for 30 years (1991–2020) is presented in Figure 18 to observe the dependency of summer (JJAS) convective rainfall on large-scale global force.

The lagged years analysis was performed based on Figure 17 to show a more dominant annual and seasonal correlation. The converse pattern was observed during exceeding and less years (Figures 18(a)–18(d)) of annual and

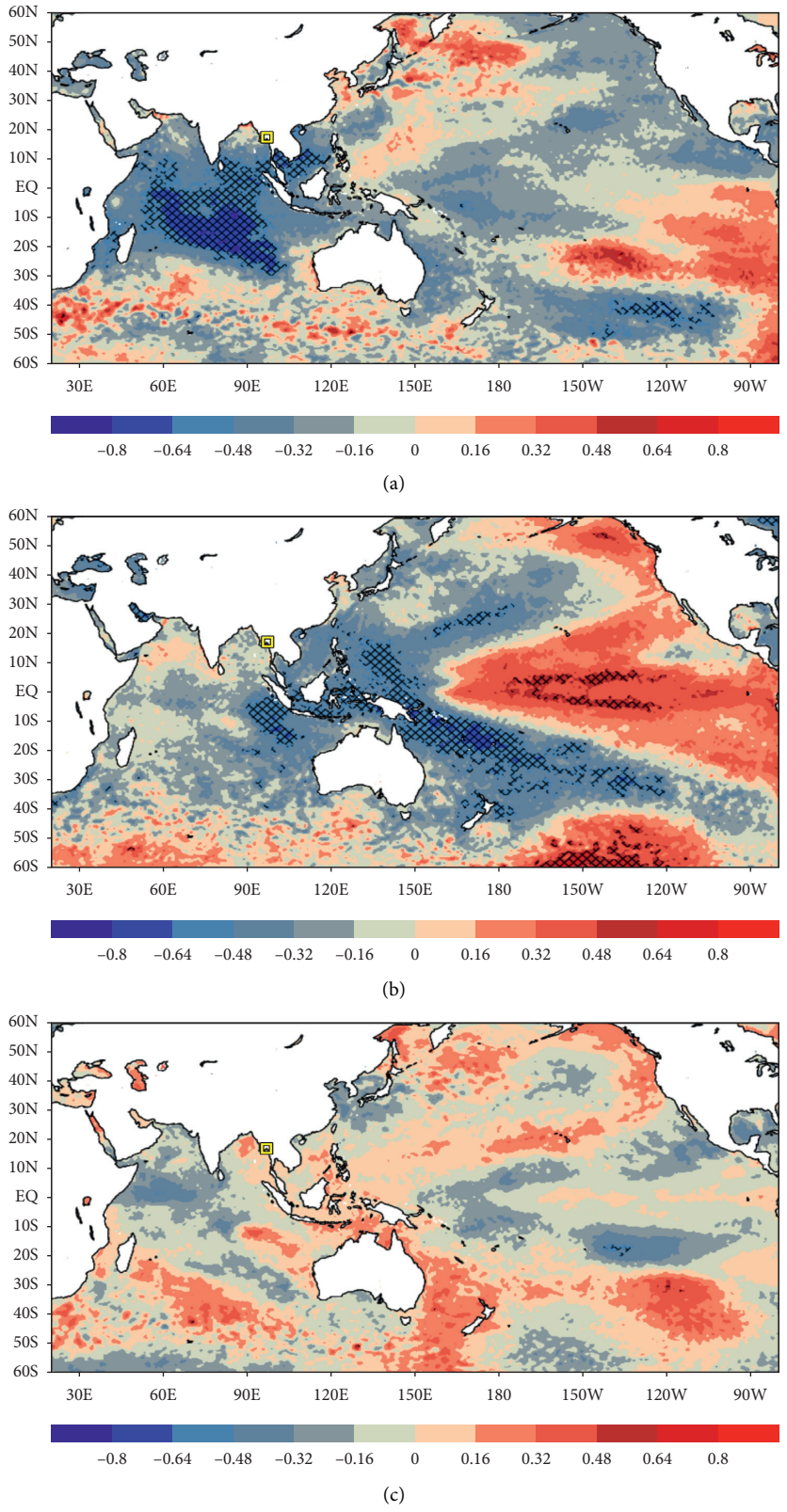

Figure 16: Correlation of SST with convective rainfall over the VYYY (shaded) and correlation significant area (hatched) for (a) annual, (b) summer (JJAS), and (c) winter (DJF) at 95% confidence level.

Table 1: Lagged correlation of JJAS rainfall with NINO, IOD, and IO during 1991–2020.

	NINO 3–4	IOD	IO
Annual	−0.18 ($p = 0.35$)	0.05 ($p = 0.81$)	−0.65 ($p < 0.01$)
JJAS	0.50 ($p < 0.01$)	0.14 ($p = 0.45$)	−0.17 ($p = 0.37$)
DJF	−0.02 ($p = 0.93$)	−0.44 ($p = 0.02$)	−0.14 ($p = 0.47$)

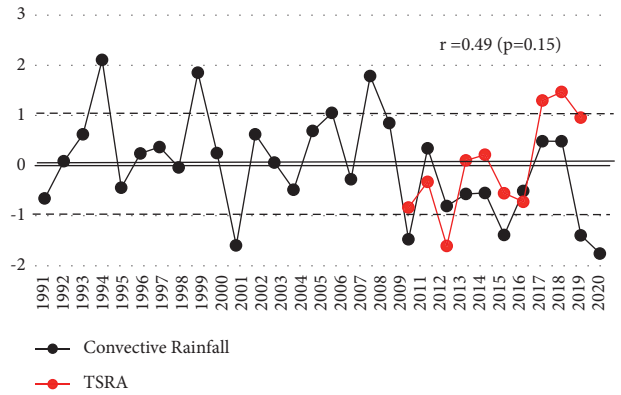

Figure 17: Interannual variability of standardized anomalies of TSRA occurrences (observation data) and convective rainfall (ERA5 reanalysis data) over the VYYY; the black line is the reference line and the black-dotted line bounds the value of ±1 above or below years, assuming that there are exceeding or less years of convective rainfall over study area during 1991–2020.

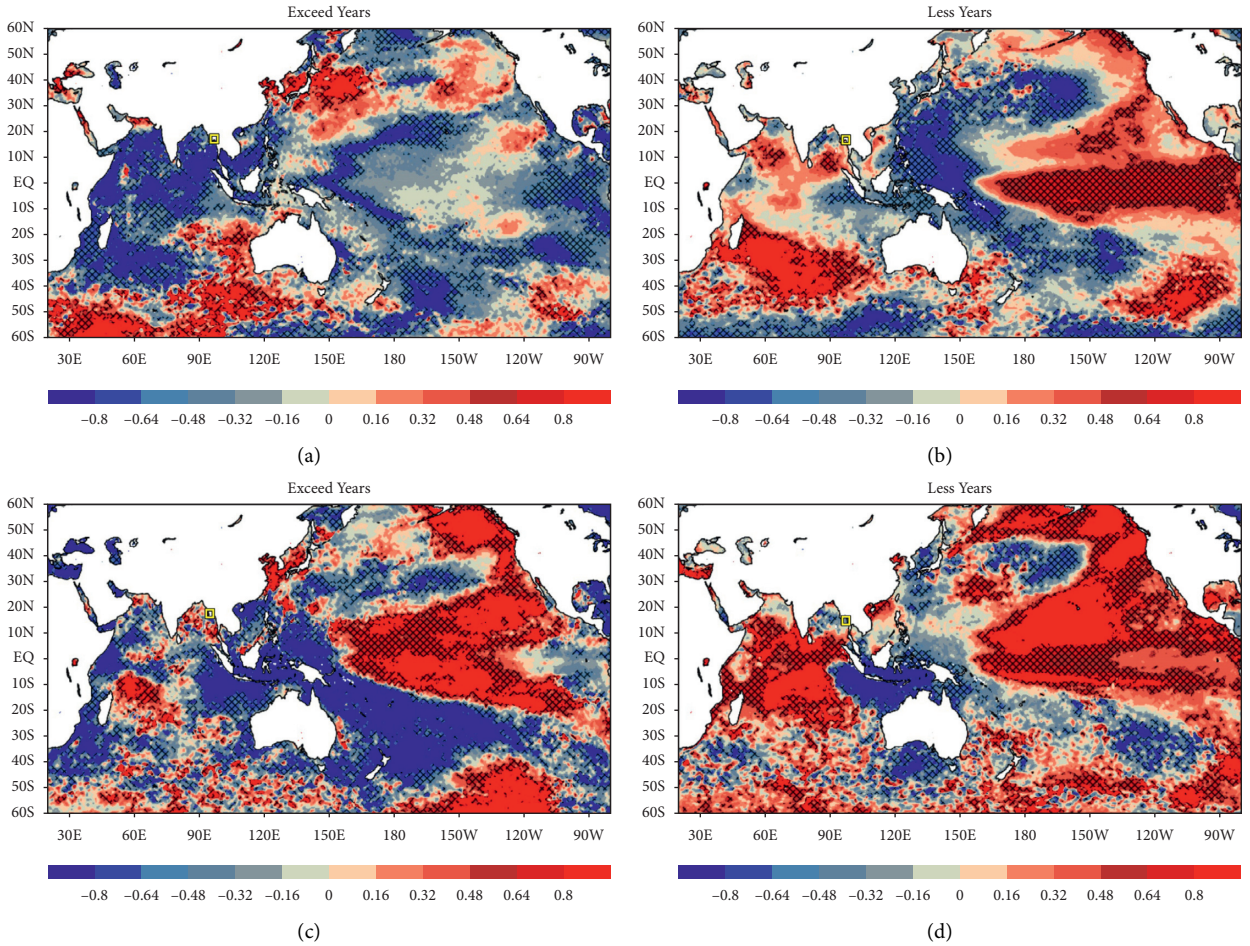

Figure 18: Correlation of SST with convective rainfall over the VYYY (shaded) and significant area (hatch) of (a) annual of exceeding years, (b) annual of less years, (c) summer (JJAS) of exceeding years, and (d) summer (JJAS) of less years based on Figure 17 during 1991–2020 at a 95% confidence level.

summer (JJAS). It is discovered that IO SST anomalies are the main driver of convective rainfall over the study area during summer (JJAS). Because SST anomalies over NINO 3-4 region have positive correlation in both exceeding and less years of summer (JJAS) (Figure 18(c) and 18(d)). The spatial result agrees with the previous temporal result in Table 1. But IO has only dominant different negative (positive) during exceed (less) years in annual analysis (Figures 18(a) and 18(b)). As a result of Figure 18(b), the positive anomalies, the warm phase of ENSO and IO SST may result in less convective rainfall over the study area. In contrast, the reverse pattern can be found during the years covered by Figure 18(a).

Generally, yearly frequency analysis showed how TSRA days occur more frequently year by year due to global climate change. During the eleven years (2009–2019), the minimum occurrences were 255 times in 2010. The average number of occurrences is 527, with 920 occurrences in 2018. Thunderstorms have occurred at their peak during half of the summer and the entire southwest season, and they have occurred at their peak at Yangon International Airport for at least 8 months. The maximum frequency of occurrence is 22% in July, the minimum occurrence is 1% in January, and there are no occurrences in February, March, and December. The annual CAPE values over local airport regions, the Bay of Bengal (BOB), the western equatorial Pacific, and the South China Sea show a strong positive correlation with convective rainfall over the study area. In contrast, negative CIN anomalies have been observed over the same areas as above, except for the western part of BOB along the Indian Coast. This indicates that these places had a good possibility of experiencing convective activity. Furthermore, the annual component wind, which blows from the southwest sea to the northeast, may result in increased moisture transport to the BOB's northeast continental area and encourage convective rainfall over the airport regions. Interannual convective rainfall has no significant correlation with SST at NINO 3-4 (5N–5S and 170W–120 W) in the Pacific Ocean, but there is a clear negative correlation over the Indian Ocean. However, the results of a seasonal connection analysis demonstrate a favorable correlation over the Nino 3-4 region, especially in the summer southwest monsoon season (JJAS). The major conclusion shows that, during the summer El Nino phase of ENSO, more convective rainfall may occur (JJAS). Increased convective rainfall over the research area may possibly be a result of negative IO SST anomalies. Positive anomalies, the warm phase of ENSO, and the IO SST, on the other hand, may result in less convective rainfall over the research area [34–19].

4. Conclusions

"Before-Flight-Briefing without weather discussion will lead to your flight as a blindfold beyond your vision."

Hlaing Myint (Flight Captain, Air Thanlwin, Myanmar).

On a day-to-day basis, the airliner is routed to take advantage of weather or atmospheric elements (e.g., jet stream tailwind to improve fuel efficiency). In addition, every pilot and aircrew need to know what weather situation has occurred on their route of flight. Before each flight, pilots should obtain all the pertinent information relevant to the flight's nature. A weather briefing obtained by the pilot from an approved weather source, via the Internet and/or from weather forecasting professional, is included in this.

In this study, we can learn the climatology of Yangon International Airport, which is a vital resource for the country's economic gateway. Weather forecasters or specialists can get a lot of important and useful information for weather forecasters or specialists, such as analyzing what weather situation is the most important or best time for flight operations. Fog and haze weather phenomena are most common in the winter. Thunderstorms, on the other hand, have been most common during the first half of summer and the entire southwest monsoon season, which lasts at least eight months. After examining numerous characteristics of Yangon International Airport, we identified which elements had a big impact on operations, and we obtained a lot of practical information from the operators during the important interview phase. Weather, notably TSRA and visibility, can influence aviation mishaps, as seen in the accident case study section. As a result, we identified two meteorological occurrences (TSRA and fog) that were extremely likely to result in plane crashes or operational delays. TSRA poses a greater risk than fog because it is linked to a variety of other weather phenomena such as hail, wind shear, and lightning. Yearly frequency of occurrence research revealed that, as a result of global climate change, TSRA days occur more frequently year after year. The lowest number of occurrences was 255 times in 2010 throughout the eleven years (2009–2019). With 920 occurrences in 2018, the average number of occurrences is 527. Thunderstorms peaked in the second half of the summer and throughout the entire southwest season, and they peaked at Yangon International Airport for at least eight months. In July, the largest frequency of occurrence is 22%.

The annual CAPE across local airport districts, the Bay of Bengal (BOB), the western equatorial Pacific, and the South China Sea is strongly correlated with convective rainfall over the study area. In contrast, negative CIN anomalies have been found over the same locations as above, except for the western part of BOB near the Indian Coast. This indicates that the study area had a good possibility of experiencing convective activity significantly. Furthermore, the annual component wind, which travels from the southwest to the northeast, could improve moisture delivery to the BOB's northeast continental area and encourage convective activity. In the Pacific Ocean, there is no significant link between interannual convective rainfall and SST at NINO 3-4 (5N–5S and 170W–120 W), whereas there is a distinct negative correlation over the Indian Ocean. But seasonal analysis reveals a positive link in the NINO 3-4 zone, especially during the summer monsoon season in the southwest (JJAS). The key finding suggests that more convective rainfall may occur in the El Nino phase of ENSO during the summer (JJAS) at study area. Negative IO SST anomalies may also result in increased convective rainfall over the study area. In contrast, the positive anomalies, the warm phase of ENSO and IO SST, may result in less

convective rainfall over the study area. This may lead to direct or indirect influence over aircraft operation and accident prevention due to convective clouds or thunderstorms, which are high-risk aviation hazards as everyone knows. The main innovation is that we investigate the effects of thunderstorms on airport operations before determining their relationship with ENSO and the IOD separately and combined during their complete phases. The present finding has another implication for forecasters. Thus, to obtain a realistic prediction of Yangon International Airport, we also need to study other variables and need to simulate the model. According to a well-known physicist in another context, the current discovery raises a new question and a new possibility for viewing climatology from a new perspective and making significant progress in the predictability study.

Data Availability

Meteorological statistical data (METAR) based on the recommendations of the International Civil Aviation Organization (ICAO) and the World Meteorological Organization (WMO) are obtained from the Department of Meteorology and Hydrology (DMH, Myanmar) and the University of Wyoming (http://weather.uwyo.edu/surface/meteorogram/seasia.shtml), and these can be obtained freely. Flight delay and accident data are obtained from Aviation Safety Network (ASN) (aviation-safety.net) and ICAO Safety API Data Service (ICAO.int). These also can be downloaded freely. Historical Himawari-8 satellite images developed by Japan Meteorological Agency can be obtained from JAXA Himawari Monitor (P-Tree System) freely. Aerodrome's data are supported by YIA Service Company Limited and MC-Jalux Airport Services Company Limited and hence cannot be freely distributed. Requests for access to these data should be made at https://yangonairport.aero/index.php/en/. The SST NINO 3.4 indexes (area-averaged SSTA over 150W–90W, 5S–5N) data are taken from the website of the National Centre for Atmospheric Research (US), Climate Data Store, and they can be obtained freely from NINO SST Indices (NINO 1 + 2, 3, 3.4, 4; ONI and TNI) | NCAR-Climate Data Guide (ucar.edu). CAPE Index value, K-Index, and Bay of Bengal SST data are taken from ERA5 reanalysis data from ECMWF (https://cds.climate.Copernicus.EU/cdsapp#!/home?tab=overview). The above datasets are now freely available from 1950 to the present by registration at ECMWF. Open Grads (OpenGrADS-Home), climate data operator (https://code.mpimet.mpg.de/), and IBM SPSS are mainly used for this study. Among these the first two are open-source applications for everyone.

Conflicts of Interest

The authors declare that there are no conflicts of interest with the publication of this article.

Acknowledgments

The researchers extend their gratitude to all of the professors who approved and supported this research, as well as the Nanjing University of Information Science, for their assistance in completing it. The authors would like to express their gratitude to the Department of Meteorology and Hydrology for their support of Myanmar data, as well as Professor Larry Oolman of the University of Wyoming's Department of Atmospheric Science, for his support of METAR data for airfields. Professor U Chit Kyaw, Department of Meteorology and Hydrology, Professor Badri Jijelava, Head of Met Office at SAKAERONAVIGATSIA, and Captain Hlaing Myint, Air Thanlwin, deserve special thanks for their contributions to research concepts and analysis procedures, and Captain Hlaing Myint, Air Thanlwin, deserves special thanks for coordinating the questionary survey. Also, the authors want to express their gratitude to all Myanmar aviation services, particularly Myanmar National Airline and Aviation Safety Network, for providing data for this paper. Finally, the authors would like to express their gratitude to Professor Wang Wen of Nanjing University of Information Science and Technology for supervising this study and providing support throughout the research process.

References

[1] A. Gittens, S. Hocquard, A. de Juniac, F. Liu, and E. Fanning, "Aviation Benefits Report," *International Civil Aviation Organization*, vol. 76, 2019, https://www.icao.int/sustainability/Documents/AVIATION-BENEFITS-2019-web.pdf.

[2] Industry High-level Group, *Aviation Benefits Report*, p. 76, 2019.

[3] M. Vorstenbosch and W. van der Pijl, "Myanmar seafood exports - quick scan of the eu market potential," pp. 1–28, 2012.

[4] PricewaterhouseCoopers, "Myanmar Business Guide," vol. 3, pp. 1–38, 2012.

[5] D. C. A. (Myanmar), "AIP MYANMAR — YANGON/YANGON INTERNATIONAL," vol. 24, 2019.

[6] Bureau of Transportation Statistics, "Delay cause by year, as a percent of total delay minutes," Bureau of Transportation Statistics, Wahington, Dc, USA, 2019, https://www.bts.gov/delay-cause-year-percent-total-delay-minutes.

[7] WMO (World Meteorological Organization), "World meteorological organization aviation hazards," *Techniques*, vol. 1390, 2007.

[8] V. Lo, "Weather index project: investigating the effect of weather on flight delays," 2013.

[9] R. Dorian and T. Robinson, ""IATA guidance booklet: airport ownership and regulation," the world bank/public - private infrastructure advisory facility," 2018, https://www.iata.org/policy/infrastructure/Documents/Airport-ownership-regulation-booklet.pdf.

[10] "No Title," *Visibility*, https://www.skybrary.aero/index.php/Visibility.

[11] ATC Service Back to Normal in Myanmar – International Ops 2021 – OPSGROUP." https://ops.group/blog/atc-for-overflights-in-myanmar-following-military-coup/.
[12] ICAO, "Annex 3, meteorological service for international air navigation," 2018.
[13] Frequency Analysis - an Overview | ScienceDirect Topics." https://www.sciencedirect.com/topics/earth-and-planetary-sciences/frequency-analysis.
[14] K. Carlson and J. Winquist, "Introduction to statistics and frequency distribution," *An Introduction to Statistics: An Active Learning Approach*, vol. 23, pp. 1–32, 2014.
[15] K. Hamal, S. Sharma, B. Baniya, N. Khadka, and X. Zhou, "Inter-annual variability of winter precipitation over Nepal coupled with ocean-atmospheric patterns during 1987-2015," *Frontiers of Earth Science*, vol. 8, 2020.
[16] N. H. Saji, P. N. Goswami, P. N. Vinayachandran, T. Yamagata, and N. A. Saji, "Dipole mode in the tropical indain ocean," *Nature*, vol. 401, pp. 360–363, 1999, http://www.nature.com/doifinder/10.1038/43854%0Apapers3://publication/doi/10.1038/43854.
[17] E. E. Zin, "Myanmar Climate Report," *Norwgian Meterological Inst*, vol. 9, p. 105, 2017, http://files/679/MyanmarClimateReportFINAL11Oct2017.pdf.
[18] V. Krishnamurthy and J. Shukla, "Intraseasonal and interannual variability of rainfall over India," *Journal of Climate*, vol. 13, no. 24, pp. 4366–4377, 2000.
[19] A. P. Dimri, "Sub-seasonal interannual variability associated with the excess and deficit Indian winter monsoon over the Western Himalayas," *Climate Dynamics*, vol. 42, no. 7–8, pp. 1793–1806, 2014, https://go.gale.com/ps/i.do?p=AONE&sw=w&issn=09307575&v=2.1&it=r&id=GALE%7CA380747281&sid=googleScholar&linkaccess=fulltext.
[20] S. Cheng, Y. Zhang, S. Hao, R. Liu, X. Luo, and Q. Luo, "Study of flight departure delay and causal factor using spatial analysis," *Journal of Advanced Transportation*, vol. 2019, pp. 1–11, 2019.
[21] L. Dray, "An empirical analysis of airport capacity expansion," *Journal of Air Transport Management*, vol. 87, p. 101850, 2020.
[22] S. Borsky and C. Unterberger, "Bad weather and flight delays: the impact of sudden and slow onset weather events," *Economics of Transportation*, vol. 18, pp. 10–26, 2019.
[23] Airport Statistics Paris, Charles De Gaulle | CDG." https://airportinfo.live/airport-statistics/cdg-paris-charles-de-gaulle.
[24] Final Report of Runway Excursion Accident of Air Bagan," vol. 72, pp. 1–23, 2015.
[25] ASN Aircraft Accident Shaanxi Y-8F-200W 5820 Dawei." https://aviation-safety.net/database/record.php?id=20170607-0.
[26] 20 Suffer Injuries in Biman Airline Crash | the Myanmar Times." https://www.mmtimes.com/news/20-suffer-injuries-biman-airline-crash.html.
[27] L. L. Aung, "Myanmar Climate Report," *Norwgian Meterological Inst*, vol. 9, p. 105, 2017.
[28] K. T. Oo, *Thunderstorm Days in Yangon International Airport*.
[29] A. McGregor, L. Law, G. Banks, W. Murray, and N. I. ÑO. EL, "Taking stock: reflecting on AsiaPacificViewpoint," *Asia Pacific Viewpoint*, vol. 55, no. 1, pp. 1–5, 2014.
[30] A. Thompson, "Rain from thunderstorms is rising due to climate change - scientific American," 2017, https://www.scientificamerican.com/article/rain-from-thunderstorms-is-rising-due-to-climate-change/.
[31] S. Das, "Severe Thunderstorm observation and modeling – a review," 2018.
[32] S. S. V. S. Ramakrishna, "Prediction of severe thunderstorms over Sriharikota Island by using the WRF-ARW operational model," *Remote Sens. Model. Atmos. Ocean. Interact. VI*, vol. 9882, Article ID 988214, 2016.
[33] P. Summary, L. Index, and M. C. Updraft, "Convective Available Potential Energy (CAPE)," 2014.
[34] D. J. Parker, "The response of CAPE and CIN to tropospheric thermal variations," *Quarterly Journal of the Royal Meteorological Society*, vol. 128, no. 579, pp. 119–130, 2002.
[35] Inter-annual Variability of Moisture Transport over the Northern Indian Ocean and South Asian Summer Monsoon on JSTOR." https://www.jstor.org/stable/26496989.
[36] M. A. Alexander, I. Bladé, M. Newman, J. R. Lanzante, N.-C. Lau, and J. D. Scott, "The atmospheric bridge: the influence of ENSO teleconnections on air-sea interaction over the global oceans," *Journal of Climate*, vol. 15, no. 16, pp. 2205–2231, 2002.
[37] C. Li and T. Zhao, "Seasonal responses of precipitation in China to El Niño and positive Indian Ocean Dipole modes," *Atmosphere*, vol. 10, no. 7, pp. 372–7, 2019.

Hindawi
Advances in Meteorology
Volume 2022, Article ID 1279625, 13 pages
https://doi.org/10.1155/2022/1279625

Review Article

Overview of the Application of Orographic Data in Numerical Weather Prediction in Complex Orographic Areas

Yingjie Wang [1,2] **and Jianping Wu** [2]

[1]*College of Computer Science and Technology, National University of Defense Technology, Changsha, China*
[2]*College of Meteorology and Oceanography, National University of Defense Technology, Changsha, China*

Correspondence should be addressed to Jianping Wu; wjp@nudt.edu.cn

Received 5 January 2022; Accepted 18 March 2022; Published 30 March 2022

Academic Editor: Feng Chen

Complex orography is still a big challenge for all numerical weather prediction (NWP) models. Orography is an important factor that affects the NWP results. The orography in NWP mainly affects the main accuracy of the results through two aspects: orographic representation in models dynamics and orography-related parameterization schemes in the physical processes. To ensure the accuracy of NWP results, it is necessary to have a comprehensive understanding of the application of orographic data in NWP. This paper summarized the influence of orography on weather, the influence of orographic representation on prediction accuracy, and the parametrization of orography-related drag in NWP models. Finally, this paper elaborates the problems of the application of orographic data in NWP and looks forward to future directions in this field, hoping to improve the performance of NWP in complex orographic areas and provide a reference for better application in NWP.

1. Introduction

Orography plays an important role in atmospheric motion at different scales, and it also has an important influence on the movement and evolution of a weather system. When air flows through uneven mountains, the orography causes the airflow to climb and go around orography, and this affects the atmosphere's energy transmission and budget through its thermal action. Currently, numerical weather prediction (NWP) models are widely used with the development of computer technology. However, various NWP and climate models still have a typical problem; that is, they cannot accurately predict the intensity and structure of the zonal flow in complex orographic areas. Orography is one of the key factors affecting the prediction accuracy of NWP models [1, 2].

The NWP in complex terrain has always been a research hotspot because of its inaccurate predictions. For example, Moya-Álvarez et al. [3] studied the simulation of rainfall under complex orographic conditions such as the central Andes of Peru by the Weather Research and Forecasting Model (WRF). In normal simulations, the model overestimated the amount of precipitation, but in extreme precipitation and hail weather, the model underestimated the amount of precipitation. It can be seen that there is still a lot of room for improvement in the numerical prediction in complex orographic areas. Inappropriate representation of the current land, especially the inappropriate description of orography and biophysical parameters in specific spatial areas, has led to the uncertainty of simulation from local to regional scales in the NWP model [4]. Caccamo et al. [5] used different grid resolutions and orographic data to simulate the impact of heavy rainfall event in Sicily when studying weather prediction performances for complex orographic areas. It is found that it was still a challenge to provide accurate and timely prediction of extreme rainfall in complex orographic areas. However, if appropriate high spatial resolution models are used, the forecast performance can be effectively improved. Mass et al. [6] also found that in coastal areas with complex orography, high-resolution NWP models can improve forecasting skills. Besides, Alpert et al. [7] also found that the high-resolution NWP models have

better performance in capturing precipitation in high-altitude areas. One of the main reasons is that the representation of orography can be improved at high resolution.

Around the 1950s, there was no orographic data in the various digitized versions that are now available. The first orographic data used in NWP models was read from aeronautical orographic charts (Figure 1) [8]. At that time, orographic heights were averaged by eye over one-degree squares, and aeronautical charts were not complete, so there was an urgent need to develop a set of orographic datasets with high quality and high global coverage. However, with the development of satellite and remote sensing technology, various global datasets with different resolutions have been developed, such as ETOPO5, GTOPO30, Shuttle Radar Topography Mission data (SRTM), and ASTER GDEM [9–11]. Later, these orographic datasets started to be applied to various global and regional NWP models and greatly improved the model performance [4, 5, 12–15]. In addition, orographic data of various regions were generated, such as the high-resolution orographic dataset of the Heihe River Basin [16]. Different resolutions of orographic data represent different orographic characteristics. As a result, different meteorological features and different weather phenomena will be obtained if different orographic data are utilized. Nunalee and Horváth [17] compared the prediction results from orographic data with different resolutions and confirmed that different orographic data can generate completely different orographic wake mechanics, such as whether or not vortex shedding exists. Vortex shedding means that when the wind hits a mountain and flows along its surface, the airflow will change, and a circulating vortex will be generated at the end of the airflow. He et al. [18] compared the simulation results from various orographic data, including the Shuttle Radar Topography Mission (SRTM), and found that orographic data had a much higher impact on temperature than precipitation.

Complex orography is still a big challenge for all NWP models [19]. Orography is the key factor in the inaccuracy of NWP results in complex orographic areas. The orography in NWP mainly affects the accuracy of the results through two aspects: orographic representation in models dynamics and orography-related parameterization schemes in the physical processes (Figure 2). Hence, to predict the weather more accurately in complex orographic areas, it is essential to have a comprehensive understanding of the application of orographic data in NWP. As shown in Figure 2, this paper reviewed recent developments from several aspects, including the influences of orography on weather, the influence of orographic representation on prediction accuracy and the parametrization of orography-related drag in NWP models, hoping to provide references for future studies and operations.

2. The Effect of Orography on Weather

When Dimri [20] simulated rainfall caused by an active western disturbance in India, it was found that the distribution and rate of rainfall were highly sensitive to orography. It can be seen that orography is an important factor affecting rainfall. However, the basic mechanisms of orographic rainfall had not yet been fully resolved. The large number of physical processes involved and interactions between different processes make the quantitative prediction of rainfall in complex orography a difficult task [21]. The influence of orography on rainfall has been a hot topic since ancient times. For example, Oikonomou et al. [22] utilized the regional climate model, RegCM3.1, to set up two simulation experiments. One retained the land cover data but removed the orographic height in the study area to become a flat orography. This was termed the "flat experiment." The other preserved the original orography to study the relationship between the Greek orography and prolonged drought. It was found that due to the effect of orography, there was a significant precipitation system between the Greek mainland and Crete Island. When the orographic height was removed, the duration of extreme drought was significantly extended. This indicated that the orography had a very important impact on the distribution of local extreme drought. Alpert et al. [7] also found that there is a significant relationship between seasonal precipitation and orographic altitude. Sethunadh et al. [23] simulated a rainstorm event over the city of Chennai using the high-resolution regional National Center for Medium Range Weather Forecast (NCMRWF) Unified Model (UM). After improving the orographic representation, it was found that the local details of the rainfall distribution were better simulated. The possible reason is that after improving the orographic representation, the detailed orographic features that affect rainfall have been more realistically represented. Torma and Giorgi [24] studied the rainfall in the Carpathians Mountains and found that the elevation, size, and orientation of the mountains in the complex orography play a key role in the occurrence and changes of rainfall. Besides, many scholars have also studied the relationship and mechanisms between orography and rainfall [17, 25, 26]. It can be seen that orography plays an important role in the generation and development of rainfall. In the global distribution of heavy rain (Figure 3(a)), most of the rainstorm centers were located near complex orographic areas, such as the Qinghai-Tibet Plateau, Cordillera Mountains, Appalachian Mountains, Andes Mountains, and so on [27]. In the average number of rainstorm days in eastern China (Figure 3(b)), the areas with the most rainstorm days were mostly located on the southeast windward slope of mountains, such as Taihang Mountains, Funiu Mountains, Dabie Mountains, Wuyi Mountains, and Nanling Mountains. When a rainfall weather system moves closer to a mountainous area, orography can make the original weather system without precipitation begin to show precipitation, and the distribution of rainfall in the weather system with precipitation becomes very uneven. As a result, in some parts of the mountain, there will be more rainfall, and the duration of the rainfall will also be prolonged. These effects are called the orographic effect of increasing rainfall [28]. Although the movement of weather systems with water vapor to mountains areas is an important factor in rainfall, the Mesoscale Alpine Project (MAP) in 1999 showed that change of orography on airflow was a crucial factor affecting the

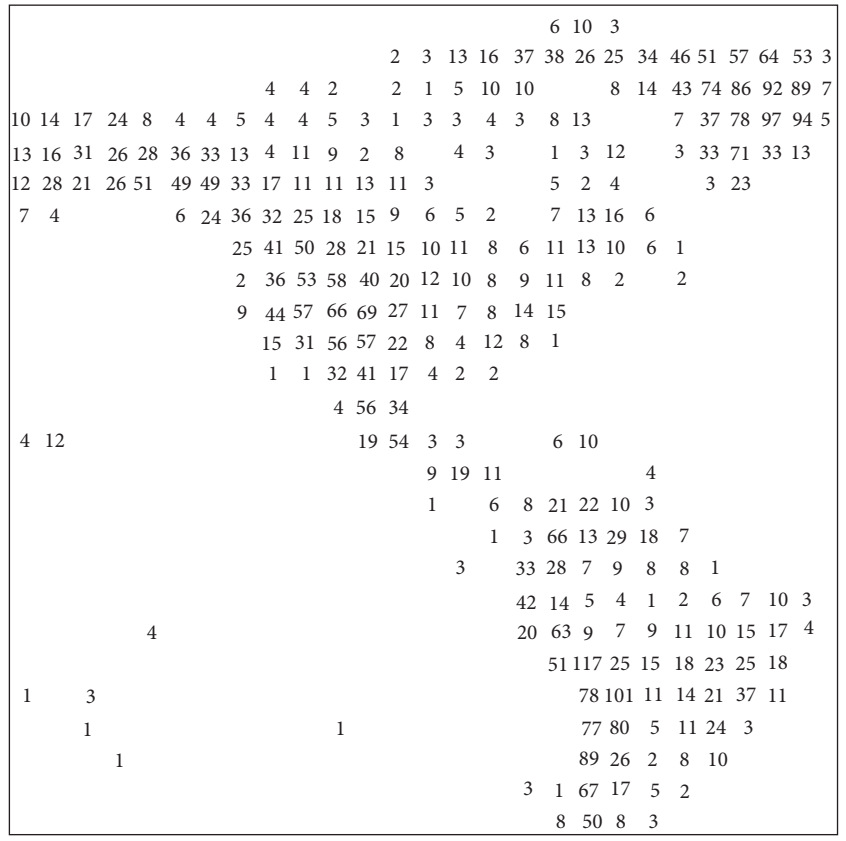

Figure 1: Section of a table showing the hand-digitized orography of Western Hemisphere at a resolution of five degrees latitude and longitude from [8].

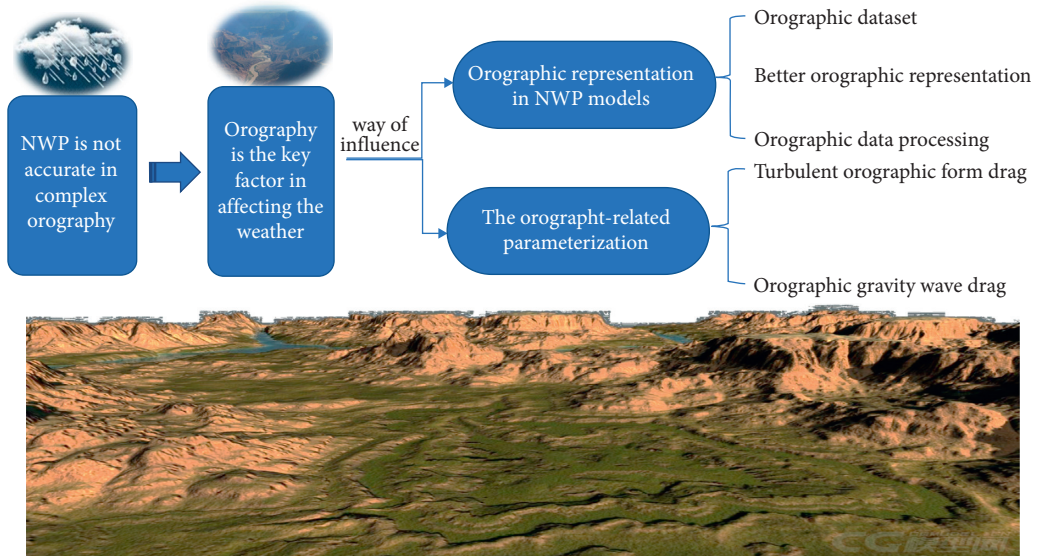

Figure 2: Application of orography in numerical weather prediction.

location, intensity, and duration of orographic rainfall [29]. MAP studied how complex alpine orography affects moist stratified airflow to generate rainfall, primarily by determining the location and rate of vertical airflow movement and microphysical processes associated with enhanced local rainfall. The MAP has greatly improved the understanding of orographic rainfall [30, 31]. In specific rainstorm cases, such as the "7·20 Heavy rainstorm in Zhengzhou" event in 2021, the center of the rainstorm was mainly concentrated on the east and south sides of the mountain. On the windward slope, with the increase of orographic height to the east, the change of rainfall was gradually obvious. Finally, the blocking, convergence, and upward movement of airflow generated by the Funiu Mountain caused the rainfall (Figure 4) [32].

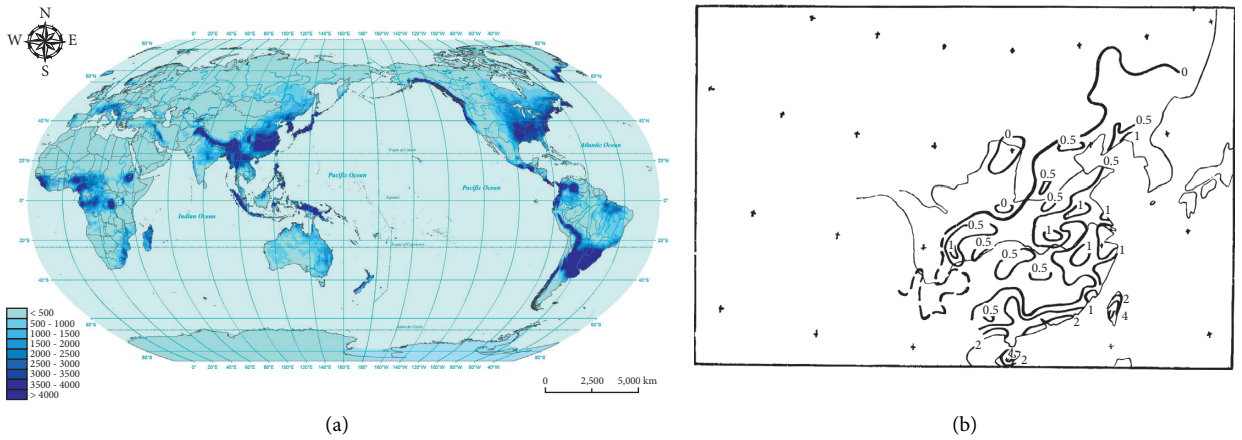

FIGURE 3: The spatial distribution of heavy rainfall. (a) The global average annual heavy rainfall over land from 1991 to 2000 (units: mm·10a^{-1}) [27]. (b) Average number of days with heavy rain in eastern China (daily rainfall ≥100 mm) [28].

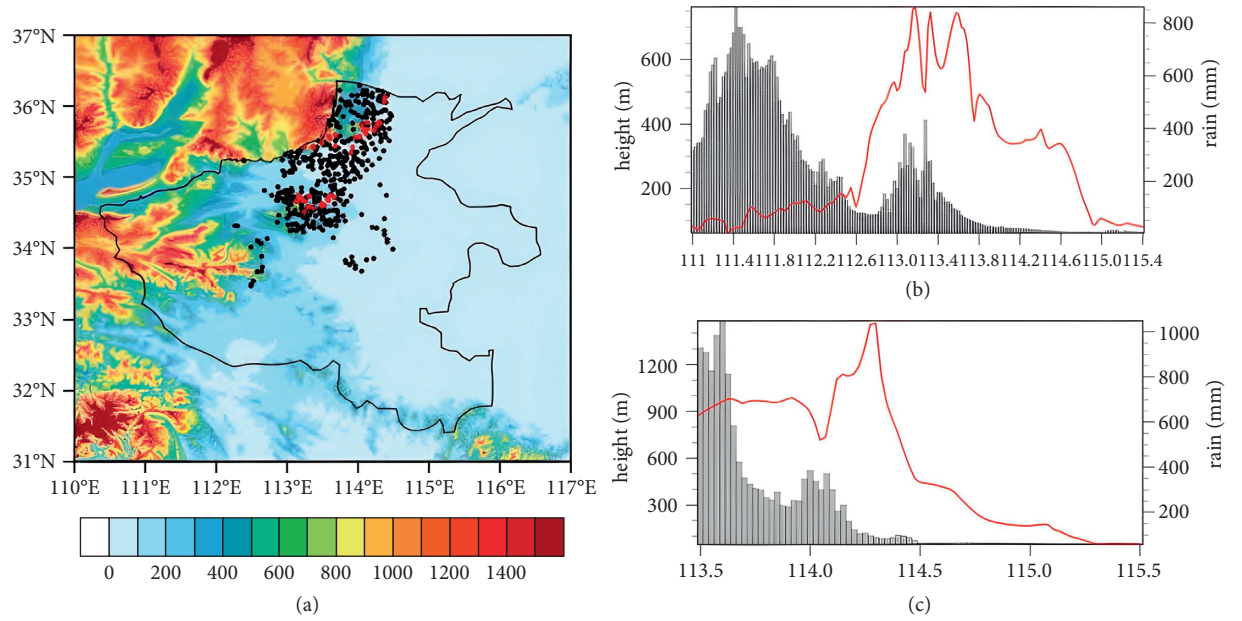

FIGURE 4: The heavy rainstorm from 08:00 on 17th of July to 08:00 on 23rd of July, 2021, in Zhengzhou, China. (a) The site distribution of process accumulated rainfall larger than 400 mm and less than 800 mm (black dots) and larger than 800 mm (red dots) (filled color represents altitude, units: m). (b) The variation curves of altitude (columnar shadow) and process accumulated rainfall over the Zhengzhou station 34.7°N and (c) the station 35.77°N [32].

The orography not only has a great influence on rainfall, but also has a great influence on other weather systems and meteorological elements. For example, Renault et al. [33] found that the vortex stretching and the surface drag related to turbulent momentum flux divergence caused by orography enhanced the drag coefficient on land and caused a significant decrease in wind speed. Obermann-Hellhund and Ahrens [34] simulated Mistral and tramontane using orography of different resolutions and also found that the reduction of orographic details (low-resolution orography) would lead to a change in wind pattern change and a reduction in wind speed. Huang and Wu [35] studied the effect of ideal orography on upstream tropical cyclone track. It was found that when the tropical cyclone was still far away from the orography, the changes in the background flow caused by the orography firstly caused large-scale steering current to push the tropical cyclone to the southward. When the tropical cyclone approached the ideal orography, the role of inner-core dynamics became very important and the channel effect generated by orography caused tropical cyclone to deflect further south. In addition, the subgrid scale orography also has a great influence on various weather processes and climate. It is discussed in detail in Section 4 of the article. The steepness of the orography is also very sensitive to different meteorological models and vertical coordinates. Yudin [36] applied two nonhydrostatic numerical models, a finite-difference model and a finite-element model, to predict gravity wave propagation. The finite-

difference model is suitable for smooth orography, and the finite-element model is suitable for steep orography. Gallus [37] used the National Center for Environmental Prediction (NCEP) regional Eta model, and used the Eta vertical coordinate and stepwise treatment of orography to replace the terrain-following sigma vertical coordinate, to study the influence of the stepped orography on the flow near the mountains. It was found that the stepped orography caused a significantly underestimate of wind speeds at leeward side of mountains during the storm and stepped orography caused weaker mountain waves than generated when the sigma vertical coordinate was used.

Most of these studies use sensitivity experiments to study the impact of orography on the weather. By changing the orographic conditions in NWP models, people can better understand its impact and improve the accuracy of NWP. Sensitivity tests can clearly explain the influence of orography on weather and provide a quantitative measure of the impact of orography, and this has become a research hotspot. However, sensitivity tests have primarily been confined to specific phenomena, specific parts of the world, or to specific parameterization schemes. This has no universal practicality to the regional NWP and does not improve the accuracy of operational NWP models. As a result, we should develop quantitative methods in future studies to improve the practicality and universality.

3. Orographic Representation in NWP Models

With the wide application of various NWP models, the accuracy of weather prediction results has greatly improved [38, 39]. However, if in a complex orographic area, the prediction of the value of meteorological elements, such as precipitation and wind, would still be inaccurate. This is primarily because of the uncertainty of the orography representation and orographic drag parametrization [39]. Chapter 3 will mainly discuss the representation of orography, and the parameterization of orographic drag will be discussed in Chapter 4. To ensure the accuracy of NWP results, we need not only to understand the general influence of a regional orography on weather, but also to choose a set of orographic data and orography processing schemes suitable for NWP. This would be of great benefit to improve and optimize future NWP operations.

3.1. What Kind of Orographic Data Is Better? The main challenge of NWP models in complex orographic areas is that it is difficult to accurately represent the orography. In NWP models, when orographic height is represented by the discrete numerical grid, the value of each grid point represents the average orographic height in this grid, but it cannot represent the change of orographic height within the unit grid. Therefore, at a certain resolution of the NWP model, the grid values of the model implicitly smooth the orographic height, which reduces the actual orographic height, causing the model to underestimate the blocking effect of mountains [40]. When the NWP model uses a higher resolution, the numerical grid area of the model will be smaller, which means that the representation of orographic height may be more accurate. Then, does a higher resolution lead to a better result?

For orographic dataset, the orographic resolution includes the resolution of the original orographic data and the resolution of the orographic data after interpolation. Some scholars have noted that high-resolution orographic data in climate models are essential to improve the accuracy of precipitation prediction results in mountainous regions [24]. Gao et al. [41] used the regional climate model, RegCM2, to predict the precipitation of East Asia. They used "actual orography" made by the National Center for Atmospheric Research (NCAR). This means that the orographic height was the original data and had not been interpolated and processed, and they used very smooth model orography that refers to the original orographic data after processing. Then, they interpolated these two orographic data into different resolutions. Finally, they compared the simulated precipitation results. They found that the prediction accuracy of rainfall in East Asia depended on the resolution of the orographic data. The higher the resolution, the better the accuracy. However, if the resolution was the same, the simulation of the "actual orographic" data was better than that of using the smoothed orographic data. For the high-resolution orographic data with a resolution of 30 m produced by the Chinese Academy of Sciences and Global 30″ orographic data produced by the United States Geological Survey (USGS) in the Black River Basin, Liu et al. [16] used these two datasets to predict the meteorological fields by the Mesoscale Model 5 (MM5) in the Black River Basin. The results showed that the higher-resolution data had a better capability to predict temperature and wind than the USGS data, but the improvement in the precipitation prediction was not obvious. This was different from the results of Gao et al. [41] who believed that the resolution of orography can greatly affect precipitation predictions. This might have been caused by the fact that the precipitation prediction is not only affected by orography, but also by many other factors including the performance of NWP models, differences in research areas, divergence of the orographic data, and other factors.

The SRTM and ASTER GDEM orography data have been widely used in weather prediction research because of its high resolution. Many scholars have conducted different studies on what is the best orographic dataset. For example, Zhang and Yin [12] predicted and compared the characteristics of meteorological features of atmospheric boundary layer in Huangshan and the surrounding areas of Anhui Province by replacing GTOPO30 (approximately 1 km resolution) orographic data produced by USGS with SRTM3 (approximately 90 m resolution) orographic data produced by the National Aeronautics and Space Administration (NASA) into the model WRF. This was combined with four boundary layer parametrization schemes. It was found that when the SRTM3 orographic data were used, the meteorological fields of the atmospheric boundary layer predicted from various boundary layer schemes were better than those from GTOPO30. In a word, the SRTM3 orographic data were better than GTOPO30 in the WRF. Caccamo et al. [5]

used the ASTER GDEM V2 orographic data (an approximate 1 arcsec resolution) produced by the Japanese Ministry of Economy, Trade and Industry (METI) and the NASA to replace the GTOPO30 orographic data (an approximate 30 arcsec resolution) produced by the USGS. Finally, they directly compared the observation data and the model prediction results and found that using the higher original resolution orographic data was key factors for accurate model prediction, especially for complex orography. Kirthiga and Patel [4] used SRTM orographic data to update the surface information and simulated micrometeorological and near-surface weather by the WRF model. In the modified run, it was found that the model better simulated the temporal changes in surface temperature, surface pressure, solar radiation, wind speed, and relative humidity. For these near-surface weather variables, the improvement in 24-hour forecast ranges from 15% to 30%. De Meij and Vinuesa [13] and De Meij et al. [14] simulated the effects of TOPO30 and SRTM orographic data on the 2 m temperature, the 10 m wind speed and rainfall by the WRF model and found that the result with SRTM orographic data was closer to reality. In addition, the prediction accuracy of the precipitation event was also increased. These studies showed that orography with high-resolution data, such as SRTM, could improve the accuracy of prediction results compared with the low-resolution data. The possible reason is that higher-resolution orographic data can reflect more realistic orographic conditions and represent smaller-scale orographic effect. Therefore, orography can be more resolved by NWP model, and the negative impact caused by the uncertainty of orographic representation is reduced.

3.2. The Processing of Orographic Data. Sometimes introducing high-resolution orographic data to a model may cause false disturbances, such as sudden abnormal increases or decreases in the value of meteorological elements, especially excessive wind speeds at some grid points. These problems have a significant impact on the performance and robustness of NWP models. Zhu et al. [42] studied the effect of high-resolution orographic data in a new-generation Global/Regional Assimilation Prediction System (GRAPES), developed by the China Meteorological Administration for the prediction of near-ground features (e.g., temperature and wind) in southern China. They found the 2 m temperature at 06Z to be a false oscillation; that is, its value had a sudden change that was possibly due to a lack of smooth orographic height in the model. Although high-resolution orographic data can improve NWP models accuracy, it should be recognized that a large number of experiments are still needed to study which orographic processing technology reduces the impact of high-resolution orographic "noise" on the dynamic calculation process to improve the stability and accuracy of NWP models. These studies show that filtering and smoothing the orographic field is effective to solve these problems.

Orographic processing began to appear and develop a long time ago. Davies and Brown [43] argued that an orographic filtering scheme should be used in grid point models under neutral and stable stratified flow regimes within the context of the nonlinear three-dimensional Blasius model [44, 45]. Research results show that orographic features with a length of more than or equal to six grid lengths were fully resolved, and orographic features less than two grid lengths could not be resolved but often actually harm the overall fidelity of NWP models. Therefore, an orographic smoothing scheme was needed here. These researches provided helpful information to later scholars. Webster et al. [46] applied the filter given by Raymond [47] to the UM as a scheme to filter orographic data. It was found that this filter can improve or eliminate excessive wind speed at some grid points. Later, Rutt et al. [48] proposed a novel, very flexible variational approach to orographic smoothing and studied its effects in the numerical model. It was found that new orographic smoothing scheme could reproduce the results of the schemes of Raymond [47] and Webster et al. [46]. Tu et al. [49] and He et al. [50] studied the impact of high-resolution orographic smoothing schemes on ground fields, such as the precipitation, in the GRAPES and WRF models using the Chebyshev polynomial filtering method. The results showed that the smoothed orographic data had a positive effect on the precipitation prediction under the complex orographic conditions on the eastern side of the plateau. Chen et al. [51] studied the effect of different orographic smoothing methods on precipitation forecasts using the WRF model. It was found that different orographic smoothing schemes could have different effects on the precipitation intensity and spatial distribution, and orography should not only be close to the actual orography as much as possible, but also reach a certain degree of smoothness. These studies have shown that that it is important to select better orographic smoothing schemes when using high-resolution orographic data.

4. The Orography-Related Drag Parameterization

As we all know, it is extremely important and necessary to represent orographic effects as accurately as possible in NWP models. However, due to the limitation of model resolution, small-scale orography cannot be resolved by models. The unresolved orography is called subgrid orography. When the orography is complex, current models cannot describe some features of small-scale orography well, such as slope and ridge direction. But subgrid orography plays an extremely important role in the model atmosphere in both the heat and motion aspects. In addition, it is usually difficult for model dynamics to deal with this problem with reasonable mathematical methods at current NWP models' resolution because the wavelength of the gravity wave excited by the subgrid orography is too small. Therefore, parametrization scheme to describe the effect of orographic drag on the weather system is currently a good method.

The orography-related drag parameterizations mainly include turbulent orographic form drag (TOFD) and orographic gravity wave drag (OGWD). In most NWP models, the orographic gravity wave drag parameterization scheme includes two parts, one is the orographic gravity wave drag,

and the other is the low-level blocking drag. The orographic workshop of the European Center for Medium-Range Weather Forecasts (ECMWF) made a suggestion that the orographic gravity wave and low-level blocking are parameterized at subgrid scales above 5 km, and the TOFD are parameterized at scales below 5 km [52]. Since it is generally believed that on smaller horizontal scales, vertical propagation of orographic gravity waves becomes less likely and 5 km is considered to be a reasonable limit. Of course, 5 km is not an exact value, but an approximate number. Davoli [53] considered this limit value to be 6 km.

4.1. Turbulent Orographic Form Drag (TOFD). In the last century, Fiedler and Panofsky [54] proposed the concept of effective roughness length. They defined the effective roughness length. The effective roughness length of the complex orographic area is equal to the roughness length of the area with uniform orography, the same surface stress. For a long time thereafter, the effective roughness method was used in NWP models to consider the effects of turbulent orographic drag and performance of NWP models had also been effectively improved [55–58]. This method believes that under neutral conditions of the atmosphere, when turbulent air flows through undulating orography, it still follows the logarithmic law within a certain vertical range. Numerical experiments [45, 59] and a series of observations [60–62] found and confirmed that above a certain altitude in the undulating orography, the wind profile approximately follows the logarithmic law.

Although the effective roughness method greatly improves the performance of NWP models, it also has some shortcomings. For example, it causes the effective roughness to be overestimated in the region where the orographic height varies greatly, resulting in greater surface stress and thus falsely low wind speeds near the ground. Given these shortcomings, Wood et al. [63] represented drag of turbulent orography by a well-defined stress profile. However, this scheme did not address the characterization of complex orographic areas involving multiple scales, which is crucial for large-scale NWP models. Based on Wood et al. [63], Beljaars et al. [64] developed a turbulent orographic drag parameterization scheme for large-scale models. To obtain the contributions of all scales of orography, it integrated over the orographic spectrum and it took the wind forcing layer as part of the orographic wavenumber spectrum integration to solve the convergence problem. This parameterization scheme made turbulent orographic drag parameterization a big step forward from the traditional effective roughness concept and was applied to the ECMWF. Xue et al. [65] compared the effective roughness method of turbulent orography with the direct parameterization method. It is found that the direct parameterization method could drag the wind on the vertical ridge and deflected the wind in the direction parallel to the ridge with a certain vertical attenuation thickness. The direct parameterization method treated turbulent orographic drag as a single item, which made the application and improvement of the scheme extremely convenient, and the physical meaning was clearer.

Richter et al. [66] and Lindvall et al. [67] also added turbulent orographic form drag parameterization into the Community Atmosphere Model (CAM5). CAM5 cut off all turbulence at high stabilities and instead used a strong orographic surface stress parameterization, which was referred to here as turbulent mountain stress (TMS). TMS increased the surface stress based on the effective roughness length method. It was only used for the atmospheric part and not the land model where the vegetation roughness length was used instead. TMS was mostly good for the large-scale circulation because it can improve sea level pressure, zonal wind speeds, and zonal anomalies of the 500 hPa stream function, but its beneficial effects on boundary layer flow were not always obvious [68]. The TMS surface stress τ is calculated as

$$\tau = \rho C_d |V| V, \tag{1}$$

where ρ and V are the air density and the wind vector at the lowest model level and C_d is a drag coefficient given by

$$C_d = \frac{f(R_i) k^2}{\ln^2 [(z + z_0)/z_0]}, \tag{2}$$

where R_i is the Richardson number and $f(R_i)$ is the function of it, as follows:

$$\begin{aligned} f(R_i) &= 1 \text{ if } R_i < 0, \\ f(R_i) &= 0 \text{ if } R_i > 1, \\ f(R_i) &= 1 - R_i \text{ if } 0 < R_i < 0, \end{aligned} \tag{3}$$

where $k = 0.4$ is the Von Kàrmàn constant, z is the altitude of the model mean orography, and z_0 is an effective roughness length, representing the idealized size of the perturbing (turbulent-eddies-generating) surface elements due to the unresolved orography. In fact,

$$Z_0 = \min(\text{tms\_z0fac} * \sigma, 100\,\text{m}), \tag{4}$$

where σ is the standard deviation of unresolved orography (measured in meters) on scales smaller than 6 km and assuming that the maximum vertical extent of the unresolved orographic roughness elements is order of 100 m. tms_z0fac is a numerical parameter affecting the minimum roughness length seen by the model, and its value is generally 0.075.

Under the background of increasing model horizontal resolution, Davoli et al. [53] believe that it is necessary to retune some physical parameters of the atmospheric model to reduce model bias. After repeated tuning, they tuned the parameter value of tms_z0fac in formula (4) from 0.075 to 0.1875. The results show a significant improvement compared to before the adjustment, especially in the European atmospheric circulation in winter. However, this work painted an only partial picture of the effects of such a partial model physics retuning effort and therefore suffered from a number of shortcomings and limitations. In order to more accurately represent the orographic drag effect, it is necessary to carry out a large number of NWP experiments and perform fine-scale simulations of different complex orographic areas to calibrate parameters in NWP models.

4.2. Orographic Gravity Wave Drag (OGWD). The study of orographic waves began a long time ago, and the development of mathematical theories has explained many aspects of the generation and evolution of orographic waves [69]. These works have contributed to the development of parameterization scheme for orographic gravity wave drag. When a stably stratified flow crosses a mountain, the subgrid orography may excite orographic gravity waves, and these can transmit horizontal momentum to areas where fluctuations are absorbed or dissipated. The dissipation of this fluctuating flux is called orographic gravity wave drag. The gravity wave drag can affect not only high-altitude winds, but also clouds and precipitation. It plays a very important role in maintaining the conservation of atmospheric circulation energy [70]. In the 1970s and 1980s, NWP systems could only resolve Rossby waves and some midlatitude cyclones. With improvements in the spatial resolution, the predicted motion became too strong, and later scholars found that the predicted wind speed deviation was primarily due to the lack of a clear simulation of the subgrid gravity wave drag [71–73]. In 1984, Boer et al. [74] considered the subgrid orographic gravity wave drag in the Canadian Climate Center atmospheric general circulation model. They introduced the climatology of this model and compared it with the observations. In atmosphere climatology, they found that the model was generally successful in reproducing the mean observations, such as the tropospheric circulation. In 1986, based on Lindzen's saturation hypothesis theory [72], Palmer et al. [75] developed a gravity wave drag parametrization scheme. This scheme primarily considered the effect of wave fragmentation in the low-level stratosphere on the gravity wave drag. The results showed that the problem of a strong westerly jet in the troposphere was reduced by the use of the parametrization scheme. In 1987, Mcfarlane [70] added the parametrization scheme of the gravity wave drag to the climate model and found that the momentum sank due to the breaking of gravity waves that were excited by orography and played a decisive role in the structure of the flow between the troposphere and the lower stratosphere. So far, the first-generation OGWD parameterization methods for the large-scale NWP models with relatively low model tops were developed had been basically formed. Shortly thereafter, Wu [76] explained the orographic gravity wave drag parametrization systematically, further enhancing people's understanding of orographic drag. These schemes reduced the overall size of jets to separate the stratospheric jet from the tropospheric jet and produced a large easterly wind shear in the upper troposphere. They have a great influence on the stratospheric drag at mid-latitudes, directly affecting the jet in the stratospheric and indirectly affecting the westerly winds on the surface through the secondary circulation caused by stratospheric drag. This indirect effect can improve cold pole problems and decrease westerly bias.

During the same period, the NWP community conducted research on "severe downslope windstorms" found in the lower reaches of mountains, such as the Boulder storm in the lower Rocky Mountains [77–79]. However, there was some debate about the exact physical mechanism of this phenomenon, but most agreed that the orographic gravity wave drag associated with mountain storms may be excessive [78, 80, 81]. While these phenomena did not occur all the time, the drag generated each time may be greater than the drag created by breakup of stratospheric orographic wave. In the boundary layer, similar resonance breaking and drag may also be important [82]. Therefore, these processes may play a large role in the break-even of large-scale atmospheric momentum.

These studies promoted the continuous development of OGWD parameterization. There was an increasing need to increase low-level drag in the model. Some scholars have begun to express these orographic effects by enhancing OGWD in the lower troposphere [83]. Iwasaki et al. [84] studied "linearly trapped" nonhydrostatic waves in the lower reaches of mountains and parameterized its effect in a special way and found that improved prediction results. Kim and Arakawa [85] studied the influence of "nonlinear trapped" waves due to wave breaking in the lower troposphere. They systematically parameterized its effect to enhance low-level drag in lower reaches regions where nonlinearities are strong, but not in weak nonlinear regions. Later, this parameterization scheme was introduced into NWP models and improved the performance of models [81]. This way of enhancing low-level drag separates the lower reaches' wave breaking zone from the upstream blocking zone. They are respectively related to the strength and weakness of the vertical divergence of the horizontal momentum flux. In 1997, Lott and Miller [86] proposed a new OGWD parametrization scheme to develop and improve these and other low-level drag and orographic specifications. This parametrization scheme could deal explicitly with the low-level flow that was "blocked" when height of the subgrid scale orography was sufficiently high. The prediction results of the new subgrid scale orographic gravity wave drag parametrization scheme were closer to actual observations. Soon after, this orographic gravity drag scheme was applied to ECMWF. The basic principles of the orographic gravity wave drag scheme are as follows:

$$H_n = \frac{NH}{|V|}, \tag{5}$$

where H_n is the dimensionless height of the mountain. N, H, and V are the Brunt–Väisälä frequency, maximum height of the obstacle, and velocity. When H_n is small, all airflow currents can climb over mountains and gravity wave is excited by vertical movement of airflow. Assuming that the mountain is oval, the surface stress generated by the gravity wave is

$$\tau_w = \rho_0 bGB(\gamma)NUH^2, \tag{6}$$

where ρ_0, b, and G are low-level density, tuning coefficient, and mountain shape function. $B(\gamma)$ is the function of mountain anisotropy. When H_n is large, vertical movement is restricted. Part of the low-level airflow will be blocked or form a bypass.

$$Z_b = H\frac{(H_n - H_{nc})}{H_n}, \tag{7}$$

where H_{nc} is a critical value. Z_b is the height of airflow can climb over the mountain. Airflow below this height will bypass this mountain. At this time, all drag is

$$\tau \approx \tau_w \left(1 + \frac{\pi C_d}{2GB(\gamma)} \frac{H_n - H_{nc}}{H_n^2}\right), \quad (8)$$

where C_d is the drag coefficient.

In 2003, Webster et al. [46] improved orographic representation in the UM and used a new orographic gravity wave drag scheme based on [86]. They considered the friction and rotation of the airflow in the new scheme and divided the total drag into two parts: the blocking flow and the gravity wave drag. The results showed that the introduction of the new scheme obviously improved the prediction results for the northern hemisphere and tropical regions. Gao and Ran [87] made improvements to Mcfarlane's scheme [70] that did not consider the problem of the gravity wave breaking and obtained a more complete parametrization scheme that described the drag impact of stationary gravity wave breaking on the zonal mean atmospheric circulation. This scheme not only considered the drag effect of the remaining momentum on zonal mean atmospheric circulation after the gravity wave is broken, but also considered the impact of momentum loss caused by the dissipation of the broken gravity wave on the zonal mean atmospheric circulation. In 2007, Andrew [88] modified orographic gravity drag scheme based on [86] and considered the blocked flow drag. He modified the subgrid orography height to the effective orographic height, which is the maximum height that the blocked layer depth can reach minus the blocking layer height. That is, modify H in formula (6) to H_{eff}.

$$H_{eff} = 3\mu - Z_b, \quad (9)$$

where μ is the standard deviation of the subgrid orographic height. Finally, the modified scheme was evaluated, and it was found that when calculating the gravity wave drag, it could reduce the excessive deceleration of motion in areas with complex orography.

Since then, orographic gravity wave drags parametrization schemes had been applied to various numerical models, and predictive capabilities of various NWP models have been improved and optimized. For example, Xu et al. [89] introduced the OGWD parametrization scheme of ECMWF based on [86] into the GRAPES model, filling the gap in the description of this type of physical processes in the GRAPES global medium-term numerical prediction system. The results indicated that with the introduction of the OGWD process, the distribution of the predicted fields was closer to that of the real atmosphere. Liu et al. [90] studied the occurrence mechanism of heavy rain in southern China by WRF model with the OGWD parametrization scheme based on Kim and Arakawa [85]; it was found that the parametrization scheme could predict the central position and the intensity of the heavy rain well. In addition, it was found that the gravity wave could strengthen the vertical upward motion. In 2017, Wang and Xi [91] introduced the OGWD scheme of the WRF model in the GRAPES-MESO model (GRAPES-MESO is the regional system version of GRAPES) and combined with the low-level airflow blocking parametrization proposed by Lott and Miller [86]. They divided the subgrid orographic drag into the OGWD and blocking drag to study the distribution of OGWD in the Qinghai-Tibet Plateau. Finally, it was found that the model had a more accurate description for low-level and high-level orographic gravity wave breaking.

The convoluted interaction between different processes related to orography is a difficult problem in NWP [21]. However, in recent years, there are few studies on the interaction between resolved orographic drag and parameterized orographic drag. Vosper et al. [92] described the resolved and unresolved orographic drag by predicting the flow of South Georgia and New Zealand Island. They found that the parametrized orographic drags increased when the model grid length decreased. When the characteristic island wavelength was about eight grid lengths, the resolved and parametrized orographic drag were approximately the same size. When wavelengths were shorter than 8–10 grid lengths, the parametrized orographic drag was very large. However, when the island scale changes, the resolved part of the orographic drag and the parameterized part of the orographic drag cannot be completely balanced. Van Niekerk et al. [93] studied the resolved and parametrized orographic drag in eleven different modes from eight major operational modeling centers, such as ECMWF's Integrated Forecasting System (IFS), Met Office's UM model, and Global Spectral Model 1705 (GSM1705) of Japan Meteorological Agency (JMA). They found that the parametrized gravity wave drag in most of NWP models was underestimated to varying degrees. Hence, the parametrized orographic drag introduced was slightly larger, and this may improve the results of the NWP prediction. Some studies have also found that the resolved orographic drag changes were not precisely balanced by the parameterized orographic drag changes in the numerical models [1, 92, 94, 95], so it cannot ensure that NWP models remain robust between different resolutions. This reveals that there are still some problems in the handling of orographic drag in NWP models, and more researches are needed to solve the division of orographic drag in the model dynamics and physical parameterization and division between different physical parameterization schemes.

5. Conclusion and Discussion

This paper reviewed recent developments from several aspects, including the influences of orography on weather, the influence of orographic representation on prediction accuracy, and the parametrization of orography-related drag in NWP models. The primary conclusions are shown as follows:

(1) Sensitivity analysis tests were used to study the influence of orography on weather. It was found that orography has a great influence on different scale systems and meteorological elements, such as near-surface wind, temperature, rainfall and heavy rain

systems, long-term droughts, mesoscale wind fields, tropical cyclones, and so on.

(2) In general, the higher the resolution of the orographic data in NWP models, the more accurate the model forecast results, and this is primarily reflected in elements such as precipitation and wind. In addition, it is important to process the original orographic dataset prior to application, including performing filtering, smoothing, and other schemes, to make prediction results nearer to the actual weather, and to ensure the accuracy of the NWP model prediction.

(3) The introduction of the orographic drag parameterization scheme greatly improves the prediction performance of NWP models. However, the intricate interaction between different parameterization schemes and between parameterization and resolved orographic drag also bring uncertainty to the numerical model, so lots of researches are still needed.

Finding an appropriate resolution, suitable orographic data, and the optimal orographic processing scheme to obtain a better orography representation requires great many numerical experiments, and the amount of calculation is very high. Hence, we must select a model with high accuracy and good stability. Because today's computers do not have enough computing power to deal with small enough space and time resolution problems, the parametrization of the subgrid scale orographic drag in NWP models will be necessary. However, parametrization relies heavily on simplified assumptions that are primarily based on linear theory and ideal peaks, and it does not describe the nonlinear effects imposed on complex orography well. As a result, parametrization becomes a source of uncertainty and deviations. How numerical models are designed to cross areas where models cannot identify to reduce or eliminate these uncertainties and deviations is critical for applications of NWP, wind resource prediction, and numerical model modeling in complex orography [40]. With the improvement of computer performance, the NWP model resolution is getting finer and finer. Can the NWP model dynamics completely resolve orographic drag and eliminate the parameterization schemes? This is an open topic and there is no definite answer. In 2006, Smith et al. [96] utilized seven examples to explore the sensitivity of the horizontal resolution of numerical model to OGWD. The result indicated that in most cases, even if the horizontal resolution were raised to finer than 4 km, the impact of the gravity wave drag in the model still could not be fully resolved. Kim et al. [97] predicted the model resolution needed to eliminate gravity wave drag parametrization and found that the horizontal resolution required to achieve this goal was still much higher than the highest resolution achieved up to now. Probably in the recent period, parameterized schemes are still mainly used to represent effect of unresolved orographic drag in NWP models. However, with the rapid development of artificial intelligence, machine learning algorithms that are automatically improved through data learning and do not require explicit programming provide great opportunities for NWP. There are already some scholars doing this work. For example, Matsuoka et al. [98] proposed a deep learning method to predict the gravity wave drag. After training and testing, the model produced better estimates of the fine-scale momentum flux distribution of the gravity waves. It can be seen that in future research, there is great potential to use the parameterization schemes based on machine learning algorithms to couple into a higher-precision NWP model to extract key features of the data with higher efficiency and make accurate predictions.

Conflicts of Interest

The authors declare that there are no conflicts of interest regarding the publication of this paper.

Acknowledgments

This research was funded by the National Natural Science Foundation of China (Grant no. 41875121).

References

[1] I. Sandu, A. V. Niekerk, T. G. Shepherd, S. B. Vosper, and G. Svensson, "Impacts of orography on large-scale atmospheric circulation," *Climate Atmospheric Science*, vol. 2, no. 10, pp. 1–8, 2019.

[2] J. Berckmans, T. Woollings, M.-E. Demory, P.-L. Vidale, and M. Roberts, "Atmospheric blocking in a high resolution climate model: influences of mean state, orography and eddy forcing," *Atmospheric Science Letters*, vol. 14, no. 1, pp. 34–40, 2013.

[3] A. S. Moya-Álvarez, D. Martínez-Castro, S. Kumar, R. Estevan, and Y. Silva, "Response of the WRF model to different resolutions in the rainfall forecast over the complex Peruvian orography," *Theoretical and Applied Climatology*, vol. 137, no. 3, pp. 2993–3007, 2019.

[4] S. M. Kirthiga and N. R. Patel, "Impact of updating land surface data on micrometeorological weather simulations from the WRF model," *Atmósfera*, vol. 31, no. 2, 2018.

[5] M. T. Caccamo, G. Castorina, F. Colombo, V. Insinga, E. Maiorana, and S. Magazù, "Weather forecast performances for complex orographic areas: impact of different grid resolutions and of geographic data on heavy rainfall event simulations in Sicily," *Atmospheric Research*, vol. 198, pp. 22–33, 2017.

[6] C. F. Mass, D. Ovens, K. Westrick, and B. A. Colle, "Does increasing horizontal resolution produce more skillful forecasts?" *Bulletin of the American Meteorological Society*, vol. 83, no. 3, pp. 407–430, 2002.

[7] P. Alpert, F. Jin, and H. Shafir, "Orographic precipitation simulated by a super-high resolution global climate model over the Middle East," *National Security and Human Health Implications of Climate Change*, vol. 125, pp. 301–306, 2012.

[8] L. Berkofsky and E. A. Bertoni, "Mean topographic charts for the entire earth," *Bulletin of the American Meteorological Society*, vol. 36, no. 7, pp. 350–354, 1955.

[9] K. G. Nikolakopoulos, "Comparing a DTM created with ASTER data to GTOPO 30 and to one created from 1/50.000 topographic maps," *Proceedings of SPIE*, vol. 5574, no. 1, pp. 43–51, 2004.

[10] T. G. Farr, "The Shuttle radar topography mission," *Review of Geophysics*, vol. 45, no. 2, 2007.
[11] T. Tachikawa, *ASTER Global Digital Elevation Model Version 2–Summary of Validation Results*, NASA, Washington, DC, USA, 2011.
[12] X. Zhang and Y. Yin, "Evaluation of the four PBL schemes in WRF Model over complex topographic areas," *Transactions of Atmospheric Sciences*, vol. 36, no. 1, pp. 68–76, 2013.
[13] A. De Meij and J. F. Vinuesa, "Impact of SRTM and Corine Land Cover data on meteorological parameters using WRF," *Atmospheric Research*, vol. 143, pp. 351–370, 2014.
[14] A. De Meij, E. Bossioli, C. Penard, J. F. Vinuesa, and I. Price, "The effect of SRTM and Corine Land Cover data on calculated gas and PM10 concentrations in WRF-Chem," *Atmospheric Environment*, vol. 101, pp. 177–193, 2015.
[15] X. Wen, W. Dong, W. Yuan, and Z. Zheng, "Establishment and analysis of a high-resolution assimilation dataset of the water-energy cycle in China," *Physics and Chemistry of the Earth, Parts A/B/C*, vol. 87, pp. 126–141, 2015.
[16] W. Liu, Y. Gao, Y. Ran, and g. Cheng, "Contrast analyses of simulation results in Heihe basin utilizing the different resolution DEM data," *Plateau Meteorology*, vol. 26, no. 3, pp. 525–531, 2007.
[17] C. G. Nunalee and Á. Horváth, "High-resolution numerical modeling of mesoscale island wakes and sensitivity to static topographic relief data," *Geoscientific Model Development*, vol. 8, no. 8, pp. 2973–2990, 2015.
[18] J. J. He, Y. Yu, L. J. Yu, N. Liu, and S. P. Zhao, "Impacts of uncertainty in land surface information on simulated surface temperature and precipitation over China," *International Journal of Climatology*, vol. 37, pp. 829–847, 2017.
[19] R. Salerno and C. Balsamo, "Influence of nonhydrostatic effects and time-integration schemes on numerical simulations in a complex orography environment," *MeteoSwiss*, vol. 66, pp. 230–233, 2003.
[20] A. P. Dimri, "Impact of horizontal model resolution and orography on the simulation of a western disturbance and its associated precipitation," *Meteorological Applications*, vol. 11, no. 2, pp. 115–127, 2004.
[21] G. H. Roe, "Orographic precipitation," *Annual Review of Earth and Planetary Sciences*, vol. 33, no. 1, pp. 645–671, 2005.
[22] C. Oikonomou, H. A. Flocas, G. Katavoutas, M. Hatzaki, D. N. Asimakopoulos, and C. Zerefos, "On the relationship of orography with extreme dry spells in Greece," *Advances in Geosciences*, vol. 25, pp. 161–166, 2010.
[23] J. Sethunadh, A. Jayakumar, S. Mohandas, E. Rajagopal, and A. Nagulu, "Impact of Cartosat-1 orography on weather prediction in a high-resolution NCMRWF unified model," *Journal of Earth System Science*, vol. 128, 2019.
[24] C. Torma and F. Giorgi, "On the evidence of orographical modulation of regional fine scale precipitation change signals: the Carpathians," *Atmospheric Science Letters*, vol. 21, no. 6, Article ID e967, 2020.
[25] M. Kunz and C. Kottmeier, "Orographic enhancement of precipitation over low mountain ranges. Part I: model formulation and idealized simulations," *Journal of Applied Meteorology and Climatology*, vol. 45, no. 8, pp. 1025–1040, 2006.
[26] W. C. Chao, "Correction of excessive precipitation over steep and high mountains in a GCM," *Journal of the Atmospheric Sciences*, vol. 69, no. 5, pp. 1547–1561, 2012.
[27] F. Kong, "Spatiotemporal patterns of global-continental-regional scale heavy rainfall," *Journal of Beijing Normal University*, vol. 52, no. 2, pp. 228–234, 2016.
[28] C. Tao, *Heavy Rain in China*, China Science Publishing & Media Ltd., Beijing, China, 1980.
[29] R. Rotunno and R. A. Houze, "Lessons on orographic precipitation from the Mesoscale Alpine Programme," *Quarterly Journal of the Royal Meteorological Society*, vol. 133, no. 625, pp. 811–830, 2007.
[30] P. Bougeault, P. Binder, A. Buzzi et al., "The map special observing period," *Bulletin of the American Meteorological Society*, vol. 82, no. 3, pp. 433–462, 2001.
[31] H. Volkert and T. Gutermann, "Inter-domain cooperation for mesoscale atmospheric laboratories: the Mesoscale Alpine Programme as a rich study case," *Quarterly Journal of the Royal Meteorological Society*, vol. 133, no. 625, pp. 949–967, 2007.
[32] Z. Xia, Y. Hui, W. Xinmin, S. Lin, W. Di, and L. Han, "Analysis on characteristic and abnormality of atmospheric circulations of the July 2021 extreme precipitation in Henan," *Transactions of Atmospheric Sciences*, vol. 44, no. 5, pp. 672–687, 2021.
[33] L. Renault, A. Hall, and J. C. McWilliams, "Orographic shaping of US West Coast wind profiles during the upwelling season," *Climate Dynamics*, vol. 46, no. 1, pp. 273–289, 2016.
[34] A. Obermann-Hellhund and B. Ahrens, "Mistral and tramontane simulations with changing resolution of orography," *Atmospheric Science Letters*, vol. 19, no. 9, Article ID e848, 2018.
[35] K.-C. Huang and C.-C. Wu, "The impact of idealized terrain on upstream tropical cyclone track," *Journal of the Atmospheric Sciences*, vol. 75, no. 11, pp. 3887–3910, 2018.
[36] M. S. Yudin, "A numerical study of gravity waves in the atmosphere: smooth and steep orography effects," *IOP Conference Series: Earth and Environmental Science*, vol. 48, no. 1, Article ID 012024, 2016.
[37] W. A. Gallus, "The impact of step orography on flow in the Eta model: two contrasting examples," *Weather and Forecasting*, vol. 15, no. 5, pp. 630–639, 2000.
[38] X. Shen, J. Wang, Z. Li, D. Chen, and J. Gong, "Research and operational development of numerical weather prediction in China," *Journal of Meteorological Research*, vol. 34, no. 4, 2020.
[39] B. Goger, M. W. Rotach, A. Gohm, I. Stiperski, and O. Fuhrer, "Current challenges for numerical weather prediction in complex terrain: topography representation and parameterizations," *International Conference on High Performance Computing & Simulation*, pp. 890–894, 2016.
[40] F. Chow, C. Schär, N. Ban, K. Lundquist, L. Schlemmer, and X. Shi, "Crossing multiple gray zones in the transition from mesoscale to microscale simulation over complex terrain," *Atmosphere*, vol. 10, no. 5, p. 274, 2019.
[41] X. Gao, Y. Xu, Z. Zhao, S. P. Jeremy, and G. Filippo, "Impacts of horizontal resolution and topography on the numerical simulation of East asian precipitation," *Transactions of Atmospheric Sciences*, vol. 30, no. 2, pp. 185–192, 2006.
[42] W. Zhu, Z. Chen, Y. Zhang, J. Yang, and Y. Zhang, "The impact of high resolution terrain on the prediction of ground elements from grapes model in south China," *Journal of Tropical Meteorology*, vol. 35, no. 6, pp. 801–811, 2019.
[43] L. A. Davies and A. R. Brown, "Assessment of which scales of orography can be credibly resolved in a numerical model," *Quarterly Journal of the Royal Meteorological Society*, vol. 127, no. 574, pp. 1225–1237, 2001.
[44] S. E. Belcher and N. Wood, "Form and wave drag due to stably stratified turbulent flow over low ridges," *Quarterly Journal of*

the Royal Meteorological Society, vol. 122, no. 532, pp. 863–902, 1996.

[45] N. Wood and P. Mason, "The Pressure force induced by neutral, turbulent flow over hills," *Quarterly Journal of the Royal Meteorological Society*, vol. 119, no. 514, pp. 1233–1267, 1993.

[46] S. Webster, A. R. Brown, D. R. Cameron, and C. P.Jones, "Improvements to the representation of orography in the Met Office unified model," *Quarterly Journal of the Royal Meteorological Society*, vol. 129, no. 591, pp. 1989–2010, 2003.

[47] W. H. Raymond, "High-order low-pass implicit tangent filters for use in finite area calculations," *Monthly Weather Review*, vol. 116, no. 11, pp. 2132–2141, 1988.

[48] I. C. Rutt, J. Thuburn, and A. Staniforth, "A variational method for orographic filtering in NWP and climate models," *Quarterly Journal of the Royal Meteorological Society*, vol. 132, no. 619, pp. 1795–1813, 2007.

[49] N. Tu, J. Chen, and G. He, "Research on application of Chebyshev polynomial filtering method in smooth topography of GRAPES mode," *Plateau Meteorology*, vol. 31, no. 1, pp. 47–56, 2012.

[50] G. He, J. Peng, and N. Tu, "Terrain construction and experiment for numerical model based on high resolution terrain data," *Plateau Meteorology*, vol. 34, no. 4, pp. 910–922, 2015.

[51] L. Chen, Y. Xia, and X. Zhuang, "Influence of different terrain smoothing schemes in WRF model on precipitation forecast," *Meteorol Sci Technol*, vol. 48, no. 5, pp. 664–674, 2020.

[52] ECMWF, *Proceedings of a Workshop on Orography*, ECMWF, UK, 1997.

[53] G. Davoli, "Tuning of some orography-related drag parameterizations in the atmospheric component of the cmcc operational seasonal prediction systems," *Technical Notes*, 2021.

[54] F. Fiedler and H. A. Panofsky, "The geostrophic drag coefficient and the "effective" roughness length," *Quarterly Journal of the Royal Meteorological Society*, vol. 98, no. 415, pp. 213–220, 1972.

[55] P. Mason, "On the parameterization of orographic drag," in *Seminar on Physical Parameterization for Numerical Models of the Atmosphere,* ECMWF, UK, 1985.

[56] P. A. Taylor, R. I. Sykes, and P. J. Mason, "On the parameterization of drag over small-scale topography in neutrally-stratified boundary-layer flow," *Boundary-Layer Meteorology*, vol. 48, no. 4, pp. 409–422, 1989.

[57] A. L. M. Grant and P. J. Mason, "Observations of boundary-layer structure over complex terrain," *Quarterly Journal of the Royal Meteorological Society*, vol. 116, no. 491, pp. 159–186, 1990.

[58] S. F. Milton and C. A. Wilson, "The impact of parameterized subgrid-scale orographic forcing on systematic errors in a global NWP model," *Monthly Weather Review*, vol. 124, no. 9, pp. 2023–2045, 1996.

[59] T. M. J. Newley, *Turbulent Air Flow over Hills*, University of Cambridge, Cambridge, UK, 1986.

[60] W. P. Kustas and W. Brutsaert, "Wind profile constants in a neutral atmospheric boundary layer over complex terrain," *Boundary-Layer Meteorology*, vol. 34, no. 1, pp. 35–54, 1986.

[61] R. S. Thompson, "Note on the aerodynamic roughness length for complex terrain," *Journal of Applied Meteorology*, vol. 17, no. 9, pp. 1402-1403, 1978.

[62] C. J. Nappo Jr, "Mesoscale flow over complex terrain during the eastern Tennessee trajectory experiment (ETTEX)," *Journal of Applied Meteorology*, vol. 16, no. 11, pp. 1186–1196, 1977.

[63] N. Wood, A. R. Brown, and F. E. Hewer, "Parametrizing the effects of orography on the boundary layer: an alternative to effective roughness lengths," *Quarterly Journal of the Royal Meteorological Society*, vol. 127, no. 573, pp. 759–777, 2001.

[64] A. C. M. Beljaars, A. R. Brown, and N. Wood, "A new parametrization of turbulent orographic form drag," *Quarterly Journal of the Royal Meteorological Society*, vol. 130, no. 599, pp. 1327–1347, 2004.

[65] H. Xue, X. Shen, and Y. Su, "Parameterization of turbulent orographic form drag and implementation in GRAPES," *Journal of Applied Meteorological Science*, vol. 22, no. 2, pp. 169–181, 2011.

[66] J. H. Richter, F. Sassi, and R. R. Garcia, "Toward a physically based gravity wave source parameterization in a general circulation model," *Journal of the Atmospheric Sciences*, vol. 67, no. 1, pp. 136–156, 2010.

[67] J. Lindvall, G. Svensson, and C. Hannay, "Evaluation of near-surface parameters in the two versions of the atmospheric model in CESM1 using flux station observations," *Journal of Climate*, vol. 26, no. 1, pp. 26–44, 2013.

[68] J. Lindvall, G. Svensson, and R. Caballero, "The impact of changes in parameterizations of surface drag and vertical diffusion on the large-scale circulation in the Community Atmosphere Model (CAM5)," *Climate Dynamics*, vol. 48, no. 11, pp. 3741–3758, 2017.

[69] R. B. Smith, "The influence of mountains on the atmosphere," *Advances in Geophysics*, vol. 21, pp. 87–230, 1979.

[70] N. A. Mcfarlane, "The effect of orographically excited gravity wave drag on the general circulation of the lower stratosphere and troposphere," *Journal of the Atmospheric Sciences*, vol. 44, no. 14, pp. 1775–1800, 1987.

[71] J. T. Houghton, "The stratosphere and mesosphere," *Quarterly Journal of the Royal Meteorological Society*, vol. 104, no. 439, pp. 1–29, 1978.

[72] R. S. Lindzen, "Turbulence and stress owing to gravity wave and tidal breakdown," *Journal of Geophysical Research Oceans*, vol. 86, no. 10, pp. 9707–9714, 1981.

[73] J. R. Holton, "The role of gravity wave induced drag and diffusion in the momentum budget of the mesosphere," *Journal of the Atmospheric Sciences*, vol. 39, no. 4, pp. 791–799, 1982.

[74] G. J. Boer, N. A. Mcfarlane, and R. Laprise, "The climatology of the Canadian Climate Centre general circulation model as obtained from a five-year simulation," *Atmosphere-Ocean*, vol. 22, no. 4, pp. 430–473, 1984.

[75] T. N. Palmer, G. J. Shutts, and R. Swinbank, "Alleviation of a systematic westerly bias in general circulation and numerical weather prediction models through an orographic gravity wave drag parametrization," *Quarterly Journal of the Royal Meteorological Society*, vol. 112, no. 474, pp. 1001–1039, 1986.

[76] Y. Wu, "The Parameterization of the Orographic gravity wave drag," *Meteorological Science and Technology*, vol. 4, pp. 31–33, 1987.

[77] J. B. Klemp and D. K. Lilly, "Numerical simulation of hydrostatic mountain waves," *Journal of the Atmospheric Sciences*, vol. 35, no. 1, pp. 78–107, 1978.

[78] W. R. Peltier and T. L. Clark, "The evolution and stability of finite-amplitude mountain waves. Part II: surface wave drag and severe downslope windstorms," *Journal of the Atmospheric Sciences*, vol. 36, no. 8, pp. 1498–1529, 1979.

[79] D. R. Durran and J. B. Klemp, "Another look at downslope winds. Part II: nonlinear amplification beneath wave-overturning layers," *Journal of the Atmospheric Sciences*, vol. 44, no. 22, pp. 3402–3412, 1987.

[80] J. T. Bacmeister and R. T. Pierrehumbert, "On high-drag States of nonlinear stratified flow over an obstacle," *Journal of the Atmospheric Sciences*, vol. 45, no. 1, pp. 63–80, 1988.

[81] Y.-J. Kim, "Representation of subgrid-scale orographic effects in a general circulation model. Part I: impact on the dynamics of simulated january climate," *Journal of Climate*, vol. 9, no. 11, pp. 2698–2717, 1996.

[82] C. J. Nappo and G. Chimonas, "Wave exchange between the ground surface and a boundary-layer critical level," *Journal of the Atmospheric Sciences*, vol. 49, no. 13, pp. 1075–1091, 1992.

[83] R. T. Pierrehumbert, "An essay on the parameterization of orographic gravity wave drag," *Seminar/Workshop on Observation, Theory and Modelling of Orographic effects*, vol. 1, 1986.

[84] T. Iwasaki, S. Yamada, and K. Tada, "A parameterization scheme of orographic gravity wave drag with two different vertical partitionings," *Journal of the Meteorological Society of Japan. Series II*, vol. 67, no. 1, pp. 11–27, 1989.

[85] Y. J. Kim and A. Arakawa, "Improvement of orographic gravity wave parameterization using a mesoscale gravity wave model," *Journal of the Atmospheric Sciences*, vol. 52, no. 52, pp. 1875–1902, 1995.

[86] F. Lott and M. J. Miller, "A new subgrid-scale orographic drag parametrization: its formulation and testing," *Quarterly Journal of the Royal Meteorological Society*, vol. 123, no. 537, pp. 101–127, 1997.

[87] S. Gao and L. Ran, "The Parameterized Scheme for the Dragging of gravity wave to mid-level zonal mean airflow," *Chinese Science Bulletin*, vol. 48, no. 7, pp. 726–729, 2003.

[88] O. Andrew, "Evaluation revised parameterizations sub-grid orographic drag," *Journal of Advances in Modeling Earth Systems*, 2007.

[89] G. Xu, X. Yang, L. Huang, D. Chen, X. Wu, and Z. Jin, "Introducing and application testing of the orographic gravity wave drag parameterization physics in the GRAPES," *Acta Meteorologica Sinica*, vol. 68, no. 5, pp. 631–639, 2010.

[90] L. Liu, Z. Ding, Y. Chang, and M. Chen, "Application of parameterization of orographic gravity wave drag in WRF model to mechanism analysis of a heavy rain in warm sector over south China," *Meteorological Science and Technology*, vol. 40, no. 2, pp. 232–240, 2012.

[91] Y. Wang and G. Xu, "Preliminary analysis of the gravity wave drag on Qinghai-Tibet Plateau and its numerical simulation," *Acta Meteorologica Sinica*, vol. 75, no. 2, pp. 275–287, 2017.

[92] S. B. Vosper, A. R. Brown, and S. Webster, "Orographic drag on islands in the NWP mountain grey zone," *Quarterly Journal of the Royal Meteorological Society*, vol. 142, no. 701, pp. 3128–3137, 2016.

[93] A. van Niekerk, I. Sandu, A. Zadra, E. Bazile, T. Kanehama, and M. Köhler, "COnstraining ORographic drag effects (COORDE): a model comparison of resolved and parametrized orographic drag," *Journal of Advances in Modeling Earth Systems*, vol. 12, no. 11, 2020.

[94] A. van Niekerk, T. G. Shepherd, S. B. Vosper, and S. Webster, "Sensitivity of resolved and parametrized surface drag to changes in resolution and parametrization," *Quarterly Journal of the Royal Meteorological Society*, vol. 142, no. 699, pp. 2300–2313, 2016.

[95] S. B. Vosper, A. Niekerk, A. Elvidge, I. Sandu, and A. Beljaars, "What can we learn about orographic drag parametrisation from high-resolution models? A case study over the Rocky Mountains," *Quarterly Journal of the Royal Meteorological Society*, vol. 146, no. 727, pp. 979–995, 2020.

[96] S. A. Smith, J. D. Doyle, A. R. Brown, and S. Webster, "Sensitivity of resolved mountain drag to model resolution for MAP case-studies," *Quarterly Journal of the Royal Meteorological Society*, vol. 132, no. 618, pp. 1467–1487, 2006.

[97] Y. J. Kim, S. D. Eckermann, and H. Y. Chun, "An overview of the past, present and future of gravity-wave drag parametrization for numerical climate and weather prediction models," *Atmosphere-Ocean*, vol. 41, no. 1, pp. 65–98, 2003.

[98] D. Matsuoka, S. Watanabe, K. Sato, S. Kawazoe, W. Yu, and S. Easterbrook, "Application of deep learning to estimate atmospheric gravity wave parameters in reanalysis data sets," *Geophysical Research Letters*, vol. 47, no. 19, 2020.

Hindawi
Advances in Meteorology
Volume 2022, Article ID 3792225, 17 pages
https://doi.org/10.1155/2022/3792225

Research Article

Observation Selection, Total Variation, and L-Curve Methods for LiDAR Data Denoising

Jie Zhang,[1] **Pak Wai Chan**,[2] **and Michael K. Ng**[1]

[1]*Department of Mathematics, The University of Hong Kong, Hong Kong, China*
[2]*Aviation Weather Services, Hong Kong Observatory, Hong Kong, China*

Correspondence should be addressed to Michael K. Ng; mng@maths.hku.hk

Received 6 October 2021; Accepted 27 December 2021; Published 22 January 2022

Academic Editor: Hiroyuki Hashiguchi

In this article, we propose a light detection and ranging (LiDAR) data denoising scheme for wind profile observation as a part of quality control procedure for wind velocity monitoring and windshear detection. The proposed denoising scheme consists of several components. (i) It selects LiDAR observations according to their SNR values so that serious noisy data can be removed. (ii) A polar-based total variation smoothing term is employed to regularize LiDAR observations. (iii) The regularization parameters are automatically determined to balance the data-fitting term and the total variation smoothing term. Numerical results for LiDAR data collected at the Hong Kong International Airport are reported to demonstrate that the denoising performance of the proposed method is better than that of the testing LiDAR data denoising schemes in the literature.

1. Introduction

Light detection and ranging (LiDAR) technique [1, 2] is a remote sensing tool that plays a significant role in environmental monitoring sciences. It is widely used in meteorological data observing. Generally, LiDAR emits a beam of light to the observation region. Some of this light would be backscattered towards the LiDAR receiver since it interacts with the medium or particles under observation [3]. The backscattered light captured by the LiDAR receiver is used to determine the characteristics of the observation area, e.g., the velocity of wind. Due to the impact of measurement environments and some other reasons, there would be some observation errors and very noisy observations in the observational LiDAR data as the range of observation increases [4]. It can have a serious effect in different LiDAR data applications such as windshear detection. Therefore, it is indispensable to develop an effective denoising method as a part of quality control for LiDAR observational data to improve the data quality and remove bad observations.

Several denoising methods have been developed to improve the quality of LiDAR data. There are mainly two different types of methods for LiDAR data denoising. One is for the time-varying but location-fixed LiDAR data. For example, a stationary wavelet domain spatial filtering-based denoising method was proposed by Yin et al. [5]. The method can effectively remove noise and detect the sudden change of LiDAR signal. Hassanpour [6, 7] proposed a singular value decomposition-based Savitzky-Golay approach for signal denoising. Similarly, Azadbakht et al. [8] employed the Savitzky-Golay method for full-waveform LiDAR data denoising. The second one is for the time-varying and distance-varying LiDAR data. For instance, Wu et al. [9] proposed a biorthogonal discrete wavelet transform (DWT) with a distance-dependent threshold algorithm to do the line-of-sight wind velocity denoising. In [10], Wu et al. studied the empirical mode decomposition (EMD) method [11] to analyze LiDAR data. Liu et al. applied the EMD method to a Doppler wind LiDAR acquisition system and got much better denoising results than the original method in [12]. In [13], Zhang et al. combined the EMD method with the Savitzky-Golay filtering algorithm, which can retain more features of LiDAR signal. Li et al. proposed a LiDAR denoising method based on ensemble empirical mode decomposition in [14]. This method can overcome the

mode mixing phenomenon that occurs with the EMD method. Also Tian et al. improved the EMD method for range and frequency analysis in LiDAR data and proposed an automatic EMD denoising method in [15]. In [16], the EMD-CIIT method [17] was applied to reduce the noise of large-scale LiDAR data.

However, the abovementioned methods cannot remove the bad observations in LiDAR data. To address this issue, several methods including bad data removal were used in the LiDAR data applications. The most commonly used methods are based on the signal-to-noise ratio (SNR). For example, Baranov et al. [18] filtered the bad observations in LiDAR data by the threshold level of SNR and then applied a smoothing algorithm to improve the data quality. In [19], Newsom et al. removed the bad observations based on an SNR threshold level. The Hong Kong Observatory (HKO) currently used a SNR-based quality control method to preprocess the LiDAR data collected at the Hong Kong International Airport (HKIA) for windshear detection (refer to Algorithm 3 for more detailed description). However, the SNR threshold level the above methods used is really empirical that requires numerous tests based on the observational data. Moreover, we remark that all the abovementioned methods do not consider LiDAR data at the other azimuth angles together in the data processing procedure.

In this article, we aim to investigate a mathematical denoising scheme that can not only reduce the noise level for a whole scan but also remove the bad observations in LiDAR data adaptively based on the corresponding SNR values. By analysis of the LiDAR data collected at the Hong Kong International Airport (see Section 2 for more details), we propose a LiDAR data denoising method based on the minimization of an objective function containing (i) the data-fitting term between the observed LiDAR data and the denoised data; (ii) the polar-based total variation regularization term that is used to smooth LiDAR observations; and (iii) the weighting term of LiDAR observations that is employed to control whether LiDAR observations are used in the denoising procedure based on their SNR values and neighborhood observations. In the optimization scheme, we also propose an L-curve selection method for several regularization parameters to be used for balancing the contribution of the above three terms in the objective function. The whole scan data are used in the proposed scheme by the polar total variation method instead of the only data at the same azimuth angle used by the other methods given in [9, 16, 18, 19]. The SNR-based weighting term makes it possible to remove the very bad observations more flexibly instead of just relying on a fixed empirical threshold. Numerical results demonstrate the usefulness of the proposed denoising scheme compared with testing LiDAR data denoising schemes in the literature.

This paper is organized as follows. In Section 2, we introduce our proposed denoising scheme and the parameter selection method. In Section 3, results and discussions are presented. Finally, some concluding remarks are given in Section 4.

2. Methods

In this section, the information about LiDAR data we investigate in this paper is given in Subsection 2.1. Next, we introduce the proposed model in Subsection 2.2. Also, the algorithm and parameter selection method are given in Subsections 2.3 and 2.4, respectively.

2.1. Data Sets. The Hong Kong International Airport (HKIA) is located at the place lying to the north of Lantau Island that is quite mountainous with heights ranging from 300 m to 900 m. Due to the complex terrain near the airport, it is necessary to collect LiDAR data of wind velocities and observe any windshear phenomena appearing over the flight paths of the airport. To provide timely windshear alerting, the Hong Kong Observatory devised a Doppler LiDAR system (see [20, 21] for more details). Due to the highly cluttered environment around HKIA such as vehicles, derricks, barges, windmills, and cable cars, there are lots of noise and bad observations in the observational LiDAR data. For example, we show in Figure 1(a) the LiDAR radial velocity data of conical scan, where the radius and the polar angle of the scan refer to the slant range and the azimuth angle of LiDAR beam, respectively. In Figure 1(b), we show the signal-to-noise ratio (SNR) of the measured wind velocities corresponding to Figure 1(a). It is obvious that there are noise and some outliers whose SNR values are from −10 to −60 in the observational data. Therefore, it is significant to develop an efficient data denoising method to remove bad observations and improve the quality of observational LiDAR data.

The set of data used in this study was collected at HKIA from 1 March to 31 March 2015, including the 147 windshear cases that reported in the pilot report and several nonwindshear cases. Each scan of windshear cases took $\mathbf{y}_i \in \mathbb{R}^n$ about 25 seconds (see one example in Figure 1).

2.2. The Proposed Model. Let be the LiDAR data observed at azimuth angle θ_i. For simplicity, we assume that there are m azimuth angles $(\theta_1 < \theta_2 < \cdots < \theta_m)$ to be recorded in between 0° and 359°, and also there are n range values to be recorded, i.e.,

$$y_i = \left[y_{i,1}, y_{i,2}, \ldots, y_{i,n}\right], \quad 1 \le i \le m. \tag{1}$$

Note that the locations of such range values are not necessary to be uniform, and the distance between the LiDAR centre and the observed value $y_{i,j}$ is equal to r_j. We are interested to compute the denoising LiDAR data as follows:

$$x_i = \left[x_{i,1}, x_{i,2}, \ldots, x_{i,n}\right], \quad 1 \le i \le m, \tag{2}$$

according to the given SNR values:

$$s_i = \left[s_{i,1}, s_{i,2}, \ldots, s_{i,n}\right], \quad 1 \le i \le m, \tag{3}$$

from the observed LiDAR data. When $y_{i,j}$ is a missing LiDAR observation, the corresponding $s_{i,j}$ can be set to be $-\infty$. In total, there are nm observations and SNR values and nm unknowns covered in the conical scan in a two-dimensional plane. In the proposed minimization model, there are three components in the objective function.

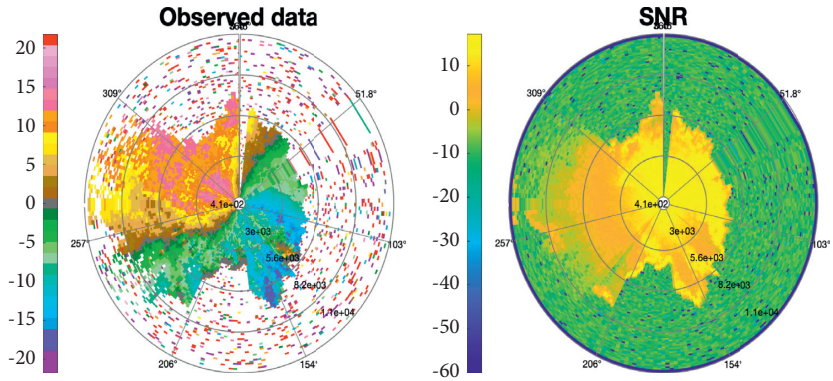

(a) (b)

Figure 1: An example of the LiDAR data on 5 March 2015 from 04 : 16 : 02 to 04 : 16 : 25. (a) Wind velocities and (b) signal-to-noise ratio of LiDAR observations. The observations were collected at the Hong Kong International Airport under LiDAR system by Hong Kong Observatory [21, 22].

(i) The first term is the data-fitting term between the observed LiDAR data $\mathbf{y}_i$ and the denoised data $\mathbf{x}_i$ $(1 \le i \le m)$. In order to determine whether $y_{i,j}$ at the azimuth angle θ_i and range value r_j to be used in the model, we incorporate a nonnegative weight $w_{i,j}$ for $y_{i,j}$. When the value of $w_{i,j}$ is equal to zero, the LiDAR observation $y_{i,j}$ is not used. The resulting data-fitting term is given by

$$\frac{1}{2}\sum_{i=1}^{m}\sum_{j=1}^{n} w_{i,j}\left(y_{i,j}-x_{i,j}\right)^2. \tag{4}$$

It is clear that when the LiDAR data observation is removed $(w_{i,j} = 0)$, the corresponding data-fitting term does not appear.

(ii) In the model, we would like to smooth LiDAR observations over all possible range and azimuth values together. In image processing, total variation regularization techniques based on rectangular pixel-based form were shown to be a very useful denoising method (see, for instance, [23–25]). Here, the polar-based total variation regularization term is proposed and employed as follows:

$$\mathrm{TV}\left(x_{i,j}\right) = \frac{\left|x_{i,j}-x_{i,j-1}\right|}{d\left(x_{i,j},x_{i,j-1}\right)} + \frac{\left|x_{i,j}-x_{i-1,j}\right|}{d\left(x_{i,j},x_{i-1,j}\right)}, \tag{5}$$

where $d(x_{i,j}, x_{i,j-1})$ refers to the distance between the two observed range values at the same azimuth angle, i.e.,

$$d\left(x_{i,j},x_{i,j-1}\right) = r_j - r_{j-1}, \tag{6}$$

and $d(x_{i,j}, x_{i,j-1})$ refers to the distance between the same observed range value at the two adjacent azimuth angles θ_i and θ_{i-1}, i.e.,

$$d\left(x_{i,j},x_{i-1,j}\right) = \left|2r_j \sin\left(\frac{\theta_i-\theta_{i-1}}{2}\right)\right|. \tag{7}$$

In (7), the first and the second terms are the one-dimensional total variation regularization. However, we apply the one-dimensional total variation regularization to the polar-based LiDAR data observations by using their actual distances in the formula. The combined total variation regularization term is given as follows:

$$\sum_{i=1}^{m}\sum_{j=1}^{n} w_{i,j}\mathrm{TV}\left(x_{i,j}\right). \tag{8}$$

We see from (7) and (8) that the denoised values $x_{i,j}$ are coupled into the regularization formula, and therefore the denoising procedure is adapted to the whole polar-based LiDAR data observations instead of observations in range values only such as the methods we introduce in Section 1.

(ii) In the model, we should include SNR values $s_{i,j}$ to determine whether the LiDAR observation $y_{i,j}$ is used in the denoising procedure. Here, we propose the following term in the model:

$$\lambda_1 \sum_{i=1}^{m}\sum_{j=1}^{n} \exp\left(-s_{i,j}\right)w_{i,j}^2 + \lambda_2 \sum_{i=1}^{m}\sum_{j=1}^{n} \exp\left(s_{i,j}\right)\left(w_{i,j}-1\right)^2, \tag{9}$$

where λ_1 and λ_2 are the positive numbers to control the balance between the two terms in (9). We note in (9) that when $s_{i,j}$ is too small (a negative number), the LiDAR observation is very noisy, and therefore $\exp(-s_{i,j})$ is large and $\exp(s_{i,j})$ is small. The optimization process drives $w_{i,j}$ to be zero. Similarly, when $s_{i,j}$ is not small (the LiDAR observation is not noisy), $\exp(-s_{i,j})$ is small and $\exp(s_{i,j})$ is large and therefore the optimization process drives $w_{i,j}$ to be one. Finally, we also incorporate nonnegativity constraint on $w_{i,j}$ in the optimization model:

$$w_{i,j} \geq 0, \quad 1 \leq i \leq m,\ 1 \leq j \leq n. \tag{10}$$

For the ease of presentation, we denote $\mathbf{x} = \{x_{i,j}\}$ and $\mathbf{w} = \{w_{i,j}\}$. According to (4), (6), (9), and (10), the combined optimization model is given as follows:

$$\begin{aligned}(\mathbf{x}, \mathbf{w}) = \arg\min_{(\mathbf{x},\mathbf{w})} \Bigg\{ & \frac{1}{2} \sum_{i=1}^{m} \sum_{j=1}^{n} w_{i,j} \left(y_{i,j} - x_{i,j}\right)^2 + \alpha \sum_{i=1}^{m} \sum_{j=1}^{n} w_{i,j} \mathrm{TV}\left(x_{i,j}\right) + \chi(\mathbf{w}) \\ & + \lambda_1 \sum_{i=1}^{m} \sum_{j=1}^{n} \exp\left(-s_{i,j}\right) w_{i,j}^2 + \lambda_2 \sum_{i=1}^{m} \sum_{j=1}^{n} \exp\left(s_{i,j}\right) \left(w_{i,j} - 1\right)^2 \Bigg\},\end{aligned} \tag{11}$$

where α is a positive number to balance the contribution of the total variation regularization term and the other terms and $\chi_{\mathscr{W}}(\mathbf{w})$ is the characteristic function of the non-negativity constraint set $\mathscr{W} = \{\mathbf{w}: w_{i,j} \geq 0,\ 1 \leq i \leq m,\ 1 \leq j \leq n\}$

$$\chi_{\mathscr{W}}(\mathbf{w}) = \begin{cases} 0, & \mathbf{w} \in \mathscr{W}, \\ +\infty, & \text{otherwise.} \end{cases} \tag{12}$$

2.3. The Algorithm. In this subsection, we will introduce the algorithm for the proposed model. Since both $d(x_{i,j}, x_{i-1,j})$ and $d(x_{i,j}, x_{i-1,j})$ are fixed in LiDAR observations, for simplicity, we use $\tau_{i,j}$ and $\mu_{i,j}$ to represent them, respectively, in the following discussion. Let $p_{i,j} = x_{i,j} - x_{i,j-1}, q_{i,j} = x_{i,j} - x_{i-1,j}$. We can rewrite (11) as follows:

$$\begin{aligned}(\mathbf{x}, \mathbf{w}, \mathbf{p}, \mathbf{q}) = \operatorname*{argmin}_{(\mathbf{x},\mathbf{w},\mathbf{p},\mathbf{q})} \Bigg\{ & \frac{1}{2} \sum_{i=1}^{m} \sum_{j=1}^{n} w_{i,j} \left(y_{i,j} - x_{i,j}\right)^2 + \alpha \sum_{i=1}^{m} \sum_{j=1}^{n} w_{i,j} \frac{\left|p_{i,j}\right|}{\tau_{i,j}} + \alpha \sum_{i=1}^{m} \sum_{j=1}^{n} w_{i,j} \frac{\left|q_{i,j}\right|}{\mu_{i,j}} \\ & + \chi_W(\mathbf{w}) + \lambda_1 \sum_{i=1}^{m} \sum_{j=1}^{n} \exp\left(-s_{i,j}\right) w_{i,j}^2 + \lambda_2 \sum_{i=1}^{m} \sum_{j=1}^{n} \exp\left(s_{i,j}\right) \left(w_{i,j} - 1\right)^2 \Bigg\}, \\ s.t.\ & p_{i,j} = x_{i,j} - x_{i,j-1},\ q_{i,j} = x_{i,j} - x_{i-1,j}.\end{aligned} \tag{13}$$

The augmented Lagrangian of the above-constrained optimization problem is given as follows:

$$\begin{aligned}L_{\gamma_1,\gamma_2}(\mathbf{x}, \mathbf{w}, \mathbf{p}, \mathbf{q}; \mathbf{\Lambda}, \Gamma) = & \frac{1}{2} \sum_{i=1}^{m} \sum_{j=1}^{n} w_{i,j} \left(y_{i,j} - x_{i,j}\right)^2 + \alpha \sum_{i=1}^{m} \sum_{j=1}^{n} w_{i,j} \frac{\left|p_{i,j}\right|}{\tau_{i,j}} \\ & + \alpha \sum_{i=1}^{m} \sum_{j=1}^{n} w_{i,j} \frac{\left|q_{i,j}\right|}{\mu_{i,j}} + \chi_W(w) + \lambda_1 \sum_{i=1}^{m} \sum_{j=1}^{n} \exp\left(-s_{i,j}\right) w_{i,j}^2 \\ & + \lambda_2 \sum_{i=1}^{m} \sum_{j=1}^{n} \exp\left(s_{i,j}\right) \left(w_{i,j} - 1\right)^2 + \sum_{i=1}^{m} \sum_{j=1}^{n} \Lambda_{i,j} \left[p_{i,j} - \left(x_{i,j} - x_{i,j-1}\right)\right] \\ & + \sum_{i=1}^{m} \sum_{j=1}^{n} \Gamma_{i,j} \left[q_{i,j} - \left(x_{i,j} - x_{i-1,j}\right)\right] + \frac{\gamma_1}{2} \sum_{i=1}^{m} \sum_{j=1}^{n} \left[p_{i,j} - \left(x_{i,j} - x_{i,j-1}\right)\right]^2 \\ & + \frac{\gamma_2}{2} \sum_{i=1}^{m} \sum_{j=1}^{n} \left[q_{i,j} - \left(x_{i,j} - x_{i-1,j}\right)\right]^2,\end{aligned} \tag{14}$$

where $\gamma_1, \gamma_2 > 0$ are penalization parameters and Λ and Γ are Lagrange multipliers.

With an initial guess of $(\mathbf{x}^0, \mathbf{w}^0, \mathbf{p}^0, \mathbf{q}^0; \Lambda^0, \Gamma^0)$, the iterations of the alternating direction method of multipliers [26] are given as follows:

$$\begin{cases} \mathbf{x}^{k+1} = \arg\min_{\mathbf{x}} L_{\gamma_1,\gamma_2}\left(\mathbf{x}, \mathbf{w}^k, \mathbf{p}^k, \mathbf{q}^k; \boldsymbol{\Lambda}^k, \Gamma^k\right), \\ \mathbf{w}^{k+1} = \arg\min_{\mathbf{w}} L_{\gamma_1,\gamma_2}\left(\mathbf{x}^{k+1}, \mathbf{w}, \mathbf{p}^k, \mathbf{q}^k; \boldsymbol{\Lambda}^k, \Gamma^k\right), \\ \mathbf{p}^{k+1} = \arg\min_{\mathbf{p}} L_{\gamma_1,\gamma_2}\left(\mathbf{x}^{k+1}, \mathbf{w}^{k+1}, \mathbf{p}, \mathbf{q}^k; \boldsymbol{\Lambda}^k, \Gamma^k\right), \\ \mathbf{q}^{k+1} = \arg\min_{\mathbf{q}} L_{\gamma_1,\gamma_2}\left(\mathbf{x}^{k+1}, \mathbf{w}^{k+1}, \mathbf{p}^{k+1}, \mathbf{q}; \boldsymbol{\Lambda}^k, \Gamma^k\right), \\ \Lambda_{i,j}^{k+1} = \Lambda_{i,j}^k + \gamma_1\left[p_{i,j}^{k+1} - \left(x_{i,j}^{k+1} - x_{i,j-1}^{k+1}\right)\right], \\ \Gamma_{i,j}^{k+1} = \Gamma_{i,j}^k + \gamma_2\left[q_{i,j}^{k+1} - \left(x_{i,j}^{k+1} - x_{i-1,j}^{k+1}\right)\right]. \end{cases} \tag{15}$$

Next, we demonstrate how to solve the abovementioned subproblems (15) with respect to $(\mathbf{x}, \mathbf{w}, \mathbf{p}, \mathbf{q})$.

Let us consider the $\mathbf{x}$-subproblem in (15):

$$\begin{aligned} \mathbf{x}^{k+1} = \arg\min_{\mathbf{x}} \Bigg\{ & \frac{1}{2}\sum_{i=1}^{m}\sum_{j=1}^{n} w_{i,j}\left(y_{i,j} - x_{i,j}\right)^2 + \frac{\gamma_1}{2}\sum_{i=1}^{m}\sum_{j=1}^{n}\left[p_{i,j}^k + \frac{\Lambda_{i,j}^k}{\gamma_1} - \left(x_{i,j} - x_{i,j-1}\right)\right]^2 \\ & + \frac{\gamma_2}{2}\sum_{i=1}^{m}\sum_{j=1}^{n}\left[q_{i,j}^k + \frac{\Gamma_{i,j}^k}{\gamma_2} - \left(x_{i,j} - x_{i-1,j}\right)\right]^2 \Bigg\}. \end{aligned} \tag{16}$$

Noting that the data-fitting term will vanish if there is no observation data $y_{i,j}$. The optimality condition of $\mathbf{x}$-subproblem is given by

$$\begin{cases} \left(w_{i,j}^k + 2\gamma_1 + 2\gamma_2\right)x_{i,j} - \gamma_1\left(x_{i,j+1} + x_{i,j-1}\right) - \gamma_2\left(x_{i-1,j} + x_{i+1,j}\right) & \\ = w_{i,j}^k y_{i,j} + \gamma_1\left(p_{i,j}^k - p_{i,j+1}^k\right) + \gamma_2\left(q_{i,j}^k - q_{i+1,j}^k\right) + \Lambda_{i,j}^k - \Lambda_{i,j+1}^k + \Gamma_{i,j}^k - \Gamma_{i+1,j}^k, & \text{if } y_{i,j} \text{ exists}, \\ 2\left(\gamma_1 + \gamma_2\right)x_{i,j} - \gamma_1\left(x_{i,j+1} + x_{i,j-1}\right) - \gamma_2\left(x_{i-1,j} + x_{i+1,j}\right) & \\ = \gamma_1\left(p_{i,j}^k - p_{i,j+1}^k\right) + \gamma_2\left(q_{i,j}^k - q_{i+1,j}^k\right) + \Lambda_{i,j}^k - \Lambda_{i,j+1}^k + \Gamma_{i,j}^k - \Gamma_{i+1,j}^k, & \text{otherwise}. \end{cases} \tag{17}$$

We can solve the above set of equations by using the conjugate gradient (CG) method [27, 28].

For $\mathbf{w}$-subproblem, we have

$$\begin{aligned} \mathbf{w}^{k+1} = \arg\min_{\mathbf{w}\geq 0} \Bigg\{ & \frac{1}{2}\sum_{i=1}^{m}\sum_{j=1}^{n} w_{i,j}\left(y_{i,j} - x_{i,j}^{k+1}\right)^2 + \alpha\sum_{i=1}^{m}\sum_{j=1}^{n} w_{i,j}\frac{\left|p_{i,j}^k\right|}{\tau_{i,j}} \\ & + \alpha\sum_{i=1}^{m}\sum_{j=1}^{n} w_{i,j}\frac{\left|q_{i,j}^k\right|}{\mu_{i,j}} + \lambda_1\sum_{i=1}^{m}\sum_{j=1}^{n}\exp\left(-s_{i,j}\right)w_{i,j}^2 \\ & + \lambda_2\sum_{i=1}^{m}\sum_{j=1}^{n}\exp\left(s_{i,j}\right)\left(w_{i,j} - 1\right)^2 \Bigg\}. \end{aligned} \tag{18}$$

We note that $w_{i,j}$ are decoupled, and we only need to deal with scalar optimization problems. More precisely, if $y_{i,j}$ exists, the scalar optimization problem is given by

$$\begin{aligned} w_{i,j}^{k+1} = \arg\min_{w\geq 0} \Bigg\{ & \frac{1}{2}w_{i,j}\left(y_{i,j} - x_{i,j}^{k+1}\right)^2 + \alpha w_{i,j}\frac{\left|p_{i,j}^k\right|}{\tau_{i,j}} \\ & + \alpha w_{i,j}\frac{\left|q_{i,j}^k\right|}{\mu_{i,j}} + \lambda_1\exp\left(-s_{i,j}\right)w_{i,j}^2 \\ & + \lambda_2\exp\left(s_{i,j}\right)\left(w_{i,j} - 1\right)^2 \Bigg\}. \end{aligned} \tag{19}$$

If $y_{i,j}$ does not exist, it is equal to

$$w_{i,j}^{k+1} = \arg\min_{w\geq 0}\left\{\alpha w_{i,j}\frac{\left|p_{i,j}^{k}\right|}{\tau_{i,j}} + \alpha w_{i,j}\frac{\left|q_{i,j}^{k}\right|}{\mu_{i,j}} + \lambda_1 \exp\left(-s_{i,j}\right)w_{i,j}^{2} + \lambda_2 \exp\left(s_{i,j}\right)\left(w_{i,j}-1\right)^{2}\right\}. \tag{20}$$

Both the above two scalar optimization problems are convex. And one can readily get that

$$\mathbf{w}^{k+1} = \max\left\{\overline{\mathbf{w}}^{k+1}, 0\right\}, \tag{21}$$

where

$$\overline{w}_{i,j}^{k+1} = \begin{cases} \dfrac{2\lambda_2 \exp\left(s_{i,j}\right) - 1/2\left(y_{i,j} - x_{i,j}^{k+1}\right)^{2} - \alpha\left|p_{i,j}^{k}\right|/\tau_{i,j} - \alpha\left|p_{i,j}^{k}\right|/\mu_{i,j}}{2\lambda_1 \exp\left(-s_{i,j}\right) + 2\lambda_2 \exp\left(s_{i,j}\right)}, & \text{if } y_{i,j} \text{ exists,} \\ \dfrac{2\lambda_2 \exp\left(s_{i,j}\right) - \alpha\left|p_{i,j}^{k}\right|/\tau_{i,j} - \alpha\left|q_{i,j}^{k}\right|/\mu_{i,j}}{2\lambda_1 \exp\left(-s_{i,j}\right) + 2\lambda_2 \exp\left(s_{i,j}\right)}, & \text{otherwise.} \end{cases} \tag{22}$$

For **p**-subproblem and **q**-subproblem, they are given by

$$\mathbf{p}^{k+1} = \arg\min_{\mathbf{p}}\left\{\alpha\sum_{i=1}^{m}\sum_{j=1}^{n} w_{i,j}\frac{\left|p_{i,j}\right|}{\tau_{i,j}} + \frac{\gamma_1}{2}\sum_{i=1}^{m}\sum_{j=1}^{n}\left[p_{i,j} + \frac{\Lambda_{i,j}^{k}}{\gamma_1} - \left(x_{i,j}^{k+1} - x_{i,j-1}^{k+1}\right)\right]^{2}\right\}, \tag{23}$$

and

$$\mathbf{q}^{k+1} = \arg\min_{\mathbf{q}}\left\{\alpha\sum_{i=1}^{m}\sum_{j=1}^{n} w_{i,j}\frac{\left|q_{i,j}\right|}{\mu_{i,j}} + \frac{\gamma_2}{2}\sum_{i=1}^{m}\sum_{j=1}^{n}\left[q_{i,j} + \frac{\Gamma_{i,j}^{k}}{\gamma_2} - \left(x_{i,j}^{k+1} - x_{i-1,j}^{k+1}\right)\right]^{2}\right\}, \tag{24}$$

respectively. These two subproblems can be solved by using the soft-thresholding technique [29], and their solutions are given by

$$\begin{aligned} p_{i,j}^{k+1} &= \max\left(\left|\left(x_{i,j}^{k+1} - x_{i,j-1}^{k+1}\right) - \frac{\Lambda_{i,j}^{k}}{\gamma_1}\right| - \frac{\alpha w_{i,j}^{k+1}}{\gamma_1 \tau_{i,j}}, 0\right)\operatorname{sign}\left(\left(x_{i,j}^{k+1} - x_{i,j-1}^{k+1}\right) - \frac{\Lambda_{i,j}^{k}}{\gamma_1}\right), \\ q_{i,j}^{k+1} &= \max\left(\left|\left(x_{i,j}^{k+1} - x_{i-1,j}^{k+1}\right) - \frac{\Gamma_{i,j}^{k}}{\gamma_2}\right| - \frac{\alpha w_{i,j}^{k+1}}{\gamma_2 \mu_{i,j}}, 0\right)\operatorname{sign}\left(\left(x_{i,j}^{k+1} - x_{i-1,j}^{k+1}\right) - \frac{\Gamma_{i,j}^{k}}{\gamma_2}\right), \end{aligned} \tag{25}$$

where $\operatorname{sign}(p) := o/|p|$.

Finally, the overall algorithm is summarized in Algorithm 1.

2.4. The Calculation of Parameters. In the proposed denoising scheme, there are several parameters to be determined. In this subsection, we incorporate the L-curve method to determine the values of parameters. The L-curve is a tradeoff curve between two quantities that both need to be controlled and balanced [30, 31]. It is widely used in the engineering and applied mathematics field.

First, the regularization parameter α in (14) is crucial in our proposed method since it controls the ratio between the data-fitting term and the total variation regularization term. When the value of α is large (small), the importance of the

Input: Noisy data $\mathbf{y}$, SNR data $\mathbf{s}$, and parameters $\alpha, \lambda_1, \lambda_2, \gamma_1, \gamma_2$.
Initialization: $\mathbf{x}^0 = \mathbf{y}, \mathbf{w}^0 = 1, \mathbf{p}^0 = 0, \mathbf{q}^0 = 0, \Lambda^0 = 0, \Gamma^0 = 0, k = 0$.
(1) **while** Stopping criteria is not satisfied **do**
(2) Solve $\mathbf{x}^{k+1}$ by using CG for (17)
(3) Solve $\mathbf{w}^{k+1}$ by (21)
(4) Find $\mathbf{p}^{k+1}$ by (24)
(5) Find $\mathbf{q}^{k+1}$ by (25)
(6) Update the multipliers by $\Lambda_{i,j}^{k+1} = \Lambda_{i,j}^{k} + \gamma_1 [p_{i,j}^{k+1} - (x_{i,j}^{k+1} - x_{i,j-1}^{k+1})]$ and $\Gamma_{i,j}^{k+1} = \Gamma_{i,j}^{k} + \gamma_2 [q_{i,j}^{k+1} - (x_{i,j}^{k+1} - x_{i-1,j}^{k+1})]$
(7) $k \leftarrow k + 1$
(8) **end while**

Algorithm 1

total variation regularization term is large (small) and the denoising results are more (less) regularized. Moreover, there are two parameters λ_1 and λ_2 in (14), and they can affect the values of $w_{i,j}$ according to the SNR values of LiDAR observations. When the ratio λ_1/λ_2 is large (i.e., λ_1 is larger than λ_2), the term $\lambda_1 \sum_{i=1}^{m} \sum_{j=1}^{m} \exp(-s_{i,j}) w_{i,j}^2$ is more important than the term $\lambda_2 \sum_{i=1}^{m} \sum_{j=1}^{m} \exp(-s_{i,j}) (w_{i,j} - 1)^2$. It follows that when LiDAR observations have small SNR values, there would be more zero values of $w_{i,j}$ in the optimization procedure. In contrast, when the ratio λ_1/λ_2 is small and LiDAR observations have large SNR values, there would be more values of $w_{i,j}$ to be one in the optimization procedure.

In the L-curve method, we consider the following two quantities:

$$D(\mathbf{x}(\alpha, \lambda_1, \lambda_2), \mathbf{w}(\alpha, \lambda_1, \lambda_2)) := -\log_{10}\left(\frac{\sum_{i=1}^{m} \sum_{j=1}^{n} w_{i,j}(\alpha, \lambda_1, \lambda_2)\left(y_{i,j} - x_{i,j}(\alpha, \lambda_1, \lambda_2)\right)^2}{\sum_{i=1}^{m} \sum_{j=1}^{n} w_{i,j}(\alpha, \lambda_1, \lambda_2)}\right), \tag{26}$$

and

$$S(\mathbf{x}(\alpha, \lambda_1, \lambda_2), \mathbf{w}(\alpha, \lambda_1, \lambda_2)) := -\log_{10}\left(\frac{\sum_{i=1}^{m} \sum_{j=1}^{n} w_{i,j}(\alpha, \lambda_1, \lambda_2) TV\left(x_{i,j}(\alpha, \lambda_1, \lambda_2)\right)}{\sum_{i=1}^{m} \sum_{j=1}^{n} w_{i,j}(\alpha, \lambda_1, \lambda_2)}\right). \tag{27}$$

The first quantity $D(\mathbf{x}(\alpha, \lambda_1, \lambda_2), \mathbf{w}(\alpha, \lambda_1, \lambda_2))$ refers to the degree of data fitting when $\mathbf{x}$ and $\mathbf{w}$ are computed by Algorithm 1 for fixed α, λ_1, and λ_2. Similarly, the second quantity $S(\mathbf{x}(\alpha, \lambda_1, \lambda_2), \mathbf{w}(\alpha, \lambda_1, \lambda_2))$ refers to the degree of smoothness in the regularization for the computed $\mathbf{x}$ and $\mathbf{w}$. In order to compare the degrees of data fitting and smoothness with respect to different numbers of denoising values $w_{i,j}$ across different values of λ_1 and λ_2, the weighted average of data fitting and smoothness are accounted in the two quantities. The main idea of the L-curve method is to select the suitable values of α, λ_1, and λ_2 such that both $D(\mathbf{x}(\alpha, \lambda_1, \lambda_2), \mathbf{w}(\alpha, \lambda_1, \lambda_2))$ and $S(\mathbf{x}(\alpha, \lambda_1, \lambda_2), \mathbf{w}(\alpha, \lambda_1, \lambda_2))$ are balanced.

As an illustration, we apply Algorithm 1 to the LiDAR observations in Figure 1 for different values of α, λ_1, and λ_2. More precisely, in Figure 2(a), we fix λ_1 (100) and λ_2 (0.5, 5, 50, 500) and compute $\mathbf{x}$ and $\mathbf{w}$ for different values of α (0.01, 0.05, 0.1, 0.3, 0.5, 0.8, 1, 5). In Figure 2(a), we plot $D(\mathbf{x}(\alpha, \lambda_1, \lambda_2), \mathbf{w}(\alpha, \lambda_1, \lambda_2))$ and $S(\mathbf{x}(\alpha, \lambda_1, \lambda_2), \mathbf{w}(\alpha, \lambda_1, \lambda_2))$. The lines of points of D and S with respect to α are generated for each fixed λ_1 and λ_2. In total, there are four lines of points in Figure 2(a). We observe in each line that when α is small, D is large and S is small, and thus the points appear in the left hand side of the line. When α is large, D is small and S is large, and thus the points appear in the right hand side of the line. We find that there are several corner points in the line, and they refer to several large rates of change of data fitting with respect to the change of smoothness. Here, we can pick up the corner point with the largest rate of change and employ the corresponding value of α for regularization. Next, we select the values of λ_1 and λ_2 by comparing the selected corner points of different lines. Here, we can pick up the selected corner point with the largest D (the data fitting is good) and the largest S (the smoothness is large). According to the plot in Figure 2(a), we select $\alpha^* = 0.5$, $\lambda_1^* = 100$,and $\lambda_2^* = 500$.

Based on the above idea, we summarize our L-curve method with automatic selection of α, λ_1, and λ_2 in Algorithm 2.

From Figure 2, it is obvious that the model is very sensitive for different values of the regularization parameter α due to its balance effect for data fitting and smoothing. However, from Figure 2(a), for fixed values of parameters α

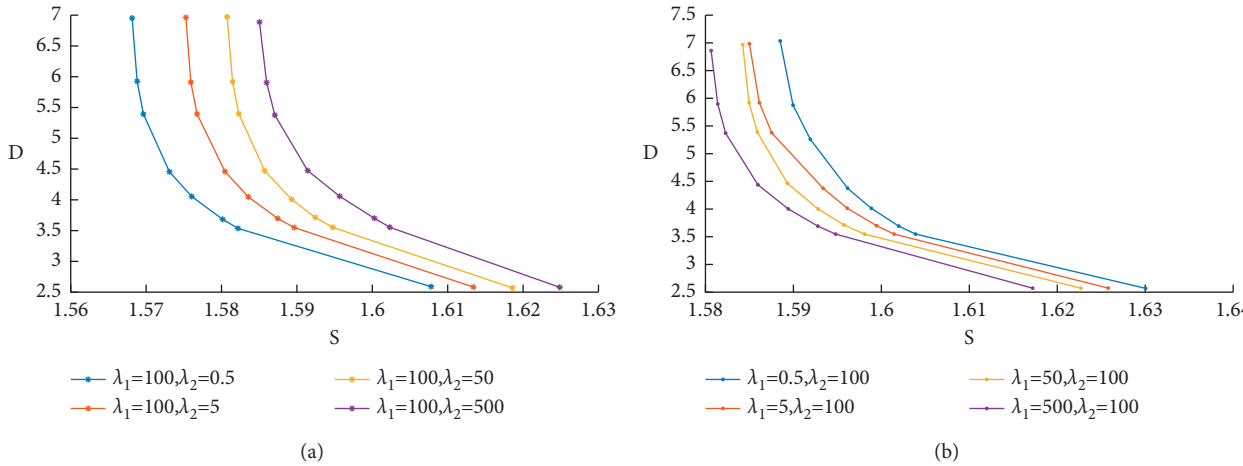

Figure 2: L-curves of different parameters α, λ_1, and λ_2.

Input: The set of parameters values α, λ_1, λ_2.
Initialization: Corner point $c^0 = (0, 0)$
(1) **while** the set of parameter values is not empty **do**
(2) Select (λ_1, λ_2) from the parameter set
(3) Find the corner point c^* of the generated lines of points $D(\mathbf{x}(\alpha, \lambda_1, \lambda_2), \mathbf{w}(\alpha, \lambda_1, \lambda_2)), S((\mathbf{x}(\alpha, \lambda_1, \lambda_2), \mathbf{w}(\alpha, \lambda_1, \lambda_2)))$ from a set of α values, and record the corresponding $\widetilde{\alpha}$.
(4) If the position of c^* is higher than the position of c^0 in the D-S plot, set $c^0 = c^*$, $\alpha^* = \widetilde{\alpha}$, $\lambda_1^* = \lambda_1$, $\lambda_2^* = \lambda_2$
(5) end while

Algorithm 2: L-curve Method.

and λ_1, the changes of D and S for different values of λ_2 are small (less than 1), which means that the model is pretty robust for parameter λ_2. To evaluate the robustness of parameter λ_1, we plot the four L-curves with respect to α $(0.01, 0.05, 0.1, 0.3, 0.5, 0.8, 1, 5)$ for fixed λ_2 in Figure 2(b), where $\lambda_2 = 100$, λ_1 varies in $\{0.5, 5, 50, 500\}$ for different curves. Similar to the results of parameter λ_2, one can readily find that the proposed model is quite robust for parameter λ_1.

3. Results and Discussion

In this section, to illustrate the effectiveness of the proposed scheme (denoted as the "TV" method), we will show some denoising results by this scheme and compare them with the results generated by other denoising methods for the LiDAR data collected at HKIA. Clearly, the LiDAR data we study in this paper are time-varying and distance-varying, so that we compare the results by the DWT method [9] and the EMD-CIIT method [16]. They are denoted as "DWT" and "EMD-CIIT." Moreover, we consider the method used by Baranov et al. [18] (denoted as "Baranov" in the rest of this article) and Newsom et al. [19] (denoted as "Newsom" in the rest of this article) as well as the method used by Hong Kong Observatory (denoted as the HKO method in the rest of this article) (see Algorithm 3 for more detailed description). Since Baranov et al. did not give an exact SNR threshold level in [18], we set the SNR threshold level as −5, which is used by Hong Kong Observatory for the LiDAR data observed at HKIA. The effects of averaging smoothing algorithm and median smoothing algorithm are shown to be about the same in [18], so that we apply a five-point-based averaging smoothing algorithm to the data selected by the SNR threshold level. Refer to Algorithm 4 for more detailed description.

3.1. Comparison Results with the "DWT" and "EMD-CIIT" Methods. Figures 3 and 4 show the results of the "DWT" method, the "EMD-CIIT" method, and the proposed TV method for LiDAR data collected on 5 March 2015 from 04 : 16 : 02 to 04 : 16 : 25 with a fixed azimuth angle 224.0° and 4 March 2015 from 21 : 26 : 16 to 21 : 46 : 39 with a fixed azimuth angle 314.0°, respectively. According to the record from Hong Kong International Airport, these two wind profiles from LiDAR data correspond to two windshear cases. According to Figures 3 and 4, one can readily find that

(1) The "DWT" method and the "EMD-CIIT" method cannot remove very noisy observations, but our proposed scheme can remove noisy observations with very low SNR values effectively.

For example, there is a high peak appearing at the range of around 8200 m in the LiDAR data observation in Figure 3. The DWT denoising method (x_{DWT}) and the EMD-CIIT denoising method

Input: LiDAR observations $y_{i,j}$ and their SNR values $s_{i,j}$ for $1 \le i \le m$ and $1 \le j \le n$

(1) $i = 1$ (for each azimuth angle)
(2) **for** $j = 1$ to n (along each range) **do**
(3) If $s_{i,j} < = -5$, then $y_{i,j} = NA$
(4) **end for**
(5) $x_{i,1} = y_{i,1}$
(6) **for** $j = 2$ to n **do**
(7) If $|x_{i,j-1}^{(HKO)} - y_{i,j}| > 16$, then $x_{i,j}^{(HKO)} = x_{i,j-1}^{(HKO)} \times 0.95 + y_{i,j} \times 0.05$
(8) If $x_{i,j-1}^{(HKO)} = NA$ and $y_{i,j+1} = NA$, then $x_{i,j}^{(HKO)} = NA$
(9) **end for**
(10) Set $i = i + 1$ and Goto Step 2

Algorithm 3: The Denoising Method used by Hong Kong Observatory.

Input: LiDAR observations $y_{i,j}$ and their SNR values $s_{i,j}$ for $1 \le i \le m$ and $1 \le j \le n$

(1) Set $i = 1$ (for each azimuth angle)
(2) **for** $j = 1$ to n (along each range) **do**
(3) If $s_{i,j} < = -5$, then $y_{i,j} = NA$
(4) **end for**
(5) $x_{i,1}^{Baranov} = y_{i,1}$
(6) $x_{i,2}^{Baranov} = y_{i,1} + y_{i,2}/2$
(7) **for** $j = 3$ to $n - 2$ **do**
(8) $x_{i,j}^{Baranov} = y_{i,j-2} + y_{i,j-1} + y_{i,j} + y_{i,j+1} + y_{i,j+2}/5$
(9) **end for**
(10) $x_{i,n-1}^{Baranov} = y_{i,n-3} + y_{i,n-2} + y_{i,n-1} + y_{i,n}/4$
(11) $x_{i,n}^{Baranov} = y_{i,n-2} + y_{i,n-1} + y_{i,n}/3$
(12) Set $i = i + 1$ and Goto Step 2

Algorithm 4: The Denoising Method used by Baranov et al.

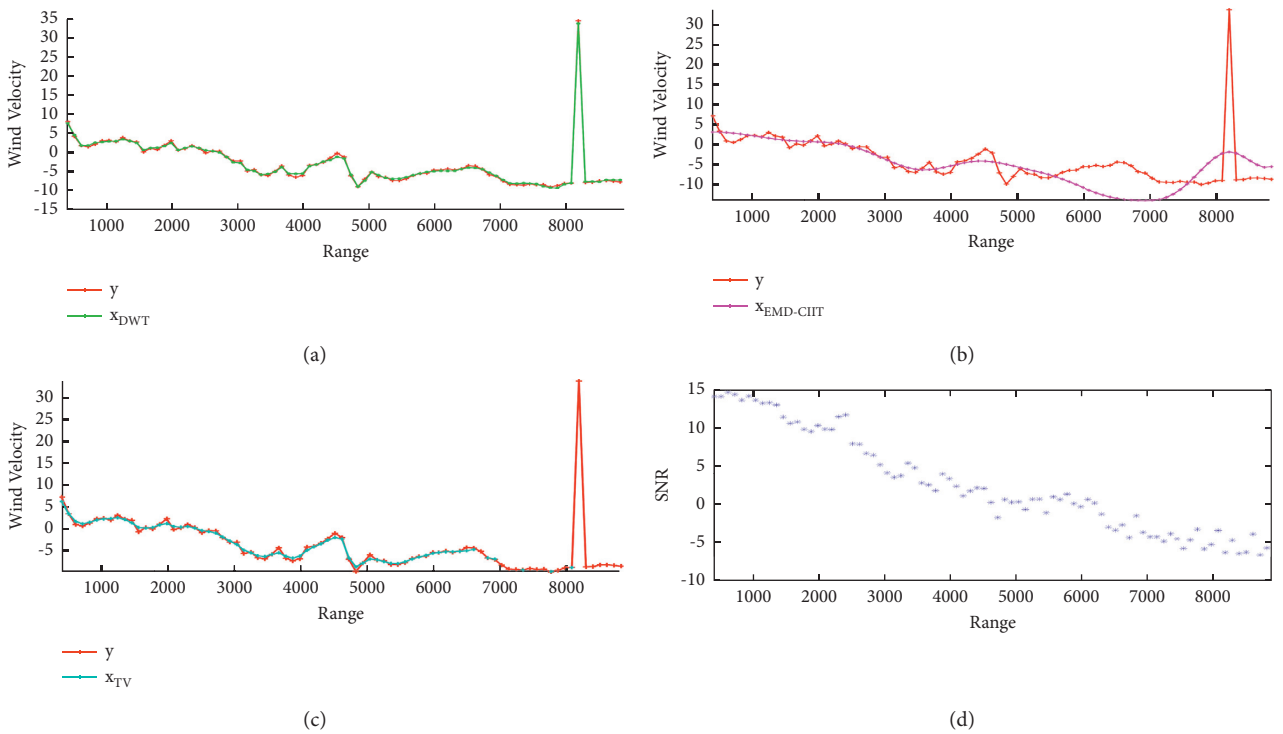

Figure 3: The denoising results by the "DWT" (a), "EMD-CIIT" (b), and our proposed scheme (c) for the LiDAR data collected on 5 March 2015 from 04 : 16 : 02 to 04 : 16 : 25 with a fixed azimuth angle (224.0°). The SNR values of the corresponding observed LiDAR data are shown in (d).

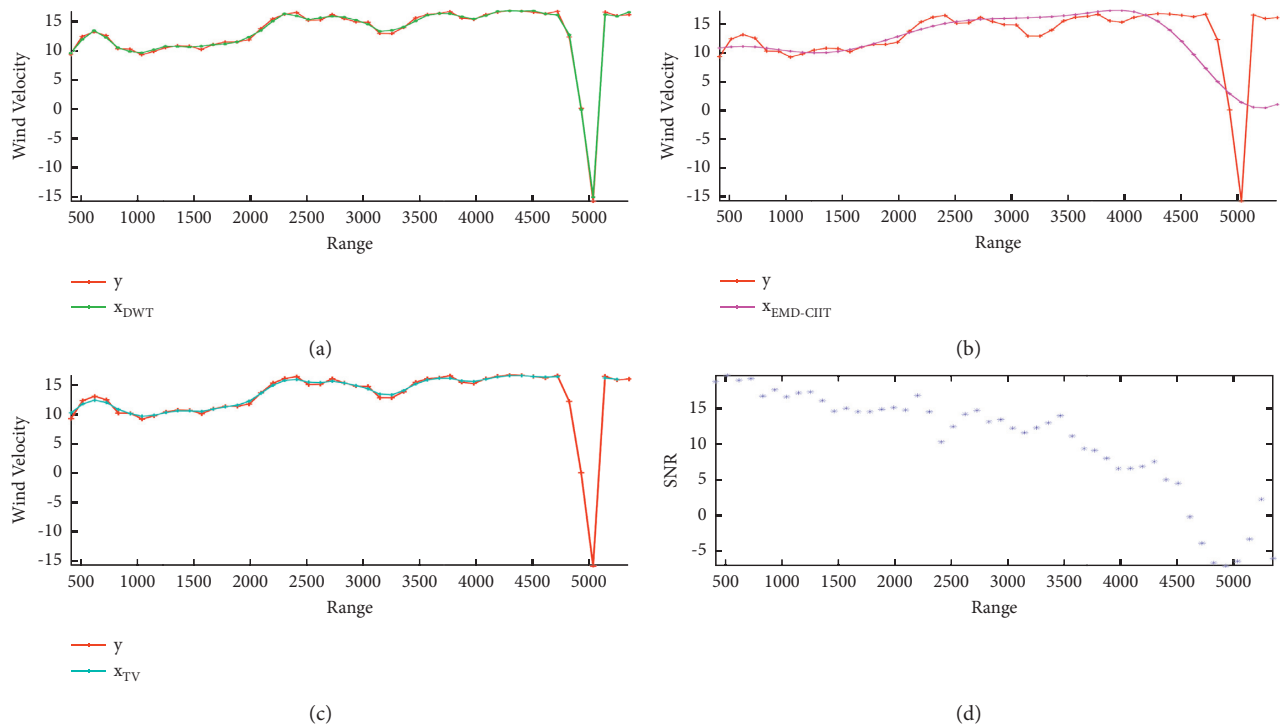

Figure 4: The denoising results by the "DWT" (a), "EMD-CIIT" (b), and our proposed scheme (c) for the LiDAR data collected on 4 March 2015 from 21 : 26 : 16 to 21 : 46 : 39 with a fixed azimuth angle (314.0°). The SNR values of the corresponding observed LiDAR data are shown in the (d).

($x_{EMD-CIIT}$) cannot remove this very noisy observation. We see from Figure 3(d) that the corresponding SNR value is about −8 at the range of around 8200 m. Indeed, it is quite acceptable to remove such noisy observation compared with neighborhood observations. Similarly, in Figure 4, there is a rock bottom appearing at the range of around 5000 m in the LiDAR data observation. From Figure 4(d), one can readily get that the corresponding SNR value is about −7 at the range of around 5000 m, which indicates the high noise intensity at this slant range. We see from Figures 4(a) and 4(b) that the "DWT" method and the "EMD-CIIT" method cannot remove such noisy observations. However, the proposed scheme (Figures 3 and 4(c)), according to the corresponding SNR values, filters both the high peak and rock bottom as well as the noisy data around them out.

(2) The method can over-smooth the input LiDAR data, and some LiDAR observations may be lost. As comparison, the denoising results of the proposed scheme are smooth but not distorted.

3.2. Comparison Results with the "Baranov" Method. Figures 5(a) and 5(c) show the results by the "Baranov" method and the proposed scheme for LiDAR data collected on 4 March 2015 from 21 : 26 : 16 to 21 : 46 : 39 with a fixed azimuth angle 314° and 5 March 2015 from 04 : 16 : 02 to 04 : 16 : 25 with a fixed azimuth angle 277°, respectively. According to Figures 5(a) and 5(c), we can easily find that

(1)The Baranov method might restore few missing points as well as some data points that are removed by the SNR threshold level by the averaging smooth algorithm. However, the values of them seem to be quite the same as the previous observed one, which play a tiny role in the following data applications such like windshear detection.

For example, in Figure 5(a), there is a rock bottom appearing at the range of around 5000 m in the LiDAR data observation. From Figure 5(b), the corresponding SNR value is about −7, which indicates the data point is removed by the SNR threshold level. However, this data point is restored by the averaging smoothing algorithm in the results by the "Baranov" method ($x_{Baranov}$). It is obvious that the velocity values of data points between the range of 4800 m and 5800 m are quite the same in $x_{Baranov}$. Similarly, there are some missing values at the range of around 9000 m and 10800 m. Some missing data points are restored with almost same values in $x_{Baranov}$.

(2) Due to the effect of the averaging smoothing algorithm, the "Baranov" method might mis-shift the velocities of some data points.

For example, there are some mis-shifted data points in the result by the "Baranov" method at the range of around 4500 m in Figure 5(a). From 5(b), the SNR values around 4500 m are around 0, which are still acceptable. Similarly, the SNR values of data points at

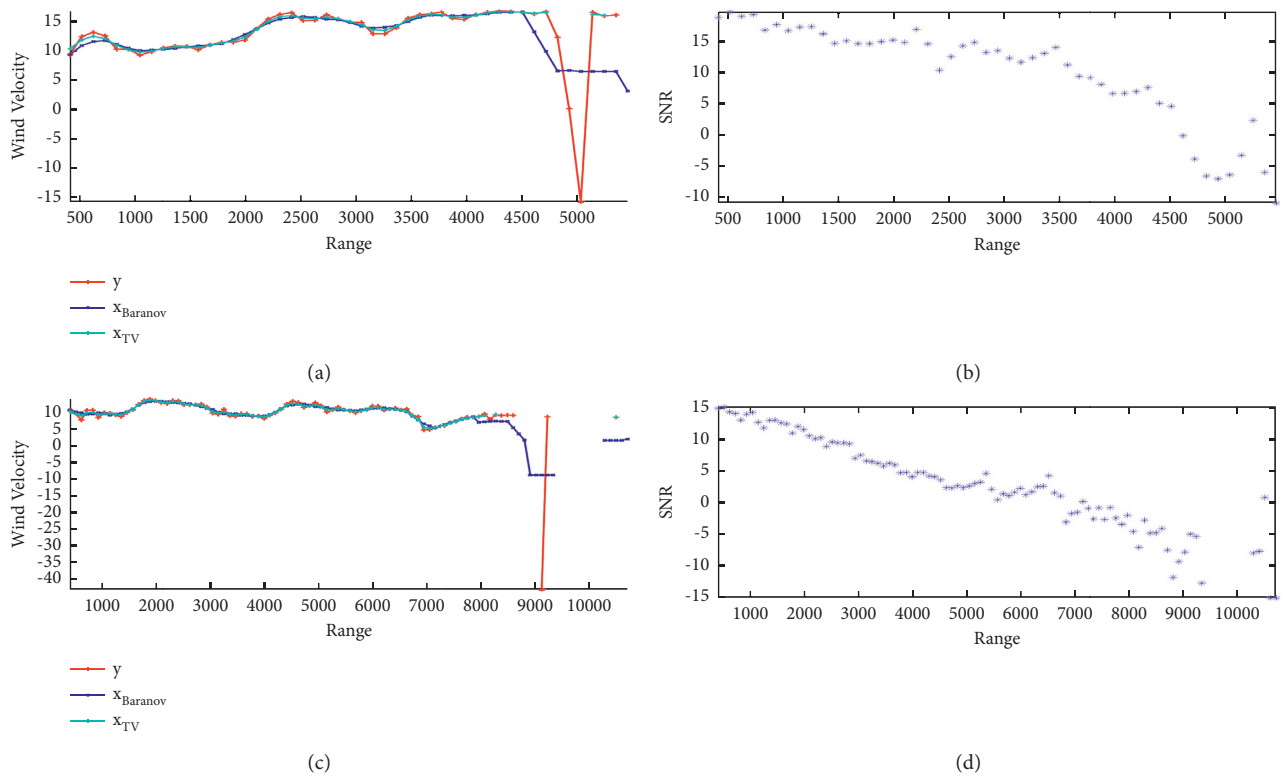

FIGURE 5: The denoising results by the proposed method x_{TV} and the "Baranov" method $x_{Baranov}$. (a) The LiDAR data were on 4 March 2015 from 21 : 26 : 16 to 21 : 46 : 39 with a fixed azimuth angle 314° and the denoising results. (b) The SNR values of the LiDAR data in the 1st row. (c) The LiDAR data were on 5 March 2015 from 04 : 16 : 02 to 04 : 16 : 25 with a fixed azimuth angle 277° and the denoising results. (d) The SNR values of the LiDAR data in the 3rd row.

the range of around 5500 m are also acceptable, but the velocity values are mis-shifted.

(3) In comparison, the results by the proposed method (x_{TV}) remove the bad observations properly and provide less useless information.

3.3. Comparison Results with HKO Method. In Figures 6(a) and 6(c), we consider LiDAR data collected on 4 March 2015 from 21 : 26 : 16 to 21 : 46 : 39 with a fixed azimuth angle 124° and 5 March 2015 from 04 : 16 : 02 to 04 : 16 : 25 with a fixed azimuth angle 139°, respectively. The denoising results x_{HKO} of LiDAR data by the HKO method are shown in Figures 6(a) and 6(c). We have the following observations.

(1) There are some mis-shifted results at the range values around 4000m-4200 m in Figure 6(a) and around 4700m-5000 m in Figure 6(c). For reference, the SNR values corresponding to LiDAR data in Figures 6(a) and 6(c) are given in Figures 6(b) and 6(d), respectively. We note in Figure 6(b) that the SNR values at 4000m-4200 m are 2–10. Similarly, the SNR values at 4700 m−5000 m are 13–18 in Figure 6(d). In these two cases, SNR values can still be in an acceptable range. However, the method by Hong Kong observatory cannot provide a reasonable denoising results in these two range values, and the detected wind profiles may be affected.

(2) In comparison, we show the denoising results x_{TV} of LiDAR data by the proposed method in Figures 6(a) and 6(c). We find that the proposed method fits the LiDAR data quite well with as much smoothness as possible based on the SNR values of the given observations.

3.4. Comparison Results with the "Newsom" Method. Note that the "Newsom" method just removes the bad observations based on the SNR values (the SNR threshold level is set to be 0.02 in [19]) without any other operations for LiDAR data, so that there are no value differences between the data after processing and the observed data. For LiDAR data in Figure 3, all the observed data after the range 4400 m are removed because their SNR values are less than 0.02. It seems that it is not reasonable to remove all these observed data points. In Figure 4, the observed data points near the rock bottom are removed. In Figures 5 and 6, the processed data by the "Newsom" method are about the same as the original observed data.

3.5. Comparison Results in Conical Scans. In Figures 7 and 8, we plot the conical scans of LiDAR data collected on 4 March 2015 from 21 : 26 : 16 to 21 : 46 : 39 and 5 March 2015 from 04 : 16 : 02 to 04 : 16 : 25 and the results by the "DWT" method, the "EMD-CIIT" method, the"Newsom" method, the "Baranov" method, the HKO method, and the proposed

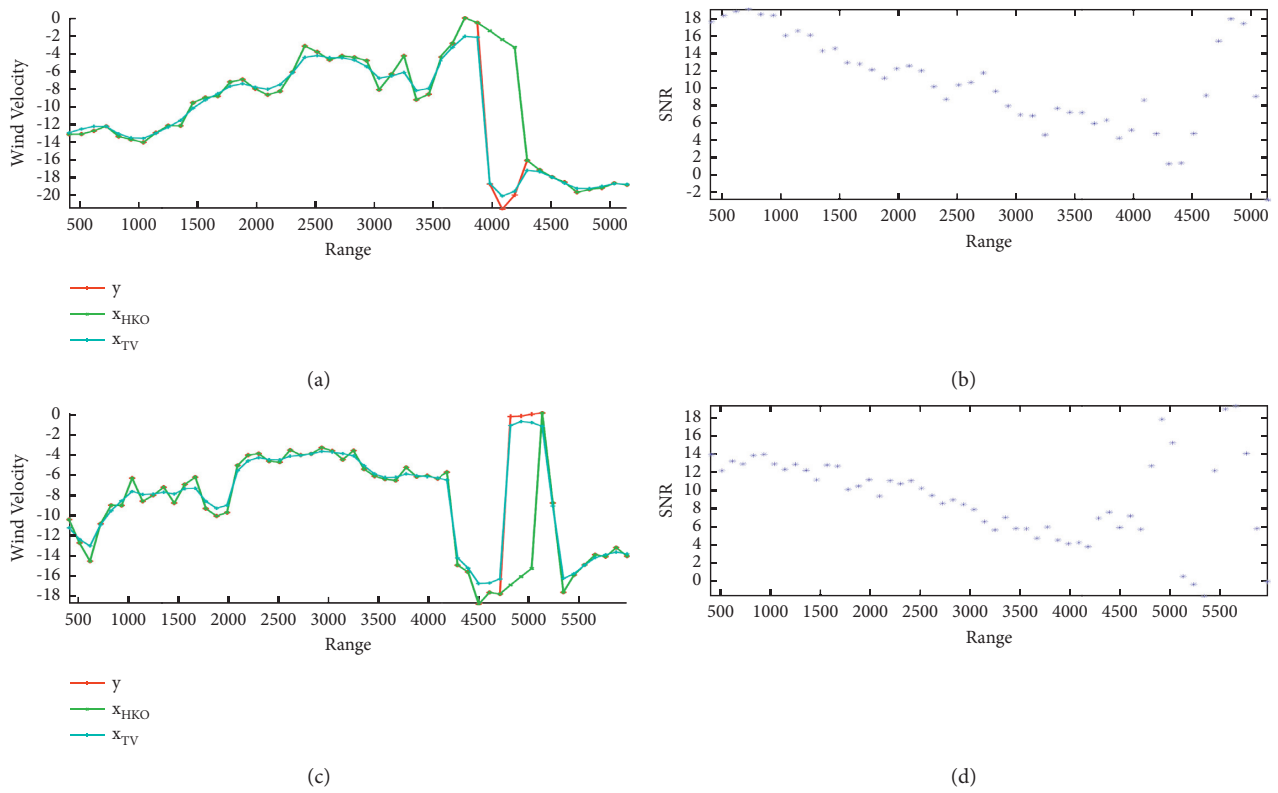

Figure 6: The denoising results by the proposed method x_{TV} and the HKO method x_{HKO}. (a) The LiDAR data were collected on 4 March 2015 from 21 : 26 : 16 to 21 : 46 : 39 with a fixed azimuth angle 124° and the denoising results. (b) The SNR values of the LiDAR data in the 1st row. (c) The LiDAR data were collected on 5 March 2015 from 04 : 16 : 02 to 04 : 16 : 25 with a fixed azimuth angle 139° and the denoising results. (d) The SNR values of the LiDAR data in the 3rd row.

method. The computational time for these methods is also given. From these figures, we can readily find that

(1) There are some spikes in the denoising results of the "DWT" method and the "EMD-CIIT" method. For example, in Figures 7(e) and 7(f), there are some spikes in the range of azimuth angles from 206° to 250°.

(2) The over-smoothness of the "EMD-CIIT" method is also overcome by the proposed scheme.

(3) There are some outliers that provide little information of the wind profile in the denoising results generated by the "Baranov" method. In comparison, the denoising results of our proposed method are much clear.

We note that Figures 7 and 8 correspond to two windshear cases in March 2015. Although the existence of outliers does not have an effect on visual judgement for windshear analysis, it can have a strong effect on machine learning methods in windshear detection. For instance, the wind profile features suggested by the machine learning method in [32] are calculated based on the maximal difference in wind velocities within a range of azimuth angles, and it is clear that the outliers can change the resulting wind profile features.

(4) Since the SNR threshold level (SNR >0.02) used by "Newsom" method is high, there are only few data points retined in the results. And the proposed method, without any fixed SNR threshold level, retained more data points which contain useful information of wind profiles.

(5) Comparing with the results by HKO method, the results of our proposed scheme is much smoother.

(6) The proposed scheme is faster than the EMD-CIIT method, but it is slower than the other methods.

For example, there are some fluctuations in the range of azimuth angles from 257° to 359° in Figure 8(g), but the data are much smoother in Figure 8(h).

To further evaluate the performance of the proposed method, we show a nonwindshear case in Figure 9. In the figure, we plot the conical scans of the LiDAR data and the denoising results by the abovementioned six methods. The LiDAR data were collected on 4 March 2015 from 00 : 00 : 16 to 00 : 00 : 39. Similarly, the denoising results given by the proposed scheme do not contain any outliers and retain more data points with good smooth effect.

3.6. Comparison Results in Noisy Observations Removal. Finally, we would like to demonstrate the capability of the proposed method in removing noisy observations compared with the "Newsom" method,the "Baranov" method, as well as

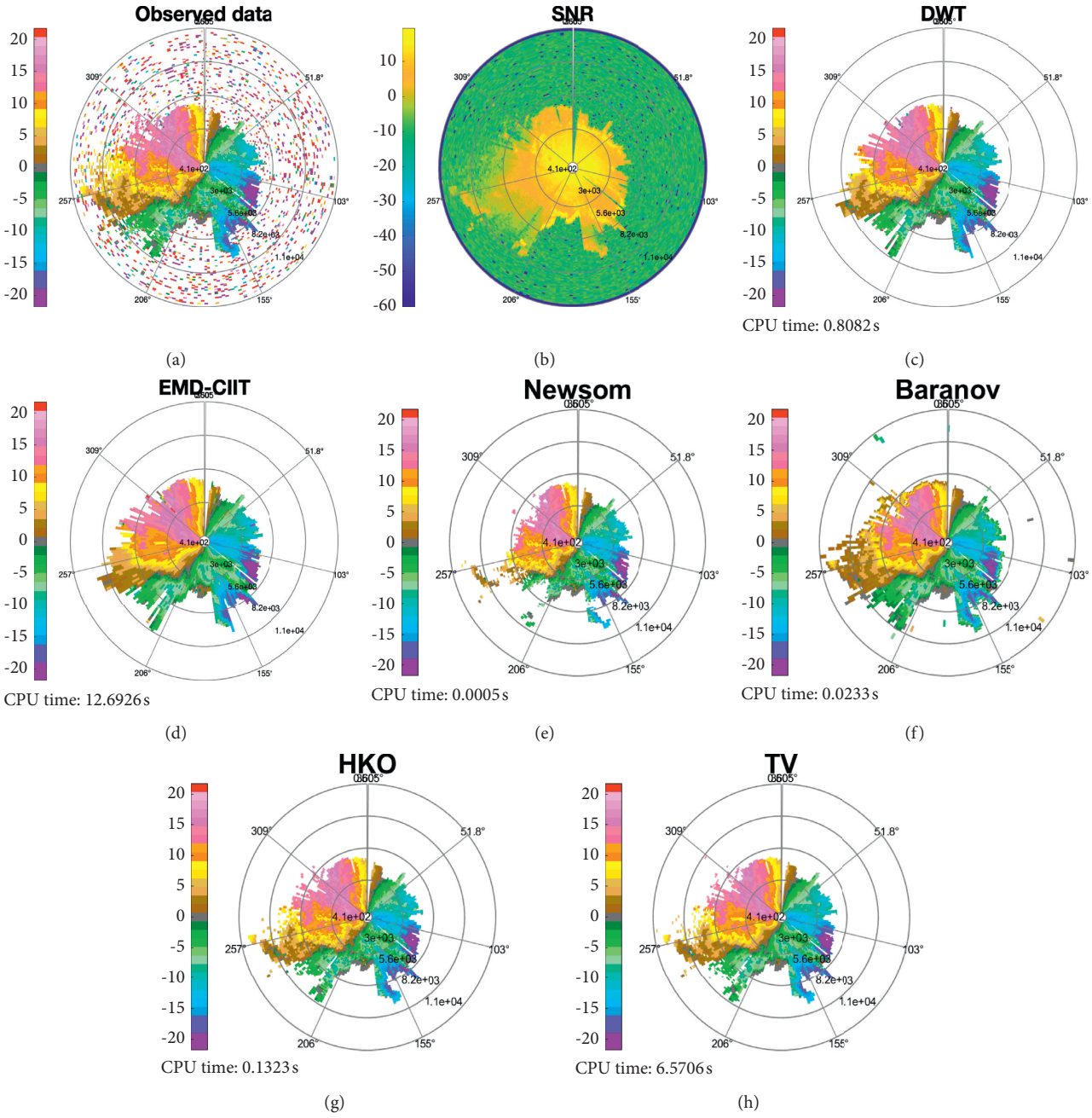

FIGURE 7: (a) The LiDAR data and (b) SNR values collected on 4 March 2015 from 21 : 26 : 16 to 21 : 46 : 39. The denoising results by (c) the "DWT" method, (d) the "EMD-CIIT" method, (e) the "Newsom" method, (f) the "Baranov" method, (g) the HKO method, and (h) the proposed scheme (denoted by TV).

the HKO method. As a matter of fact, when SNR values are too small, the LiDAR observations may not be suitable for data analysis usage. In Table 1, we show the noisy observation removal results for a set of LiDAR observations for windshear cases at Hong Kong International Airport. The set of observations was collected from 1 March to 31 March 2015. There were 147 windshear cases reported in the pilot report. Each scan of windshear cases took about 25 seconds (see the two examples in Figures 7 and 8). We see from Table 1 that

(1) Since the SNR threshold level of the"Newsom" method is 0.02, all the noisy observations are removed in the results of the "Newsom" method, but the number of the retained data points are really small.

(2) The number $\sum_{i=1}^{m}\sum_{j=1}^{n} w_{i,j}$ of denoising values by the proposed method is about the same as the number of original observations $y_{i,j}$ and the number of denoising values $x_{i,j}^{(Baranov)}$ by the "Baranov" method and the number of denoising values $x_{i,j}^{(HKO)}$ by HKO method in the slant range values from 359 m to 3509 m. Note that the SNR values of LiDAR observations in the slant range values from 359 m to

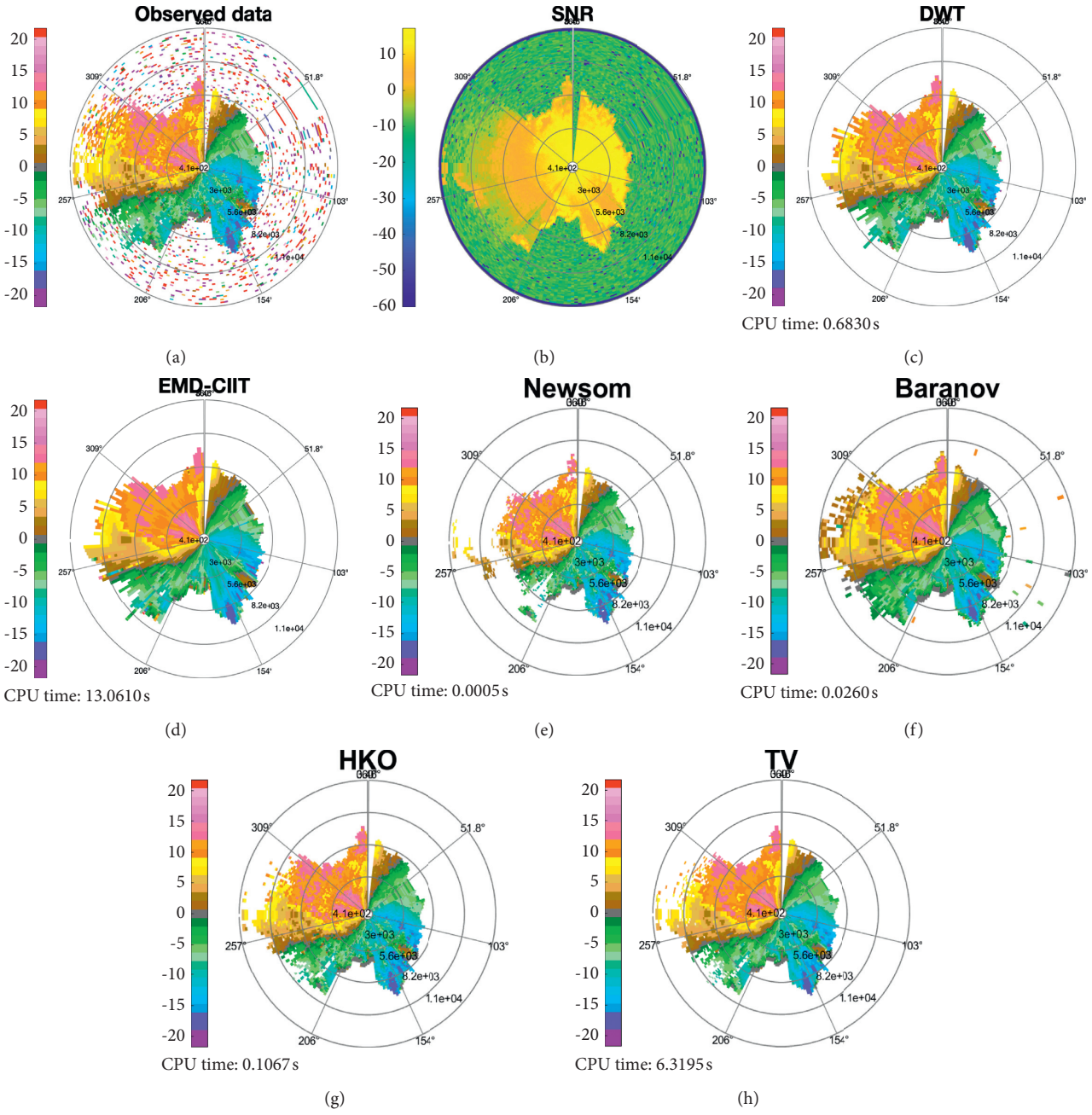

FIGURE 8: (a) The LiDAR data and (b) SNR values collected on 5 March 2015 from 04 : 16 : 02 to 04 : 16 : 25. The denoising results by (c) the "DWT" method, (d) the "EMD-CIIT" method, (e) the "Newsom" method, (f) the "Baranov" method, (g) the HKO method, and (h) the proposed scheme (denoted by TV).

3509 m are usually high, which means LiDAR observations are quite accurate.

(3) There are usually more noisy observations in large slant range values. We see from Table 1 that there are only 281927 LiDAR observations in the slant ranges from 6659 m to 9809 m and 793282 LiDAR observations in the slant ranges from 3509 m to 6659 m compared with 1033268 LiDAR observations in the slant ranges from 359 m to 3509 m.

(4) The number $\sum_{i=1}^{m}\sum_{j=1}^{n} w_{i,j}$ of denoising values by the proposed method is less than the number of original observations $y_{i,j}$ and the number of denoising values $x_{i,j}^{(Baranov)}$ by the "Baranov" method and the number of denoising values $x_{i,j}^{(HKO)}$ by the HKO method when there are many noisy observations in the slant ranges from 6659 m to 9809 m. However, the proposed method preserves more data points with high SNR values in the slant ranges from 6659 m to 9809 m.

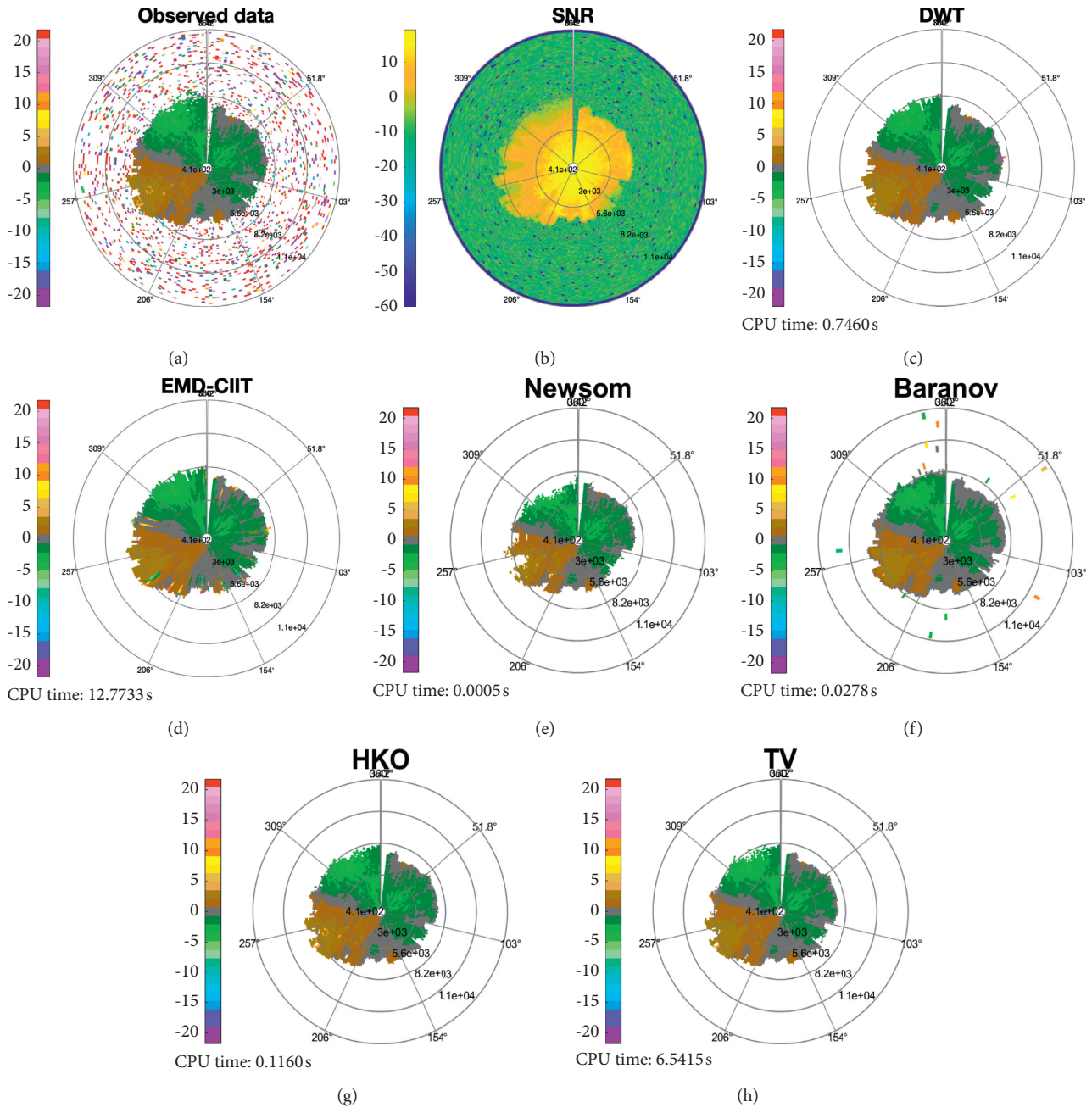

Figure 9: (a) The LiDAR data and (b) SNR values collected on 4 March 2015 from 00 : 00 : 16 to 00 : 00 : 39. The denoising results by (c) "DWT" method, (d) "EMD-CIIT" method, (e) "Newsom" method, (f) "Baranov" method, (g) HKO method, and (h) the proposed scheme (denoted by TV).

Table 1: The comparison of noisy observations removal by the "Newsom" method, "Baranov" method, HKO method, and proposed method.

Range	Data	SNR > = −5	SNR > = −3	SNR > = 0
359 m–3509 m (total number: 1036067)	LiDAR observations	1033268	1032885	1031484
	Denoising values by the "Newsom" method	1031472	1031472	1031472
	Denoising values by the "Baranov" method	1033268	1032885	1031484
	Denoising values by the HKO method	1033212	1032874	1031484
	Denosing values by the proposed method	1032987	1032793	1031394

Table 1: Continued.

Range	Data	SNR > = −5	SNR > = −3	SNR > = 0
3509 m–6659 m (total number: 836510)	LiDAR observations	793282	772883	678138
	Denoising values by the "Newsom" method	677112	677112	677112
	Denoising values by the "Baranov" method	793282	772883	678138
	Denoising values by the HKO method	791440	772670	678130
	Denosing values by the proposed method	786772	772632	678043
6659 m–9809 m (total number: 455697)	LiDAR observations	281927	184425	77073
	Denoising values by the "Newsom" method	76645	76645	76645
	Denoising values by the "Baranov" method	281927	184425	77073
	Denoising values by the HKO method	263033	183026	77018
	Denoising values by the proposed method	247713	184353	77070

4. Conclusion

In this article, we have proposed a LiDAR data denoising scheme for wind profile observations to improve data quality and remove bad observations. By introducing a weight in each observation, the scheme can filter out very noisy observations according to their SNR values and neighborhood observations. Combining with the data-fitting term and the polar-based total variation smoothing term, a global-based denoising model is built. The alternating direction method of multipliers is applied to find a solution of the proposed model. To find suitable regularization parameters of the proposed scheme, we consider an L-curve based parameter selection method that can select parameters automatically via the balance between the data-fitting term and the polar-based total variation regularization term. By applying the proposed scheme to the LiDAR data collected at the Hong Kong International Airport, we find that (i) our proposed scheme performs better than the denoising methods such as DWT and EMD-CIIT, where they cannot handle very noisy observations and they can conduct a denoising procedure along each slant range; (ii) our proposed method can handle noisy observations quite well, and its performance is better than that of HKO method and "Newsom" method as well as "Baranov" method; (iii) our proposed scheme can balance the data-fitting and the smoothing regularization via suitable parameter selection. However, the proposed scheme is slower than the comparing methods except the EMD-CIIT method. As a future research work, we will investigate a much faster algorithm for the proposed model. And we also need to consider an online denoising scheme such that it can handle LiDAR data sets in a continuous-time manner and study three-dimensional LiDAR data observations for denoising.

Data Availability

The request for data used to support the findings of this study could be addressed to the Hong Kong Observatory. The data provision would be considered on a case-by-case basis.

Conflicts of Interest

The authors declare that there are no conflicts of interest regarding the publication of this paper.

Acknowledgments

The research was supported in part by HKRGC GRF 17201020 and 17300021 and UGC-RMGS 207300829.

References

[1] M. Li, J. Xu, X. Xiong, Y. Ma, and Y. Zhao, "A novel ramp method based on improved smoothing algorithm and second recognition for windshear detection using lidar," *Current Optics and Photonics*, vol. 2, no. 1, pp. 7–14, 2018.

[2] A. Weipert, S. Kauczok, R. Hannesen, T. Ernsdorf, and B. Stiller, "Wind shear detection using radar and lidar at frankfurt and munich airports," in *Proceedings of the 8th European Conference on Radar in Meteorology and Hydrology*, Garmisch-Partenkirchen, Germany, December 2014.

[3] M. Sarvani, K. Raghunath, and S. V. B. Rao, "Lidar signal denoising methods- application to NARL Rayleigh lidar," *Journal of Optics*, vol. 44, no. 2, pp. 164–171, 2015.

[4] Z. Xu, Y. Wang, and G. Fan, "A two-stage quality control method for 2-m temperature observations using biweight means and a progressive eof analysis," *Monthly Weather Review*, vol. 141, no. 2, pp. 798–808, 2013.

[5] S. Yin and W. Wang, "Lidar signal denoising based on wavelet domain spatial filtering," in *Proceedings of the 2006 CIE International Conference on Radar*, Shanghai, China, October 2006.

[6] H. Hassanpour, "Improved svd-based technique for enhancing the time-frequency representation of signals," in *Proceedings of the 2007 IEEE International Symposium on Circuits and Systems*, pp. 1819–1822, IEEE, Piscataway, NJ, USA, May 2007.

[7] H. Hassanpour, "A time-frequency approach for noise reduction," *Digital Signal Processing*, vol. 18, no. 5, pp. 728–738, 2008.

[8] M. Azadbakht, C. S. Fraser, C. Zhang, and J. Leach, "A signal denoising method for full-waveform lidar data," *Proceedings of the ISPRS Annals of Photogrammetry, Remote Sensing and Spatial Information Sciences, Antalya, Turkey*, vol. 11–13, 2013.

[9] S. Wu, Z. Liu, and D. Sun, "Noise reduction in los wind velocity of Doppler lidar using discrete wavelet analysis," *Chinese Optics Letters*, vol. 1, no. 12, pp. 722–725, 2003.

[10] S. Wu, Z. Liu, and B. Liu, "Enhancement of lidar backscatters signal-to-noise ratio using empirical mode decomposition method," *Optics Communications*, vol. 267, no. 1, pp. 137–144, 2006.

[11] N. E. Huang, Z. Shen, S. R. Long et al., "The empirical mode decomposition and the hilbert spectrum for nonlinear and

non-stationary time series analysis," *Proceedings of the Royal Society of London. Series A: Mathematical, Physical and Engineering Sciences*, vol. 454, no. 1971, pp. 903–995, 1998.

[12] Z. Liu, N. Zhang, R. Wang, and J. N. Zhu, "Doppler wind lidar data acquisition system and data analysis by empirical mode decomposition method," *Optical Engineering*, vol. 46, no. 2, p. 026001, 2007.

[13] Y. Zhang, X. Ma, D. Hua, Y. Cui, and L. Sui, "An emd-based denoising method for lidar signal," in *Proceedings of the 2010 3rd International Congress on Image and Signal Processing*, pp. 4016–4019, IEEE, Yantai, China, October 2010.

[14] J. Li, W. Gong, and Y. Ma, "Atmospheric lidar noise reduction based on ensemble empirical mode decomposition," *The International Archives of the Photogrammetry, Remote Sensing and Spatial Information Sciences*, vol. XXXIX-B8, pp. 127–129, 2012.

[15] P. Tian, X. Cao, J. Liang et al., "Improved empirical mode decomposition based denoising method for lidar signals," *Optics Communications*, vol. 325, pp. 54–59, 2014.

[16] P. Tian, L. Zhang, X. Cao, and N. Yi, "The application of emd-ciit lidar signal denoising method in aerosol detection," *Procedia Engineering*, vol. 102, pp. 1233–1237, 2015.

[17] Y. Kopsinis and S. McLaughlin, "Development of emd-based denoising methods inspired by wavelet thresholding," *IEEE Transactions on Signal Processing*, vol. 57, no. 4, pp. 1351–1362, 2009.

[18] N. Baranov and E. Lemishchenko, "Windshear identification algorithms by Doppler pulse lidar," *ITM Web of Conferences*, vol. 24, p. 1011, 2019.

[19] R. K. Newsom, L. K. Berg, W. J. Shaw, and M. L. Fischer, "Turbine-scale wind field measurements using dual-Doppler lidar," *Wind Energy*, vol. 18, no. 2, pp. 219–235, 2015.

[20] P. W. Chan and C. M. Shun: Application of a Ground-Based Doppler LIDAR to Automatic Windshear Alerting.

[21] C. M. Shun and P. W. Chan, "Applications of an infrared Doppler lidar in detection of wind shear," *Journal of Atmospheric and Oceanic Technology*, vol. 25, no. 5, pp. 637–655, 2008.

[22] P. W. Chan, C. M. Shun, and K. C. Wu, "Operational lidar-based system for automatic windshear alerting at the Hong Kong international airport," in *Proceedings of the 12th Conference on Aviation, Range, and Aerospace Meteorology*, vol. 6, Atlanta GA, USA, January 2006.

[23] R. W. Liu, L. Shi, W. Huang, J. Xu, S. C. H. Yu, and D. Wang, "Generalized total variation-based mri rician denoising model with spatially adaptive regularization parameters," *Magnetic Resonance Imaging*, vol. 32, no. 6, pp. 702–720, 2014.

[24] W. Lu, J. Duan, Z. Qiu, Z. Pan, L. Bai, and R. W. Bai, "Implementation of high-order variational models made easy for image processing," *Mathematical Methods in the Applied Sciences*, vol. 39, no. 14, pp. 4208–4233, 2016.

[25] L. I. Rudin, S. Osher, and E. Fatemi, "Nonlinear total variation based noise removal algorithms," *Physica D: Nonlinear Phenomena*, vol. 60, no. 1-4, pp. 259–268, 1992.

[26] S. Boyd, N. Parikh, E. Chu, B. Peleato, and J. Eckstein, "Distributed optimization and statistical learning via the alternating direction method of multipliers," *Foundations and Trends in Machine Learning*, vol. 3, no. 1, pp. 1–122, 2011.

[27] R. Barrett, M. Berry, T. F. Chan et al., *Templates for the Solution of Linear Systems: Building Blocks for Iterative Methods*, SIAM, Philadelphia, PA, USA, 1994.

[28] P. S. Cgs, "A fast lanczos-type solver for nonsymmetric linear systems," *SIAM Journal on Scientific and Statistical Computing*, vol. 10, no. 1, pp. 36–52, 1989.

[29] D. L. Donoho and I. M. Johnstone, "Ideal spatial adaptation by wavelet shrinkage," *Biometrika*, vol. 81, no. 3, pp. 425–455, 1994.

[30] P. C. Hansen: The L-Curve and its Use in the Numerical Treatment of Inverse Problems. 1999.

[31] P. C. Hansen, "Regularization tools version 4.0 for matlab 7.3," *Numerical Algorithms*, vol. 46, pp. 189–194, 2007.

[32] J. Huang, M. K. P. Ng, and P. W. Chan, "Wind shear prediction from light detection and ranging data using machine learning methods," *Atmosphere*, vol. 12, no. 5, 2021.